UNIVERSITY OF SOUTHAMPTON

Faculty of Engineering and the Environment

School of Engineering Sciences

Modelling the degradation of particles in fluidised beds

by

Jörn Bruchmüller

Supervision: Dr Sai Gu and Prof. Kai H. Luo

Thesis for the degree of Doctor of Philosophy

October 2012

UNIVERSITY OF SOUTHAMPTON

ABSTRACT

FACULTY OF ENGINEERING AND THE ENVIRONMENT
SCHOOL OF ENGINEERING SCIENCES

Doctor of Philosophy

by Jörn Bruchmüller

This thesis focuses on modelling the degradation of particles in gas-solid fluidised beds. Modelling is performed by using a coupled approach where the gas phase is treated as a continuum and the solid phase is represented by individual discrete particles, using the discrete element method (DEM). This approach makes it possible to access individual particle properties. By implementing new modelling techniques into the DEM framework, the individual particle degradation behaviour can be numerically described with high accuracy. The main interest is to understand more complex gas-solid systems as encountered e.g. in fluidised beds which might contain numerous degrading particles. This work focuses on verifying and validating these sub-models to be able to obtain accurate information for further suggestions in operation and optimisation of dense particulate systems.

Particle degradation is studied by means of thermophysical, thermochemical and mechanical aspects. Drying (thermophysical) is an energy intensive process which makes further research inevitable for further optimisation. Large particles during drying develop temperature and species gradients along their radius, affecting the product quality. The DEM has been used to monitor flow, particle and sub-particle properties which have been found useful to control, operate and optimise such large particle drying processes. Pyrolytic (thermochemical) conversion of biomass in fluidised beds represents a promising route for the production of bio-oil. This process has been modelled and studied under consideration of drying, shrinkage, segregation and entrainment. Breakage or mechanical degradation is often encountered in engineering applications and requires a much better process understanding. Therefore, a new discrete fragmentation method (DFM) has been developed to study breakage in dense particle systems such as fluidised beds but also mills or crushers. Much reliable breakage information can be obtained to further optimise such systems.

Contents

Acknowledgements

This thesis would not have been possible without the essential and gracious support of many individuals. First and foremost, I offer my sincerest gratitude to both of my supervisors, Dr Sai Gu and Professor Kai H. Luo, who have supported me thoughout my thesis with their patience and trust to try projects which where maybe too adventures or challenging at a first glance. Both gave me the room to work largely in my own way but also provided advice and help in many aspects. I am aware, that I have been, only one out of many students who got such a financial support being able to establish novel collaborations and attending many conferences overseas - all this enhanced my work substantially. I am very grateful for all your support!

I had most in-depth discussions about my work with Dr Berend van Wachem and would like to thank him for giving me so much insight and help with MultiFlow, general mechanical engineering problems, writing rebuttal letters and many more. My one month stay at Imperial College London and our several mutual visits have converted the purely collaborative relation into what I would say a friend to me.

I cannot express enough gratitude to Professor Robert C. Brown, his family and research group who made my 6 weeks stay at Iowa State University so pleasant and special. I got the opportunity to start this collaboration with attending the Biochar Initiative Conference 2010, I had dinner with the Brown family in their own garden and Robert was planning to turn me into a real experimentalist. Members of his research group have made me feel home (Catie, Kaige, Patrick,...) and helped me hands-on with my own experiments (Dustin, Pat, Najeeb,...). I hope I can return at least some of their effort one day.

In my daily work I have been blessed with a friendly and cheerful group of fellow students and colleagues. I will never forget our game evenings with Jun, Ningping and Andreas. My housemate and colleague Hani who I shared lots of conversations with and Stephan who pushed me to do cycle trips of at least 100km every time. I

learned a great deal even in our small fast pyrolysis group in office 1051 - Kostas, Lindsay, Nanhang and Dekui - I always loved to discuss this stuff! I really enjoyed the everyday lunch breaks and trips outside Southampton with Matteo, Stephan, Andreas, Max, Phil and many more. I also thank Daina, my dance partner, for the variety to every days life. Thanks to Mario, Ben, Wendell, Akeel, Lorenzo,... who played football with us. And of course the list doesn't stop here, Costas, Nanda, Arvind,... and still, I have just mentioned a tiny part of all who made my life so rich.

Most of all, I thank my mother for supporting me throughout my life and for providing a home I always felt welcome to return.

Financial support from EPSRC (Grant No. EP/G034281/1) is highly acknowledged. Supercomputing resources on HECToR are highly appreciated from the EPSRC grant No. EP/I000801/1.

Declaration of Authorship

I, Jörn Bruchmüller, declare that the thesis entitled 'MODELLING THE DEGRADATION OF PARTICLES IN FLUIDISED BEDS' and the work presented in the thesis are both my own, and have been generated by me as the result of my own original research. I confirm that:

- this work was done wholly or mainly while in candidature for a research degree at this University.
- where any part of this thesis has previously been submitted for a degree or any other qualification at this University or any other institution, this has been clearly stated.
- where I have consulted the published work of others, this is always clearly attributed.
- where I have quoted from the work of others, the source is always given. With the exception of such quotations, this thesis is entirely my own work.
- I have acknowledged all main sources of help.
- where the thesis is based on work done by myself jointly with others, I have made clear exactly what was done by others and what I have contributed myself.
- parts of this work have been published as given in the list of publications.

Signed: .....

Date: .....

List of Publications

Journal Articles:

J. Bruchmüller, B.G.M. van Wachem, S. Gu, K.H. Luo and R.C. Brown, "Modelling the Thermochemical Degradation of Biomass inside a Fast Pyrolysis Fluidised Bed Reactor", Paper accepted by AIChE Journal

J. Bruchmüller, B.G.M. van Wachem, S. Gu and K.H. Luo, "Modelling Discrete Fragmentation of Brittle Particles", Powder Technology 208 (3), pp.731-739, 2011

J. Bruchmüller, S. Gu, K.H. Luo and B.G.M. van Wachem, "Discrete Element Method for Multiscale Modelling", Journal of Multiscale Modelling 2 (2), pp.147-162, 2010

Conference Papers:

J. Bruchmüller, B.G.M. van Wachem, S. Gu and K.H. Luo, "Modeling Discrete, Incremental Repetitive and/or Simultaneous Particle Breakage", 7th International Conference on Multiphase Flow (ICMF-2010), Tampa, USA, 30 May – 4 June (2010), Paper available online at: http://ufdc.ufl.edu/UF00102023/00228

J. Bruchmüller, B.G.M. van Wachem, S. Gu and K.H. Luo, "Heat and mass transfer of drying particles in a fluidized bed", 14th International Heat Transfer Conference, Washington DC, USA, 8-13 August 2010, ASME Conf. Proc., Volume 4, pp. 289-295, doi:10.1115/IHTC14-22292

J. Bruchmüller, B.G.M. van Wachem, S. Gu and K.H. Luo, "Gas-Solid Fluidised Bed Modelling with Interphase Exchange Phenomena", Proceedings of the bioten conference on biomass, bioenergy and biofuels 2010, Birmingham, UK, 21-23 September (2010), CPL Press, ISBN: 978-1-872691-54-1

List of Figures

List of Tables

Nomenclature

Roman Symbols

A	Particle surface area (m^2)
A	Pre-exponential factor $(1/s)$
b	Standard slope parameter in drop weight tests (kg/J)
Bi	Biot number $(-)$
c	Heat capacity of a solid material (kJ/KgK)
c	Vapour concentration (kg/m^3)
C_D	Drag coefficient $(-)$
c_p	Heat capacity under constant pressure (kJ/kgK)
CF	Collision factor $(-)$
D	Diffusion coefficient (m^2/s)
d_p	Particle diameter (m)
d_{min}	Smallest fragment diameter created (m)
E	Activation energy (J/mol)
E	Young's modulus (N/m^2)
e	Coefficient of restitution $(-)$
e_F	Coefficient of restitution for fragmentation $(-)$
F	Force (N)
f_{Mat}	Material resistance factor (kg/Jm)

Fo	Fourier number $(-)$
G	Shear modulus (N/m^2)
g	Gravitational acceleration (m/s^2)
ΔH	Reaction heat or latent heat (kJ/kg)
h	Convective heat transfer coefficient (W/m^2K)
k	Convective mass transfer coefficient (m/s)
k	Reaction rate $(1/s)$
k	Spring constant $(N/m^{3/2})$
K_{IC}	Fracture toughness of the first mode $(N/m^{3/2})$
l_0	Characteristic length (m)
M	Maximum achievable t_{10} $(-)$
m	Mass (kg)
M_x	Mass of all particles in bin x (kg)
$\vec{n}$	Normal vector $(-)$
Nu	Nusselt number $(-)$
P	Pressure (Pa)
P	Probability of breakage $(-)$
Pr	Prandtl number $(-)$
$\dot{Q}$	Energy source term (W)
r	Particle radius (m)
R_u	Universal gas constant (8.314 $kJ/kmolK$)
R_{cond}	Resistance to conductive heat transfer (K/W)
R_{conv}	Resistance to convective heat transfer (K/W)
Re_p	Particle Reynolds number $(-)$
S	Species source term (kg/m^2K)

Sc	Schmidt number $(-)$
T	Temperature (K)
T	Torque (Nm)
t	Time (s)
t_{10}	Breakage index $(-)$
u	Velocity (m/s)
u_0	Superficial gas velocity (m/s)
V	Volume (m^3)
W	Molar mass (kg/mol)
$W_{m,kin}$	Mass specific impact energy (J/kg)
$W_{m,min}$	Minimum mass specific energy causing particle damage (J/kg)
X	Mass fraction (kg/kg_{DS})
Y	Mass fraction (kg/kg_{total})
Y_m	Mole fraction (mol/mol_{total})

Abbreviations

∇	$\nabla = \sum_{i=1}^{3} \frac{\partial}{\partial x_i}$
CFD	Computational fluid dynamics
DEM	Discrete element method
FSP	Fibre saturation point
PSD	Particle size distribution
SAG	Semi-autogenous (mill)

Greek Symbols

α	Thermal diffusivity (m^2/s)
β	Interphase momentum transfer coefficient (kg/m^3s)
Γ	Diffusion coefficient (m^2/s)

δ	Overlapping distance between two particles or the wall (m)
ϵ	Gas volume fraction (m^3/m^3_{cell})
η	Damping coefficient $(kg/sm^{1/2})$
θ	Dimensionless temperature $(-)$
λ	Thermal conductivity (W/mK)
μ	Dynamic viscosity (kg/ms)
μ	Friction coefficient $(-)$
μ_n	Eigenvalues $(-)$
ν	Poisson ratio $(-)$
ξ	Dimensionless particle radius $(\xi = r/r_0)$ $(-)$
ρ	Density (kg/m^3)
ρ^*	Phase averaged density (kg/m^3)
τ	Shear stress tensor (N/m^2)
Φ	Any scalar value (units denpend)
$\dot{\omega}$	Energy source term (J/m^3s)
ω	Particle emissivity $(-)$

Subscripts

ab	After breakage
ar	After replacement
b	At the moment of breakage
b	Bound water
bi	Before impact
coll	Collision
cond	Conduction
conv	Convection

cp	Child particle
$diss$	Dissipated
dn	Damping normal
DS	Dry solid material
dt	Damping tangential
el	Elastic (spring) component
en	Elastic normal
et	Elastic tangential
$evap$	Evaporation
f	Fluid
g	Gas
g	Gravity
$init$	Initial value
kin	Kinetic component
l	Free liquid water
mf	Minimum fluidisation
n	In normal direction
nb	Neighbouring
p	Particle
pp	Parent particle
ref	Reference (or constant) value
rem	Remembered value
rn	Relative normal
s	Surface
sat	Saturation

t	Tangential
w	Wall

Chapter 1

Introduction

Fluidised beds are used commercially in the chemical, pharmaceutical, agricultural, petroleum, biochemical, food and power generation industries. There is enormous potential to further improve applied systems in fluidisation beyond restricting the focus on the hydrodynamic fluidisation behaviour of granular material. The degradation behaviour of particles in fluidised beds is particularly important to further improve and understand such systems. This chapter introduces the reader to gas-solid fluidisation in general, covers the main objectives of this thesis and highlights the main motivation to tackle this complex research field by means of numerical simulations. Finally, an outline of this thesis is provided.

1.1 Gas-Solid Fluidisation

When a fluid is passed through a bed of particles the pressure difference between the bottom and top of the bed rises due to frictional resistance with increasing fluid velocity (see Figure 1.1(A)). When the drag force exerted by the fluid on a cluster of particles has reached the gravitational force of the cluster, particles begin to move and the bed expands. This state is called incipient or minimum fluidisation (B). In most fluidised bed applications, a higher fluid velocity is used. Gas-solid fluidisation is achieved by which solid particles are transformed into a liquidlike state through suspension in the gas [1]. In bubbling fluidised beds, the pressure loss remains constant (C) until particle entrainment is initiated and pneumatic transport starts (D).

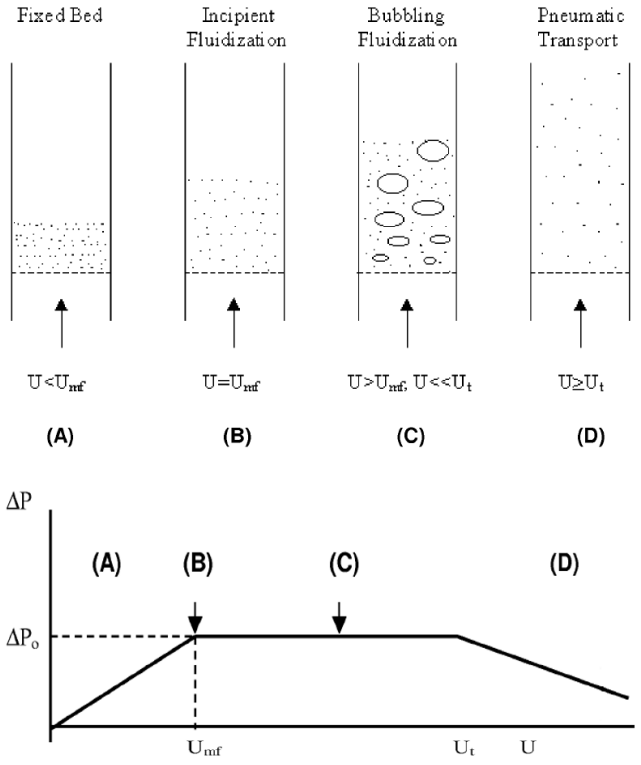

FIGURE 1.1: Different regions of gas-solid fluidisation [2]

The fluidisation behaviour is also dependent on the particle size as classified by Geldart [3]. For air fluidisation below $u_0 = 10U_{mf}$, four different distinct fluidisation behaviour can be expected (see Figure 1.2). Geldart C particles are very fine (e.g. flour) and inter-particle cohesive forces are usually higher than the drag forces created by the fluidising gas. This makes them difficult to fluidise. Geldart A particles (e.g. catalysts) are aeratable meaning that the bed expands considerably before bubbles appear. These solids are easy to fluidise. Geldart B particles are sandlike, they fluidise well with vigorous bubble formation and bubbles grow large. Geldart D particles (e.g. grains) are spoutable and when applied to fluidisation only shallow beds are used as deep beds are difficult to fluidise, they behave erratically.

When bubbles become large enough to spread across a wide portion of the vessel's domain, the bed behaviour is called slugging instead of bubbling. Slugging occurs preferably in deep and small diameter beds, particularly when larger particles are fluidised. This work focusses on bubbling and slugging fluidised beds with Geldart B or D particles.

Fluidised beds are widely used in industrial applications because of several reasons. When the bed is filled with many particles, the total surface area of all particles

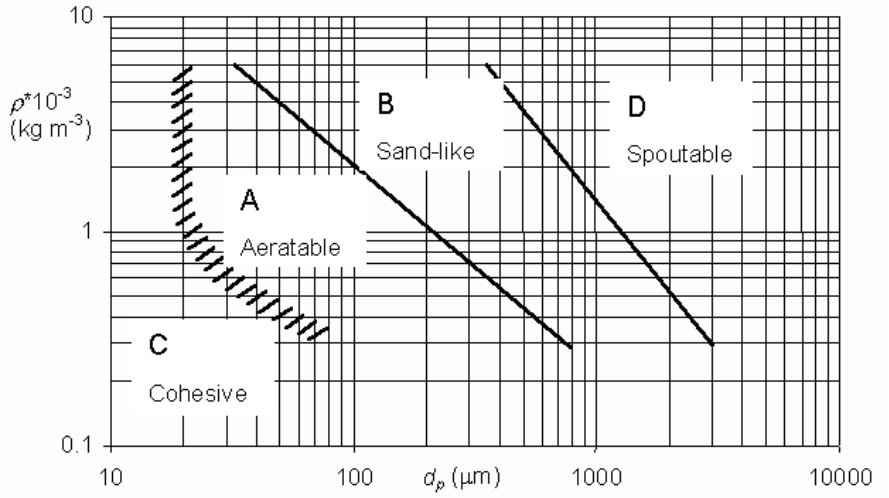

FIGURE 1.2: Geldart's classification of powders [3]

together is huge. Sand, as a common bed material, is known to have a high heat capacity so that an initial bed temperature won't change rapidly even when reactions are strongly endo-/exothermic. The bed is usually well mixed and has quasi isothermal properties making the reactor very suitable to control chemical reactions. When non-inert (cold) particles entering the bed, typically high heat and mass transfer is achieved. Due to the liquidlike flow behaviour of the solid, easy handling of the bed material can be achieved.

The disadvantage to operate fluidised beds is the high power consumption to fluidise the bed. Fluidised beds have also a high gas by-pass (bubbles) and reactants can pass unreacted while gas back-mixing might lead to undesirable secondary reactions. High exit gas temperature reduces the efficiency of these plants as the heat is difficult to regain. Due to the intense solid contacting, particle attrition and erosion of reactor walls are often reported. Size reduction or agglomeration (sintering) can change the fluidisation behaviour. The hydrodynamic behaviour is highly non-linear and therefore difficult to scale-up.

Fluidisation engineering applications require much more than the pure knowledge on gas-solid contacting. Physical applications can be often found in drying, mixing, granulation, coating, heating and cooling while chemical applications are more related to combustion, gasification, pyrolysis, catalytic reactions and many more. These processes have been introduced in the late 20th century with enormous potential to be heavily applied in future. Some of those fluidised bed applications are further discussed in this thesis to enhance the knowledge of particle degradation processes in widely encountered engineering systems.

1.2 Modelling fluidised bed applications

Computational fluid dynamics (CFD) has become a powerful tool to predict the flow behaviour of many systems, being important for scale-up, design or optimisation studies. Modelling provides usually much more local, specific and detailed information which are too troublesome or difficult to obtain in experiments. Unsteady CFD simulations deliver time-dependent solutions while experiments are often restricted to averaged steady-state results. CFD models are capable of giving a good prediction of the actual flow pattern in fluidised beds, are a valuable tool to validate and improve existing (empirical) correlations, to determine new correlations, and to calculate specific physical properties of a certain configuration [4].

Different numerical simulation strategies to model gas-solid fluidised beds have been reviewed by van der Hoef et al. [5]. In most cases, multiphase modelling of the hydrodynamic behaviour in fluidised beds, and any application of it, is either achieved by an Euler-Euler or Euler-Lagrange approach. In Euler-Euler simulations, both the gas and solid phase are modelled as separate interpenetrating continua. The solid phase can also be modelled by the discrete element method (DEM), a sub-set of the Lagrangian approach, where each individual particle is updated and each particle location is known.

The Euler-Euler approach is able to model gas-solid multiphase flows. Herein, the solid phase is described by using the kinetic theory of granular flows. This methodology assumes that the dense solid phase behaves like a fluid (therefore it has also the name "two-fluid model") and updates the emulsion phase on the fluid-cell level. It does consider solid particle properties which in turn have to be volume averaged. The advantage of two-fluid models is the relatively low computational demand. Its applicability to purely hydrodynamic studies without particle modifications (degradation or agglomeration) in dense solid flows is well accepted and it is successfully and widely applied today.

Inconsistencies and erroneous predictions occur when two-fluid models are applied to dilute gas-particle flows [6]. Desjardin et al. [7] pointed out that two-fluid models are unable to correctly capture particle trajectory crossing and particle segregation is artificially over predicted for finite Knudsen numbers. Furthermore, no information can be obtained from two-fluid models about the residence time of individual reacting particles, representing highly valuable key-information in fluidised bed applications. Although computationally expensive, the Eulerian-Lagrangian approach (or the CFD-DEM approach) has better potential to realistically reveal

thermochemical processes in granular multi-phase flow applications. The Euler-Lagrange approach potentially offers the most accurate description not only of the particle motion (translational and rotational, particle-particle collisions) but also of chemical reactions and heat and mass transfer between the dispersed phase and the gas phase at the individual particle scale [8]. Therefore, trajectories, temperature, composition (reaction rates) and many other additional particle information are more reliably and more naturally included than in Eulerian formulations which are based on spatial averaging techniques with strong simplifications made on the particle kinematics and thermodynamics.

When it comes to model Geldart D particles, the hydrodynamic behaviour shows marked deviations from those obtained from two-fluid models [9]. Geldart [10] reported that applications of the two-fluid theory for group D particles, the group that is mainly used in the drying process, results in up to 50 % error in the bubble flow rate.

Due to its high computational demand, DEM simulations are mostly performed in 2D or quasi 3D (domain width is one or slightly more particle diameters). Erroneous predictions in 2D/quasi 3D simulations have been found based on porosity [11], the particle contact number, segregation, drag and interparticle percolation [12] so that other simulation strategies such as parallel computing techniques, periodic-boundaries or novel numerical time integration schemes [13] are favoured to maintain the computational feasibility.

Research on the hydrodynamic behaviour of the sand phase in fluidised beds has been extensively studied in the literature while most aspects related to the degradation of particles in dense beds are not sufficiently understood and investigated (exploited) by CFD-DEM simulations (see Chapter 2). Fluidised beds contain often particles which undergo chemical reactions, fragmentation, agglomeration or a change in material or physical properties in general. These small-scale effects at the particle level are key-aspects for the overall performance of chemical, pharmaceutical, agricultural, building, mining, food, gas or oil processing systems.

The motivation of this work is to look at the performance of small applied engineering systems which have not sufficiently been studied with DEM before and which are or might become in the near future highly important for industrial applications. Three examples are studied in this thesis which include thermophysical, thermochemical and mechanical particle degradation processes in dense beds by means of drying, fast pyrolysis and fragmentation. All these processes

are explained in the following subsections including their individual motivation for further investigation.

1.2.1 Drying of Large Particles

Drying is the process of moisture removal due to simultaneous heat and mass transfer [14]. It is one of the conservation methods of agricultural products, which is most often used and the most energy-intensive process in industry [15]. It is reported that industrial dryers consume on average about 12% and maximum 60-70% of the total energy used in manufacturing processes [2]. Drying does not only improve the shelf-life of agricultural products (food), it also improves the thermal efficiency of the thermochemical conversion process of solid fuels. This indicates the importance of improving and optimising drying technology in general to obtain better product quality and to reduce the overall energy consumption and its associated greenhouse gas emissions.

According to Rhodes [16], one of the most important application of fluidised beds is drying of solids. This is because fluidised bed drying has many advantages over other convective drying technologies. This technique offers ease in operation and maintenance, adaptability for combining several processes such as mixing, classification and cooling, it requires less drying time due to high heat and mass transfer and provides a uniform and closely controllable bed temperature [17]. However, due to the high amount of heated fluidisation gas required, fluidised bed drying is a very energy intensive process.

In fluidised beds, particles can be dried in batch or continuous mode. Batch mode begins with an initial charge of wet particles, which are dried by the fluidising gas medium (e.g. air), followed by a subsequent complete discharge of all particles. In continuous drying, both the wet and dry particles are continuously supplied and removed respectively. Batch operation is preferred for small-scale production and heat-sensitive materials, delivering a high uniform product quality [17].

Larger grains (Geldart D particles) are, in particular, better suited for drying in fluidised beds [9]. Modelling larger particles with the DEM is favoured to keep the particle time step in feasible limits, meaning that this modelling approach is particularly suited to be applied to fluidised bed drying. Drying is also a widely applied process making it relatively easy to validate models with experimental data.

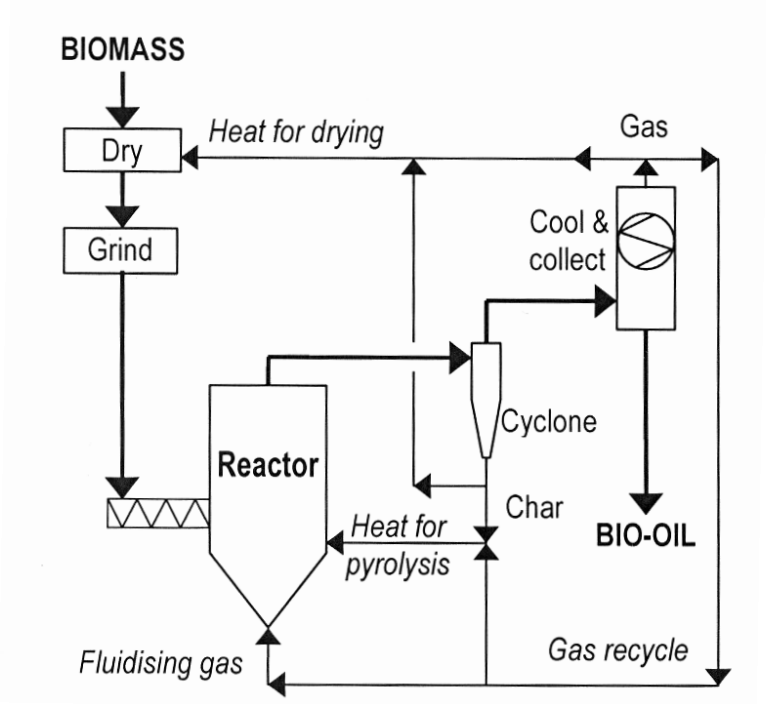

FIGURE 1.3: Conceptual fluid bed fast pyrolysis process [18]

1.2.2 Fast Pyrolysis of Biomass Particles

Fast pyrolysis is a high-temperature process in which organic material (often biomass) is rapidly heated to 400-550^{o}C in the absence of oxygen [18]. Fast pyrolysis is the most widely used process to convert biomass into high fractions of liquid bio-oil [19]. Bubbling fluidised beds are often favoured over other reactor technologies for liquid bio-oil production due to high achievable oil-yields, good heat and mass transfer properties and ease in operation. The final liquid bio-oil yield depends on the amount of condensible gases created by primary pyrolysis reactions and their amount reduced by thermal cracking, repolymerisation and recondensation, which are referred to as secondary pyrolysis reactions. Both gases which condense at ambient temperature such as many hydrocarbon compounds summarised as tar and non-condensible gases (CO_2, CO, H_2, CH_4, etc.) which do not condense at ambient conditions are entrained while only sufficiently depleted particles follow the exit gas.

Figure 1.3 depicts a conceptual fluid bed fast pyrolysis process. The biomass moisture content should be less than 10 % based on dry wood to reduce the water content of the bio-oil. Fast pyrolysis feed is usually ground to small sizes (sawdust or small wood chips) depending on the type of reactor used. The biomass particle diameter should be less than 2mm for bubbling fluidised bed pyrolysers, less than 6mm in circulating fluidised beds and around 20mm in ablative pyrolysis

reactors [18]. Once biomass particles are injected into the reactor, they experience high heating rates of up to 1000^{o}C/s [20] and decompose quickly within a few seconds into gas, char and tar. All these products are entrained with the fluidising gas (e.g. N_2). They enter a cyclone first where char particles usually bigger than 10 μm are separated from the remaining product gas. The remaining gas mixture enters a condenser/heat exchanger where all condensible gases (vapour/tar) are liquefied to bio-oil. The residence time of vapours is usually less than 2 seconds overall to avoid secondary pyrolysis reactions and to obtain high bio-oil yields of up to 75%. Char and/or non-condensible gases can be burned with O_2 to provide process heat for the fluid bed pyrolyser or the drying process. Non-condensible gas can also be re-used as fluidising gas.

Fast pyrolysis of biomass is one of the most recent renewable energy processes to have been introduced. It offers the advantages of a liquid product, bio-oil that can be readily stored and transported. Bio-oil is a renewable liquid fuel and can also be used for production of chemicals. Fast pyrolysis has now achieved a commercial success for production of chemicals and is being actively developed for producing liquid fuels. Bio-oils have been successfully tested in engines, turbines, and boilers, and have been upgraded to high-quality hydrocarbon fuels, although at a presently unacceptable energetic and financial cost. [21]

The conversion from bio-oil to ethanol is highly desired. Farrell et al. [22] estimated that the savings in energy terms can be as high as 93% when conventional gasoline is substituted with cellulose-derived ethanol.

Fast pyrolysis requires better understanding to be further developed into a much more efficient process. Experiments have the drawback that tar causes trouble for most measuring devices and would darken windows for visual observation. CFD-DEM studies are very suitable to look into the conversion of biomass into gas, char and tar representing one of the most important steps in the overall process to generate bio-oils. During fast pyrolysis, the injected virgin biomass is quickly depleted within seconds making it possible for simulations to look at the overall particle life-time behaviour. Unlike combustion or gasification, fast pyrolysis does not include significant reactions between the gas and solid phase (heterogeneous reactions) or within the gas-phase (homogeneous reactions). A complete disregard of such reactions does not necessarily lead to erroneous simulation predictions. Furthermore, the thermochemical particle degradation is also depended on the particle moisture content (drying) and size reduction (fragmentation). Both can

be studied together with fast pyrolysis when fragmentation of thermochemical degrading particles is simplified to a shrinking process.

1.2.3 Fragmentation of Brittle Particles

In this work, fragmentation is defined as the process of irreversibly breaking a particle into two or more parts. The size reduction into a few large fragments of similar size compared to the parent particle is called breakage. Generation of very fine fragments which detach from the particle surface e.g. which resembles progressive flaking of ash from an original fuel particle is called attrition. From the DEM modelling point of view, breakage is best represented by the discrete fragmentation method (DFM) while attrition is best taken into account by shrinkage assuming fragments which detach from the surface are so small that their discrete presence can be neglected (not modelled). As this thesis goes further into the details of modelling particle breakage, the word fragmentation will correspond to breakage rather than to any other fragmentation mechanism.

The reason for particle breakage arises most often from mechanical or thermal stresses. Particle breakage due to mechanical forces is often encountered in industrial applications like mills, crushers and many more. It has been estimated that comminution processes (grinding of hard material like coal, ore or rock) consume 3% of all electricity generated world wide [23, 24]. Comminution comprises up to 70% of all energy required in a typical mineral processing plant [25]. Considering these factors, a small gain in comminution efficiency can have a large impact on operating costs of a plant. To improve such processes, modelling of mechanical breakage can be of particular interest. Such simulation tools can be much better validated with experiments and analytical correlations from purely mechanical breakage compared to breakage processes caused by thermal stresses.

This thesis and the work thereafter aim to develop a numerical approach to look at the overall process to describe the thermal degradation of biomass - including thermal fragmentation. Breakage of fuel particles is important to be considered when simulating the thermochemical degradation process of large particles as it strongly affects heat transfer to virgin fuel material and therefore the yield of products obtained. Large particles are used in larger thermochemical conversion plants and their general thermochemical degradation behaviour is important for scale-up studies. Experiments have shown that breakage occurs during devolatilisation such that fuel particles might fall apart into a few fragments of similar

size [26]. Brown et al. [27] suggest that breakage rather than attrition is the dominant mechanism in a fluidised bed combustor for fuel particle sizes larger than 2mm in diameter.

The fuel particle bursts due to thermal shock and pressure build-up of released volatile gases inside the particle which is called primary fragmentation (see Figure 1.4 (1,2)). During subsequent char conversion, pores increase in size, weakening the structure inside the char causing again breakage known as secondary fragmentation (3,4). Percolation is a special type of secondary fragmentation when oxygen is present e.g. during gasification or combustion. During percolation oxidation progressively erodes the solid structure until a sudden collapse of the particle network occurs. Attrition is the main mechanism causing a size reduction for very small particles due to the abrasive action of the bed material in fluidised beds (5,6). The size reduction is linked to combustion/gasification reactions with unreacted carbon (4,5) particularly when the surface area becomes bigger (and the particle smaller). Fragmentation of fuel particles is complex but highly desired to be investigated by discrete methods to further understand fuel particle degradation.

1.3 Research Objectives

Euler-Euler simulations have difficulties to describe accurately the particle degradation in dense beds as the relevant equations are solved on the fluid-cell level. However, DEM has the potential to study much more information - mainly due to the available growth in computational resources on which it depends. To improve most engineering applications applied to fluidised beds, the accuracy and flexibility of DEM models are required on the particle level to study effects like drying, thermochemical degradation, shrinkage, breakage, segregation, mixing, entrainment and many more. In most fluidised bed applications, particle degradation is the most crucial phenomenon inside dense particle beds.

The objective of this thesis is to study the drying process of one single thermally thick spherical particle first. Its applicability and suitability for its use to model an experimentally applied fluidised bed drying process need to be scrutinised. The single particle drying model needs to be made available for many particles. Finally, the fluidised bed model and its drying characteristics require validation with experiments. Detailed discussions of the drying process are targeted, especially based on information which are difficult to obtain from Euler-Euler models or experimental studies.

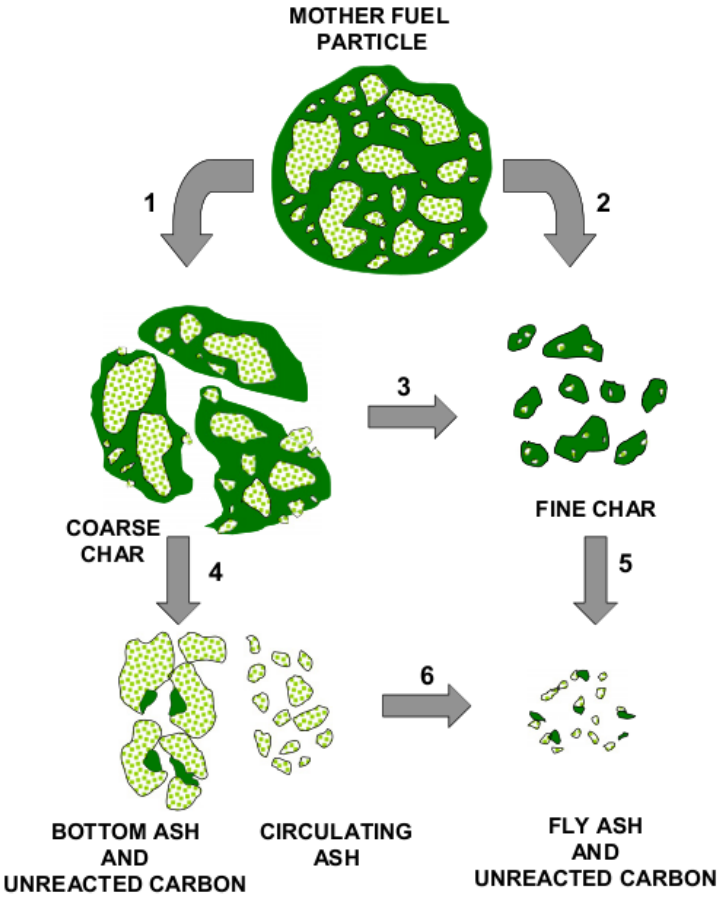

FIGURE 1.4: Main processes during fragmentation of fuel particles and char in fluidised beds. 1,2: Primary fragmentation, 3,4: secondary fragmentation, 5,6: attrition and 4,5: additional chemical consumption [28]

Fluidised beds are known for their good heat transfer characteristics and further investigations into thermochemical particle degradation is one of the most important aspects in the field of chemical engineering. Similarly to drying, the state-of-the-art fast pyrolysis process on single thermally thick particles needs to be investigated first, before stipulating the requirements needed to model efficiently large numbers of reacting particles inside dense beds. A fast pyrolysis process should be modelled which reproduces experimental results considering the main variables affecting pyrolysis. The characteristics of the particle or bed behaviour requires thoughtful discussions related to mixing, segregation, fluidisation and entrainment.

Modelling thermochemical degradation including particle break-up with DEM is a long-term objective rather than the objective of this thesis alone and has to be tackled in smaller steps. Validation of such model requires experimental results

with very detailed information which in turn is difficult to find. Hence, mechanical breakage as found during comminution processes, which is studied at ambient conditions, is far easier to model and validate than thermal breakage which occurs in hot fluidised beds. The objective of this work is to develop a discrete fragmentation model which can be applied to comminution processes and which can be developed further. The model should predict reasonable fragment size distributions, create a number of fragments suitable[1] for DEM simulations and determine accurate energy and momentum of fragments after breakage. The model needs to be validated and must be able to be applied in dense particle beds like mills, crushers or "cold" fluidised beds.

1.4 Outline

Chapter 2 reviews the literature in the field of fluidisation engineering in general and in particular on the particle degradation in fluidised beds. Later one further elaborates on drying, thermochemical and mechanical particle degradation in fluidised beds. Furthermore, this chapter gives a very brief overview of the research needs in this area recommended by other authors.

Chapter 3 gives a brief summary of the simulation software MultiFlow which has been used for all simulations in this work. This numerical framework has been developed before the start of this project. General equations to solve the gas and solid phase are provided with an emphasis on closure relations such as the interphase momentum transfer and the inter-particle interactions.

Chapter 4 focuses on implementing and validating one dimensional grain models into MultiFlow. The technique has been put forward to model many large particles in a fluidised bed dryer. The roasting process of coffee beans has been selected to compare available experimental results with model predictions. This model technique has proven to be able to provide much more information than state-of-the-art coffee bean roaster models.

Chapter 5 looks into fast pyrolysis of single large and many small biomass particles. This chapter covers highly novel and unprecedented results for the prediction of thermochemical particle degradation process in fluidised beds. Drying and shrinking has been considered additionally and results are discussed on their

[1]The number of breakage events, the number of allowed fragments and the smallest fragment size might have significant effects on the computational feasibility of DEM simulations.

dependence on different bed temperatures, particle moisture contents and fluidisation behaviour.

Chapter 6 presents the development of a novel discrete fragmentation model for brittle particles. The model is validated and outcomes have been compared to trends described in the literature. It is able to predict fragment size distributions and fragment velocities. It is highly suitable to be applied in dense particle beds like mills, crushers or fluidised beds.

Chapter 7 summarises the main conclusions drawn throughout this thesis. Some suggestions are made for further future work which are discussed again for drying, thermochemical and mechanical particle degradation in dense beds. This chapter also suggests future work required to model combined thermochemical and mechanical particle degradation processes.

Appendix A contains the general discretisation procedure for unsteady and one dimensional transport equations implemented and used in this work for modelling large particles. Energy and species transport are applied to this general discretised transport equation.

Chapter 2

Literature Review

This chapter covers briefly the major work carried out in the field of DEM modelling particularly related to particle degradation, fluidised bed applications or both together which are discussed thoroughly within this thesis. First, a general overview is given on fluidised bed modelling with the DEM approach. Both sections, the drying of large particles and thermochemical particle degradation, are reviewed by discussing first the major work done on single particle modelling and the discussion is then extended to dense beds and its applications and their specific research activities. Breakage as the main fragmentation mechanism of interest studied by different authors has been briefly categorised to highlight present research needs and achievements in the field. This chapter finishes with the main conclusions derived from this literature review.

2.1 Modelling Fluidised Beds with DEM

The discrete element method was first proposed by Cundall and Stack [29] in 1979 and coupled to the fluid phase in 1993 by Tsuji et al. [30] for the soft-sphere and 1996 by Hoomans et al. [31] for the hard-sphere method. Both methods can be used to describe inter-particle collisions. Hard-sphere collisions are event-driven, binary and instantaneous. Hard-sphere models are considerably faster but cannot account for multiple collisions at the same time which is required when modelling dense gas-particle systems such as fluidised beds. The hard-sphere method is impractical for dense fluidised beds due to frequent and continuous contacts between particles and should not be used under such conditions [32]. In particular simulations considering cohesive forces or low coefficients of restitution

require soft-sphere models. For that reason the soft-sphere method has been chosen for the work of this thesis. These collisions are time-driven and require a particle-particle or particle-wall overlap. This overlap needs to be resolved over several time steps to ensure the conservation of energy which in turn makes the soft-sphere approach computationally expensive. Soft-sphere models which can be found in the literature mainly differ from each other in the contact force scheme that is used [33].

Two-dimensional simulations of fluidised beds with the soft-sphere approach have been modelled first by Tsuji et al. [30]. Xu and Yu [34] improved closure assumptions to correctly couple the gas-particle interaction force. More effort has been made to elucidate the dependence of fluidisation characteristics based on gas-solid flow patterns and particle forces and size and shape of mobile zones where particles can move in various flow patterns [35,36]. Bubble formation from a central jet in a fluidised bed has been compared between experiments and numerical investigations using DEM and the two-fluid model by Bokkers et al. [37]. They concluded that DEM is able to describe the bubble size and shape very accurately which provides a good basis to apply DEM to more complex situations. The bubble formation behaviour can be disturbed by the presence of liquid, high temperatures or reactions causing agglomerates and finally defluidisation, which has been studied by Wang and Rhodes [38, 39]. The same authors also extended their research efforts to study the particle motion near walls by means of 2D DEM simulations [40, 41].

DEM work has been extended to 3D first by Kawaguchi et al. [42] as far as the particle phase is concerned. Very general research on mixing and segregation of isothermal beds have been quantified with the so called Lacey mixing index in 2D [43] and 3D [44]. In 3D, DEM is particularly suitable to model large (Geldart D) particles mostly found in spouting bed applications [45–47], mills [48], silos/hoppers [49, 50], coaters [51] and other systems containing bulky granules. This is due to numerical reasons as discussed later with the help of eq. (3.14).

Fluidised bed modelling in 3D with DEM has been undertaken by Ye et al. [52] who studied the hydrodynamic behaviour of fine Geldart A particles. Kafui and Thornton [53] have applied 3D DEM fluidised bed modelling to spray granulation of Geldart A particles. Usually granulation is achieved by introducing a liquid binder allowing consolidation or agglomeration - however, their model is based on activation of surface energy instead of wetting. Granule formation and breakage has been investigated by this methodology. Limtrakul [54] studied a catalytic gas-solid spouted bed reactor process where the gas phase is resolved in 2D and the

solid phase is resolved in 3D and ozone conversion on iron oxide catalysts has been examined. Further literature work carried out in the field of particle degradation is discussed in the following subsections.

2.2 Drying of Large Particles

Small particles can be dried effectively and efficiently. Large particles are more difficult to process as water can remain in the particle centre while the surface might scorch by pyrolytic reactions producing a very undesired product. Large particles require longer drying times which can contribute to an inhomogeneous quality throughout a batch of particles. The main research aim is therefore to look at processes which handle larger particles.

Particle drying removes moisture to attain a moisture level low enough to impede the growth of microorganisms. Successful preservation of food or plant material may require drying to as little as 10% moisture or less. Drying is an energy intensive process. Theoretically, drying requires 2442 kJ of energy for every kilogram of moisture removed at 25^oC [55]. In practice, drying is performed often at temperatures around 100^oC, which requires roughly 50% more energy than this theoretical level due to the sensible heat of particles and air used for drying. For example, drying of one ton of fresh biomass with a moisture content of 50% down to 10% would require 1.5 GJ, representing about 18% of the energy content of the fresh biomass [55].

Wood as a porous medium contains moisture in two forms: free water within the pores and bound water absorbed in the interior structure of the material. Di Blasi [56] modelled the drying process of a single large wood particle taking into account convective transport of free liquid water and bound water diffusion. The temperature and water concentration profiles are resolved in one dimension along the particle radius. This is probably the most comprehensive work undertaken of a single particle study. Similar work has been carried out for single wood slabs by Perre et al. [57, 58] and Bryden et al. [59]. Latter ones have studied different thermal regimes: thermally thin, thermally thick and the thermal wave regime. The thermal wave regime is present when at least 20% of the solid core is still undried and at least 20% has been pyrolysed ensuring that both drying and pyrolysis occur simultaneously for a significant portion during thermochemical degradation [60]. They also pointed out the importance of shrinkage during drying

and pyrolysis. Another comprehensive drying study on a single particle has been performed by Zhang et al. [61] for lignite.

Fluidised bed drying is a gentle and efficient process to remove moisture in granular materials [10]. Particularly Geldart D particles are suitable to be dried in spouting or bubbling fluidised beds. Wood is a less common material to be dried in fluidised beds as particles are usually less spherical in shape to be readily fluidisable and due to higher energy requirements for fluid beds compared to other drying technologies. However, other solids require gentle drying. Some typical examples for coarse particles dried in fluidised beds are grain [62], fertiliser [63], nylon [64], bovine intestine for pet food [65], cork stopper [66], silica-gel [67], hazelnuts [68], resin [17], coffee beans and many more. Despite the fact that drying of coarse particles is heavily applied in industry, modelling of these processes has hardly been undertaken although these particles feature generally good properties to be modelled with the discrete element method.

Numerical investigations of applications containing many large particles at the same time (fluidised beds, fixed beds) are again hardly represented in the literature. Wurzenberger et al. [69] and Peters et al. [70, 71] have studied wood degradation (drying, pyrolysis, char combustion) in fixed beds where the bed is resolved in 1D and very limited bed heat transfer information has been obtained. Herein, detailed single particle information needs most of the computational power available leading to a very simplified overall fixed bed representation. DEM has been applied to improve the understanding of agitated vacuum drying processes containing glass beads or lactose [72]. Li and Mason [73] looked at the drying performance of polyethylene pellets inside gas-solid pneumatic transport lines using a 2D DEM approach. Temperature is assumed to be constant along the particle radius while the moisture distribution is based on a crust model. This crust model distinguishes between a dry outer particle crust and a wet inner core. The model computes the moisture flow rate through that dry core section and through the particle after all. Such a model is certainly not suited for all materials and particle sizes and to make such an approach more general, discretisation of both temperature and moisture concentration is desired.

Hamdullahpur et al. [2,9] have developed a quite comprehensive empirical fluidised bed particle model based on drying of wheat complemented by some experimental studies [74]. The numerical work is highly simplified in terms of the hydrodynamic bed behaviour, where the bed changes in 1D along the bed height only (plug flow assumed). The solid volume fraction has been set constant along the bed height

while bubble and interstitial gas phase change. Although, the gas quantity in bubbles and interstitial voids do generally affect the particle heat and mass transfer properties, this global representation lacks in accuracy as it cannot account for any local heat transfer effects.

To initiate some fundamental research in this field it is useful to restrict the work to one material only. In this case, a comparison with experimental work is readily achievable and specific information and potential optimisation suggestions can be derived. In the scope of this thesis, coffee beans have been further studied as one representative material to be dried in fluidised beds although any other aforementioned material could have been used instead. The advantage is the availability of material properties in the literature. Chandrasekar and Viswanathan [75] investigated underipe, ripe and overipe coffee samples and determined many physical properties. There is also general knowledge available about batch roasting of coffee beans [76] which has been put forward by many other authors [77–79] in simple and applied coffee roaster models. Most of these studies do resolve the temperature and water concentration gradient along the radius in one dimension. More effort has been undertaken to resolve a multi-layer coffee cherry which consists of the bean itself, a parchment, pulp and skin which has been modelled by Varadharaju et al. [80] and Ciro et al. [81]. All these studies assume a spherical shape of the coffee bean while Hernandez et al. [82] have extended a coffee drying model to a geometry of a prolate spheroid. All these models are used for single particles and heat and mass transfer coefficients are in the best case approximated to fluidised bed conditions. Also extended research has been made in the direction of monitoring the released volatiles during roasting and has been analysed by Yeretzian et al. [83].

2.3 Thermochemical Particle Degradation

Generally biomass particles in the size between 0.1 - 6 mm in diameter are most appropriate for bio-oil production in fluidised beds [84]. However, the thermochemical conversion behaviour for woody biomass differs substantially between particles roughly smaller than 1mm in diameter and particles bigger than that [85]. The thermochemical degradation of large particles is controlled by heat transfer while the conversion of smaller particles is kinetically controlled [86].

Extensive studies on the thermochemical degradation of large single spherical particles have been undertaken by Di Blasi [87] where an external heat transfer model

is used to replace fast-pyrolysis thermal conditions in fluidised beds. Di Blasi successfully analysed the char formation and the prevailing intra-particle transport phenomena of tar and gas and used favourably experimental results for validation purposes. Fast pyrolysis degradation of single cylinders has been studied by Authier et al. [88], Sadhukhan et al. [89] and Larfeldt [90]. In all cases, results are validated with experiments and good agreement is achieved. Conditions have been applied similar to those present in fast pyrolysis although the major extra-particle effects present in fluidised beds which change dynamically are not appropriately accounted for.

Papadikis et al. [91–93] carried out a series on fast pyrolysis simulations where the gas and sand phase are modelled by a two-fluid approach (Eulerian approach) and biomass is considered by means of very few (1-3) individual Lagrangian particles. Herein, any discrete biomass information is arbitrary, rather than statistically averaged over many continuously tracked biomass particles and particle-particle interactions are strongly simplified by considering artificially generated drag.

Particle heat-transfer [94], coal/char combustion [95, 96] and wood gasification [8] have been modelled with CFD-DEM, although the particle size in these studies are far bigger than the actual sand used in ordinary experimental beds. Rabinovich et al. [97] used a CFD-DEM model to study fast pyrolysis although the bed conditions used are strongly simplified (e.g. 500 sand particles). All these research efforts are restricted to small computational domains and the conditions used are not comparable to ordinary experiments.

Peters [98, 99] developed numerical approaches to describe the thermal conversion of wood on moving grate furnaces during fixed bed combustion. Raupenstrauch and co-workers [69] also developed fixed bed combustion models. Both methods are strongly simplified where the bed is modelled in 1D and very limited bed heat transfer information have been obtained. Future work is mainly targeted towards a full resolution of a 3D bed model by means of DEM. So far, DEM has only been applied to predict the heating of packed beds [100, 101] without considering aspects of particle degradation or chemical reactions.

Geng and Che [102] used the DEM to study combustion of char in bubbling fluidised beds. Although strong simplifications have been made (e.g. disregarding turbulence for gas phase reactions) this model seems to be very promising for advanced modelling of particulate combustion in fluidised beds.

Fast pyrolysis has also been studied with the help of Euler-Euler simulations where the solid phase is updated based on the kinetic theory of granular flow. Bellan and co-workers have looked at fast pyrolysis in vortex [103] and fluidised bed [104] reactors and obtained rather general particle phase information where the main features of the pyrolysis process have been captured. Recently, Xue et al. [105] also performed Euler-Euler simulations for 200 seconds of operation. However, their novel contribution is rather limited and any validation with experimental data have been postponed to future work.

Present research needs in the field of fast pyrolysis modelling have been summarised by Di Blasi [106]. These needs are, amongst others, related to (1) more detailed inclusion of extra-particle processes, (2) the accurate prediction of conversion times and global decomposition rates, (3) incorporation of structural changes of biomass, dependence on physical properties on conversion conditions and detailed mechanisms of pyrolysis reactions. Furthermore, the ejection mechanisms and the origin of ejected particles from the bed into the freeboard can be crucial and have only been postulated while further studies are needed to elucidate particle entrainment [107]. DEM may have potential to overcome these shortcomings because it is a flexible framework, however this will require development and validation of accurate sub-models.

Nemtsov and Zabaniotou [26] concluded that only limited research has been performed to investigate the hydrodynamics of biomass particles in fluidised beds to carry out pyrolysis, gasification and combustion. They further highlighted that more effort needs to be carried out to provide general understanding of interactions among heterogeneous particles and guidance on conditions that can lead to viable and sustainable processes.

The reader is referred to more comprehensive review articles on modelling thermochemical particle degradation of biomass. Di Blasi [106], Kersten et al. [108] and Babu and Chaurasia [109] have reviewed pyrolysis and Nemtsov et al. [26] and Gómez et al. [28] summarised activities in the field of gasification.

2.4 Particle Breakage

Particle size reduction occurs in many engineering applications and requires a good understanding when it comes to process design optimisation. The discrete element method is particularly adaptable for a variety of fragmentation applications and

has been applied to particle comminution [110], blasting [111] and attrition [112]. Fragmentation can also reasonably well categorised based on the degree of breakage which increases with the amount of strain energy [113, 114] and strain rate [114, 115] applied. Strain energy is stored within an elastic solid when the solid is deformed under load and represents a type of potential energy. DEM-models for static (slow) stresses are widely applied in biaxial (2D) or triaxial (3D) tests for single global particles [116–118] and for a few crushable agglomerates [119, 120]. DEM-modelling of dynamic impact-induced fragmentation has been introduced by Potapov et al. [113] and has been brought forward to model particle breakage in tumbling mills [121]. In the latter model, particles are glued together in tetrahedra elements which detach during potential fragmentation. Inherently, this approach is computationally expensive and seams to be unfeasible when it comes to scale-up or modelling of repetitive fragmentation.

Almost all discrete element models describing fragmentation adopt an agglomeration framework [110–121], where each parent particle consists of a number of smaller child particles. During the course of a simulation, the child particles can be separated from the parent particle to represent a fragment. The advantage of this approach is its simplicity in concept and implementation. The drawback of the approach is the limitation in the number of particles and the size distribution of fragments, as all fragments must consist out of the initial particles.

An alternative to the agglomeration framework is the discrete fragmentation method (DFM). In DFM models the number and size of the progeny is derived at the moment of breakage and replaces the parent particle. The advantage of this approach is the flexibility to produce any number and size distribution of fragments. The drawback is the increased complexity in describing the parent and child particles. The discrete fragmentation method combines accuracy and efficiency to cope with large particle numbers being favoured to model most applications containing granular materials. As far as the author knows, Cleary [122] is the only one who introduced a discrete fragmentation model. He stated that the actual rules used in his code are still crude (e.g. mass is not necessarily conserved) and progress beyond fragmentation involving high speed balls in cataracting streams is desired. No further detailed description of his model has been published lately.

Breakage due to thermal stress during drying of silica particles has been investigated by Mezhericher et al. [123]. Fuel particle fragmentation during pyrolysis, gasification or combustion depends on several factors such as coal rank, initial porosity, size of particle, combustion mode and system [124]. Zhang et al. [125]

point out that the coal rank influences fragmentation most intensely of all factors. As outlined by Sudhakar et al. [126] wood has a higher volatile content (70-75%) compared to coal (30-40%) leading to build-up of high volatile pressure as proposed by Hastaoglu et al. [127] for wood pellets. He argued that wood has a more fragile mechanical structure than coal due to very high wood char porosities and charred wood is more susceptible to primary and secondary fragmentation. Although there is little research of wood particle breakage [127, 128] this field has not been tackled with DEM yet. However, due to the complexity in modelling discrete breakage due to thermal stresses, this research field is difficult to tackle in the near future.

2.5 Aspects of Numerical Limitations

Van der Hoef et al. [5] compared different modelling strategies, in particular Eulerian and Lagrangian models, for the application to fluidised beds. Herein, two-fluid models are classified for the use of engineering scales (fluidised beds roughly 1m in height) while DEM models are categorised into the laboratory scale level (fluidised beds of roughly 0.1m). The computational cost for the Eulerian approach is comparably small of similar size as particles are treated as a continuum phase and inter-particle forces are taken into account by a closure model (the Kinetic Theory of Granular Flow). Particle properties are always cell volume averaged and important information is either lost (e.g. trajectory, residence time) or blurred (any particle property is averaged). If properties of certain particles are required to be distinguishable, a new phase has to be introduced (multi-fluid approach). The computational cost of Eulerian multiphase flow models increases rapidly with an additional considered phase as a set of new eqs. (3.1, 3.2, 4.1, 4.2) is solved.

If all dimensions of a rectangular domain are doubled, it contains 8 times more particles of the same size. The number of particles are four times larger when a cylinder's diameter is doubled. The scale of the computational effort in DEM models is expected to be proportional to $NlogN$ [129,130], where N is the number of particles in the simulation. More importantly, the particle size, mass, stiffness and velocities expected in the simulation matter substantially. They are related in a non-linear way to the collision time in eq. (3.14) which in turn is coupled to the time-step used. When the force-displacement interaction is not fundamental, the stiffness can be reduced (larger overlaps) to achieve larger time-steps useful for quicker simulations of global granular trajectories [131]. The particle phase

is always updated in an explicit way and requires generally smaller time-steps compared to the implicitly solved fluid phase. In dense particle systems, the fluid phase (number of mesh cells, etc.) is only a small fraction of the overall computational demand required.

Xue et al. [105] have modelled fast pyrolysis in the fluidised bed reactor similar to the one discussed in Chapter 5 in the Euler framework. The comparison in terms of computational demand and complexity is given in Table 2.1. However, shrinkage during pyrolysis, drying and entrainment has not been considered. Validation with experimental work has been postponed to future work. Chapter 5 discusses a fluidised bed reactor of the smallest scale present in laboratories at the moment (experimental data available). Table 2.1 states that for such Lagrangian models the simulation time and computational expense are large. Simulations of larger reactor sizes are difficult. Bubbling fluidised beds are currently scaled up to use feeding rates of e.g. 100t/day (DynaMotive, Vancouver [21]), which is approximately 40,000 times (based on the feeding rate) as big as the reactor discussed in Chapter 5. The DEM approach is certainly not suited to model such reactors but has the potential to be a helpful tool in deriving constitutive correlations for the use in other simulation methods.

Both, Lagrangian and Eulerian models still require gas-particle closure models (e.g. Wen and Yu drag correlation) and therefore the fluid mesh resolution compared to the particle size should be similar. However, as the domain of Euler-Euler simulations are usually larger in scale, they have many more mesh cells and the coarse mesh appears much smaller compared to the overall domain size. In both approaches, solid particles do not exclude volume from any fluid mesh cell. The particle volume is artificially considered by using $\epsilon\rho_f$ or $\epsilon\overline{\overline{\tau}}_f$ instead of ρ_f or $\overline{\overline{\tau}}_f$ in eqs. (3.1) and (3.2) [5]. Fluid cells become more or less permeable. The Immersed Boundary approach is able to model these gas-particle interactions (without a closure model) and is therefore suitable to resolve the flow between individual particles (the flow close to the particle surface can be accounted for). This method is very expensive and only applicable to very tiny scales.

2.6 Conclusions

DEM is a very powerful approach to investigate the details of flow phenomena prevailing in granular flows. Unfortunately, there is an extreme lack of DEM modelling encountered during this literature review dealing with particle degradation

TABLE 2.1: Comparison between an Eulerian and Lagrangian model for the simulation of "basically" the same reactor. Different biomass feedstocks and fluidisation conditions apply. (ODE= ordinary differential equation, PDE=partial differential equation)

	Euler model (Xue et al. [105])	Lagrangian model (Chapter 5)
Dimensions	2D	3D
Reactor size	d=3.81cm, h=34.29cm	d=3.81cm, h=46.0cm
Stagnant bed height	7.04cm	6.3cm
Fluid mesh cells	940	99360
Fluid cell size	3.8x3.8mm	≈1.6x1.6x2mm
Gas phase species	N_2, tar, gas	N_2, tar, gas, H_2O
Sand phase eqs.	2 PDEs	2 ODEs for 600711 particles each
Biomass phase species	C,H,L,AC,AH,AL,Char,void	C,H,L,AC,AH,AL,Char,H_2O
Volume reduction	void species in particle	by shrinkage
Biomass eqs.	4 PDEs in total + 9ODEs per cell	12 ODEs for max. 188620 particles each
Time-step	$7{\cdot}10^{-4}$ sec	$5{\cdot}10^{-5}$ sec
Computer	serial run, Dell Precision T7400	HECToR Phase 2a (2.3GHz, 192 cores)
Simulated real time	200 sec	10 sec
Simulation time	144 CPU hours	400,000 CPU hours

in dense beds and the potential of this approach to optimise such systems remain unused to a large extent ever since. As pointed out by Yu and Xu [36], gas-solid flow modelling difficulties are mainly related to the solid phase rather than the gas phase. Therefore, further research and innovations are important to be made on the solid phase where DEM can be a very helpful tool to address shortcomings of previous research. Furthermore, Deen et al. [32] highlighted that for many engineering applications three dimensional modelling is required to incorporate all necessary details. They requested that more applied research is needed to be undertaken in three dimensions. As found throughout this literature review, most DEM studies are based on very simplified or small particle beds and more research is desired which tackle large scale simulations. As an example, most fluidised bed DEM studies consider very large inert particles to reduce the computational demand although the sand used in most applications is much smaller.

Very little research effort has been made on DEM modelling of large particle drying. So far, however, no DEM study includes sub-particle scale modelling of heat and mass transfer effects with detailed resolved inter-particle interactions often required for simultaneous mixing and segregation studies of numerous particles. Much potential is available to further optimise such systems. The drying/roasting process of coffee beans in bubbling fluidised beds is one of such examples. DEM is potentially able to provide information from the flow and particle level which is not possible to get from state-of-the-art coffee roaster models.

Fast pyrolysis modelling of single biomass particles has been comprehensively analysed. However, throughout the literature, modelling the thermochemical biomass particle degradation in fluidised beds lacks either in a representative reactor size, the number of new information, applicability or validity. Research needs in the field are amongst others: inclusion of extra-particle effects, global conversion times[1] and decomposition rates and hydrodynamic behaviour of biomass in sand. DEM is very well suited to tackle these issues and is therefore the most favourable method in modelling fast pyrolysis.

Modelling particle breakage is important as it can be encountered in many engineering applications. There is not a single discrete fragmentation model described in the literature which consistently obeys the conservation of mass, momentum and energy. Other empirical or discrete agglomerate models are limited in the depth of information they supply, or they encounter difficulties when applied to larger

[1]Global conversion times refer to experimentally measurable data, that means the time period particles remain in the reactor, are mainly degraded or the gas/particle composition reaches steady-state at the reactor outlet.

applications. Mechanical breakage is often encountered and models are easier to validate than breakage models for thermal breakage. Therefore, the development of a new discrete fragmentation model based on mechanical failure criteria would be an important and achievable contribution, providing valueable solutions leading to further technology improvements.

Chapter 3

MultiFlow

MultiFlow (www.multiflow.org) is a curvilinear, fully coupled CFD solver containing different simulation modules applicable to multiphase flows and has been developed by Berend van Wachem's research group. Only its Eulerian-Lagrangian module is used and discussed troughout this work. Mfix, OpenFoam, MultiFlow and other commercially available codes such as PFC3D or EDEM have been compared. Although MultiFlow is a relatively young and still fairly unknown code it has the advantage over most others that the code (including its Lagrangian part) is made fully parallel with MPI libraries and simulations can be carried out on the UK national supercomputer HECToR or on the supercomputer at the University of Southampton called Iridis3. The message passing interface (MPI) has been used via MPICH on all computer platforms used (HECToR, Iridis3, local machine). For details on MPI, the reader is referred to the literature [132]. For a more detailed description of the fluid solver, discretisation of governing equations, etc. the reader is referred to the MultiFlow user manual [133].

3.1 Fluid Phase Modelling

The fluid phase is modelled as a continuum, known as an Eulerian type model. The fluid phase continuity and momentum transport equations are solved on the computational cell-level. The continuity equation is given as:

$$\frac{\partial(\epsilon\rho_f)}{\partial t} + \nabla \cdot (\epsilon\rho_f \vec{u}_f) = S, \tag{3.1}$$

and the Navier-Stokes equation is modified two-fold, firstly it contains the fluid volume fraction and secondly an interphase momentum transfer term so that the momentum transport equation reads:

$$\frac{\partial(\epsilon\rho_f\vec{u}_f)}{\partial t}+\nabla\cdot(\epsilon\rho_f\vec{u}_f\vec{u}_f) = -\epsilon\nabla P+\nabla\cdot(\epsilon\overline{\overline{\tau}})+\rho_f\epsilon\vec{g}-\sum_{i=1}^{n}\beta(\vec{u}_f-\widetilde{\vec{u}_{p,i}})\delta(x-x_{p,i})+S\vec{u}_f, \tag{3.2}$$

where ρ_f, $\vec{u}_f$, P, $\vec{g}$ and S are the fluid density, the fluid velocity vector, the local normal pressure, gravity vector and source term respectively and ϵ is the fluid volume fraction defined as:

$$\epsilon = 1-\sum_{i=1}^{n}\frac{V_{p,i}}{V_{cell}}. \tag{3.3}$$

The shear stress tensor $\overline{\overline{\tau}}$ depends on the fluid viscosity μ_f, the Kronecker delta δ_k and the fluid bulk viscosity λ'_f. The later one can be neglected for Newtonian fluids (e.g. air) which is referred as the Stokes' assumption.

$$\overline{\overline{\tau}} = \mu_f\left(\nabla(\vec{u}_f)+\nabla(\vec{u}_f)^{-1}\right)+\delta_k\left(\lambda'_f-\frac{2}{3}\mu_f\right)\nabla\vec{u}_f. \tag{3.4}$$

The fourth term on the right hand side of eq. (3.2) is used for the momentum coupling between the fluid and particle phase where $\widetilde{\vec{u}_p}$ is the particle velocity as seen by (interpolated to) the fluid phase and n is the number of particles in a computational fluid cell. The term $\delta(x-x_{p,i})$ represents the Dirac delta function, ensuring the momentum transfer is considered only at the particle locations [11]. Generally, the interphase momentum transfer coefficient β takes into account form and skin drag and is an empirical parameter which is typically derived from experiments on a scale far bigger than it is applied in simulations. Therefore, any closure relation (which is equally valid for e.g. heat and mass transfer correlations such as Nu or Sh) is crucial in modelling multiphase flows. However, the Wen and Yu drag correlation [134] has been found to be preferred over others [135] and is therefore used for all simulations in this thesis. This correlation is valid over a wide range of solid volume fractions ($0.01 \leq \epsilon_s \leq 0.63$) and is expressed as:

$$\beta = \frac{3}{4}C_D|\vec{u}_f-\widetilde{\vec{u}_p}|\frac{\rho_f(1-\epsilon)(\epsilon)^{-1.65}}{d_p}, \tag{3.5}$$

with

$$C_D = \begin{cases} \frac{24}{\epsilon Re_p}\left(1+0.15(\epsilon Re_p)^{0.687}\right) & \text{if } \epsilon Re_p < 1000, \\ 0.44 & \text{if } \epsilon Re_p \geq 1000. \end{cases}$$

The gas flow is assumed to be laminar throughout any study in this thesis as

turbulence is suppressed due to the presence of particles in fluidised beds even for moderately high Reynold numbers (<2000) [5] and the particle motion in the freeboard is assumed to be controlled by splashing rather than turbulent diffusion [136]. In this work, no chemical reactions are considered in the gas phase so that there is no specific need to resolve turbulence.

A collocated finite volume method is used to predict the fluid flow field - using Rhie and Chow interpolation [137] for the stabilisation of pressure and velocity coupling. Second-order backward Euler time discretisation is used, while spatial discretisation is achieved for non-convective terms by the second-order central difference scheme and convective fluxes are approximated by a second-order upwind scheme. All partial differential equations are solved in a fully coupled manner, where the subset of linearised equations is solved by an additional stabilised version of the Krylov Subspace Method (BiConjugate Gradient Squared).

Boundary conditions are generally applied (for all presented simulations) as follows. At walls, adiabatic and slip boundary conditions are applied. Dirichlet boundary conditions are employed at the inlet with a constant fluid velocity, temperature and species mass fractions. The boundary condition at the fluid phase outlet is a so-called pressure outlet. The pressure at this boundary is fixed to a reference value of $1.013 \cdot 10^5 Pa$. Neumann boundary conditions are applied for the fluid velocity, temperature and species mass fractions requiring a fully developed fluid flow. This is because the outflow boundary condition assumes a zero normal gradient for all flow variables except pressure and the solver extrapolates the required information from interior.

In this thesis, only larger particles (Geltard B or D) are modelled in dense fluidised beds. Any flow in these fluidised beds is strongly dominated by the particles. For fluid flow conditions under consideration, the Stokes number is large and particles are therefore insensitive to the exact boundary layer. Also, the fluid boundary layer will have hardly any effect on the pressure drop, as the majority of the pressure drop is expected to come from particle drag forces. A boundary layer is also difficult to consider from the numerical point of view (e.g. that the fluid cell cannot be too small for discrete particles) and has not been considered for such reasons.

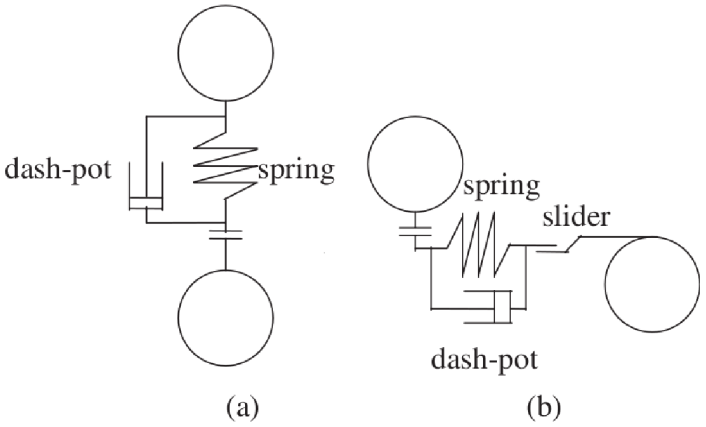

FIGURE 3.1: Particle contact forces a) normal force b) tangential force [73]

3.2 Particle Phase Modelling

The translational and rotational particle motion is modelled by the discrete element method at an individual particle level by using Newton's second law of motion according to eqs. (3.6-3.7).

$$m_p \frac{d\vec{u}_p}{dt} = \frac{V_p \beta}{(1-\epsilon)}(\widetilde{\vec{u}_f} - \vec{u}_p) - V_p \nabla P + V_p \nabla \cdot \bar{\bar{\tau}} + \vec{F}_g + \sum_{col} \left(\vec{F}\right) \tag{3.6}$$

$$I_p \frac{d\vec{\omega}_p}{dt} = \sum_{col} \left(\vec{T}\right) \tag{3.7}$$

where $\vec{u}_p$ and $\vec{\omega}_p$ are the translational and rotational particle velocity vectors, P is the local normal pressure, $\bar{\bar{\tau}}$ is the local gas phase shear tensor, $\vec{F}_g$ includes gravity and buoyancy forces, $\widetilde{\vec{u}_f}$ represents the undisturbed local fluid velocity, $I_p = \frac{2}{5} m_p r_p^2$ is the moment of inertia and $\vec{T}$ is the torque acting on that particle. In most cases, the magnitude of the gas-phase shear tensor is not significant and its contribution can be safely omitted, as it is an order of magnitude smaller than the pressure drop [11]. Soft-sphere inter-particle and particle-wall collision forces $\sum_{col} \left(\vec{F}\right)$ or $\sum_{col} \left(\vec{T}\right)$ are modelled by using a combination of a spring, dashpot and slider approximation (see Figure 3.1). The spring provides an elastic restoration force, the dashpot dissipates energy during contact due to irreversible plastic or visco-elastic deformation while the magnitude of tangential force is limited by the sliding friction element. A non-linear Hertzian spring model combined with a dampening model for the normal direction is used according to Tsuji et al. [138] and a model representing the tangential forces during impact is based on Mindlin and Deresiewicz [139]. Normal and damping forces are summarised in Table 3.1,

where $\vec{F} = \vec{F}_{en} + \vec{F}_{dn} + \vec{F}_{et} + \vec{F}_{dt}$ and $\vec{T} = (\vec{F}_{et} + \vec{F}_{dt}) \times \vec{n}$. The overlap δ_n between particle i and j during a collision is determined from the particle location and size and can be thought of as the displacement or deformation magnitude. In case the tangential force acting on a particle reaches a certain limit, the particle begins to slide and a different force is applied. Soft-sphere DEM models require four parameters which need to be specified, namely the coefficient of friction (μ), the stiffness (k), the damping coefficient (η) and the coefficient of restitution (e). The last three are correlated in the following equations:

$$\eta_n = \alpha\sqrt{m^* k_n}\delta^{1/4}, \tag{3.8}$$

$$\eta_t = \alpha\sqrt{m^* k_t}\delta^{1/4}, \tag{3.9}$$

where $m^* = \frac{m_i m_j}{m_i + m_j}$ and m is the particle mass. For wall collisions $r_w \to \infty$ and $m_w \to \infty$, hence $m^* = m_p$. The particle momentum changes in tangential and normal direction during a wall collision. For both particle-particle and particle-wall collisions two different coefficients of restitutions have to be specified.

The spring constants are based on elastic deformation according to

$$k_n = \frac{4}{3}\left(\frac{1-\nu_i^2}{E_i} + \frac{1-\nu_j^2}{E_j}\right)^{-1}\left(\frac{r_i + r_j}{r_i r_j}\right)^{-\frac{1}{2}}, \tag{3.10}$$

$$k_t = 8\left(\frac{2-\nu_i}{G_i} + \frac{2-\nu_j}{G_j}\right)^{-1}\left(\frac{r_i + r_j}{r_i r_j}\right)^{-\frac{1}{2}}\delta_n^{\frac{1}{2}}. \tag{3.11}$$

The relationship between α (a scalar for energy dissipation relation) and the coefficient of restitution is well defined by Tsuji [138]. From Newton's law of restitution [140], e is also defined as:

$$e = -\frac{u_\infty}{u_0}, \tag{3.12}$$

where u_0 and u_∞ are the normal components of relative velocities before and after the collisions.

The coefficient of restitution e, which determines the particle elasticity, can be strongly reduced in case of wet particles which are often encountered in several fluidised bed processes [141]. In case of fully elastic collisions ($e = 1$), particles would not lose any energy during collisions as it is encountered in molecular dynamics. In case of inelastic collisions ($e < 1$) of granular materials, energy is dissipated and dense particle regions tend to cluster, forming dense regions next

TABLE 3.1: Normal and tangential forces between particle i and a collision partner j (particle or wall). The explanation for the symbols can be found in the Nomenclature.

Forces	Symbol	Equation
Normal elastic force	$\vec{F}_{en}$	$-\frac{4}{3}E^*\sqrt{r^*}\delta_n^{3/2}\vec{n}$
Normal damping force	$\vec{F}_{dn}$	$-\alpha\left(\frac{4}{3}E^*m^*\sqrt{r^*\delta_n}\right)^{0.5}v_{rn}\vec{n}$
Tangential elastic force	$\vec{F}_{et}$	$\begin{cases} -8G^*\sqrt{r^*\delta_n}\vec{u}_{slip}\Delta t & \lvert\vec{F}_t\rvert \le \lvert\vec{F}_n\rvert\mu_{ij} \\ (\lvert\vec{F}_{en}+\vec{F}_{dn}\rvert)\frac{\mu_i+\mu_j}{2}\frac{\vec{\delta}_t}{\lvert\vec{\delta}_t\rvert} & \lvert\vec{F}_t\rvert > \lvert\vec{F}_n\rvert\mu_{ij} \end{cases}$
Tangential damping force	$\vec{F}_{dt}$	$-\frac{\mu_i+\mu_j}{2}(8G^*m^*)^{0.5}(r^*\delta_n\delta_t)^{0.25}\vec{u}_{slip}$
Gravitational/buoyancy force	$\vec{F}_g$	$\frac{\pi}{6}(\rho_p-\rho_f)d_p^3\vec{g}$

$\frac{1}{E^*}=\frac{1-\nu_i^2}{E_i}+\frac{1-\nu_j^2}{E_j}$; $\frac{1}{G^*}=\frac{2-\nu_i}{G_i}+\frac{2-\nu_j}{G_j}$; $G_x=\frac{E_x}{2(1+\nu_x)}$ with $x=i,j$
$Re_p=\frac{\rho_f d_p\lvert\widetilde{\vec{u}_f}-\vec{u}_p\rvert}{\mu_f}$; $\delta_t=\vec{u}_{slip}\Delta t$
For particle-particle interactions:
$\vec{u}_{slip}=\vec{u}_{r,ij}-v_{r,n}\vec{n}+\vec{\omega}_i\times r_i\vec{n}+\vec{\omega}_j\times r_j\vec{n}$; $\frac{1}{m^*}=\frac{1}{m_i}+\frac{1}{m_j}$; $\frac{1}{r^*}=\frac{1}{r_i}+\frac{1}{r_j}$
For particle-wall interactions:
$\vec{u}_{slip}=\vec{u}_i-u_{i,n}\vec{n}+\vec{\omega}_i\times r_i\vec{n}$; $m^*=m_i$; $r^*=r_i$

to dilute regions and form bubbles. The particle stiffness is often set to lower values than that of the material used, ensuring that the normal overlap is kept small and the predicted hydrodynamic behaviour is not affected. Mikami et al. [142] argued that once particles collide sufficiently often they behave like a continuum and, accordingly, the computed results are not sensitive to these parameters. For that reason, different authors [143, 144] have used relatively large overlap values when modelling fluidised beds.

Collisions need to be solved over multiple particle-time-steps which are dependent on the collision time t_{coll} and the number of time-steps to describe a collision K as [144]:

$$\Delta t_p = \frac{t_{coll}}{K}, \tag{3.13}$$

where t_{coll} is approximated according to:

$$t_{coll} \approx 2.94\left(\frac{5}{4}\frac{m^*}{E^*(d^*)^{0.5}}\right)^{2/5}u_{bi}^{-1/5}. \tag{3.14}$$

The asterisk is indicating relative properties as given in Table 3.1 and u_{bi} is the particle velocity before impact. Newton's law is solved with this variable time-stepping routine by the well known Verlet scheme [145]. When the particle phase is updated, the fluid-phase equations (section 3.1) are solved. This indicates that the

explicit update of the particle-phase has a much smaller time-scale compared to the implicitly solved fluid-phase. It can be seen from eq. (3.14), that the collision time increases when larger, heavier, softer and slower particles are considered in the simulation. Larger particle time steps lead to faster computational performance.

As mentioned above, the particle phase is updated with a variable time-stepping routine ensuring that the motion of particles is always fully resolved. This is why throughout this thesis no particle time-step has been specified. The fluid time-step has been chosen to be (10^{-2}) for all single particle studies (as mainly constant fluid properties for the sake of simplicity in comparison are chosen). The 1D sub-particle model has shown perfect agreement with analytical solutions during heat transfer and is not sensitive to the chemical reaction time scales and therefore depended on the fluid time-step (see Figure chemicalts). Furthermore, the overall real time modelled is huge compared to the fluid time-step (Figure 4.5a). For fluidised bed studies the fluid time-step is chosen much smaller (up to $5 \cdot 10^{-5}$ seconds). Fragmentation is event driven and therefore time-step independent.

3.3 Mesh generation, coupling and data storage

Most Eulerian-Lagrangian models are designed with a multi-grid approach, when inter-particle contact models are considered (efficient search for collision partners). In MultiFlow, the Cartesian particle grid cell is of the order of the biggest particle in the simulation while the fluid grid cell is usually 3-8 times bigger than the particle cell. The length-scale of the fluid cell need to be fine enough to capture the size of the smallest particle clusters (e.g. at the bubble surface in dense beds) but need to be big enough to ensure a correct prediction of the particle-fluid interaction force (volume fraction, interphase momentum transfer coefficient). Particle clusters can play a role in the stress behaviour of the overall solid phase and if the fluid length-scale becomes too big, the difference between the actual physics and the model prediction grows. As a consequence, to achieve highly accurate gas-solid interaction forces, the gas-phase in Euler-Lagrangian simulations is solved on a fairly coarse grid, possibly reducing the accuracy of the gas-flow.

Fluidised beds are dense and completely dominated by particles. Especially because the particles are big (Geldart B or D) with high Stokes numbers. The fluid flow is therefore mainly influenced by the fluid-particle interaction forces (drag + pressure gradients). This affects the size of the fluid mesh in the first place. Any

simulation in the thesis is kept to the lower limit (roughly 3 particle dimensions), so that any other mesh constellation is expected to have a negative influence.

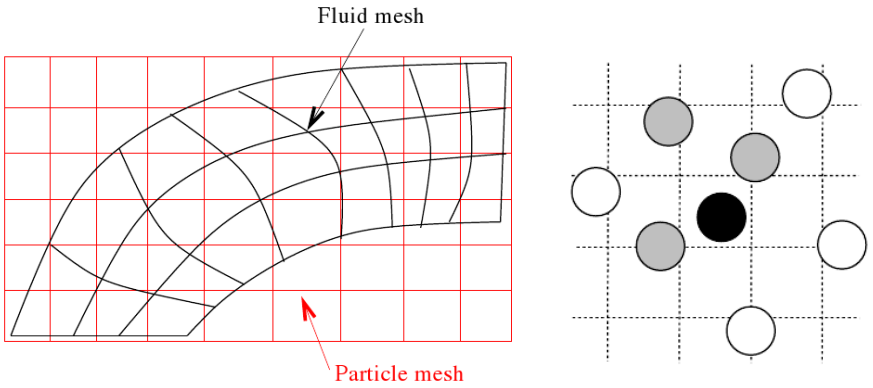

FIGURE 3.2: a) Overlapping fluid mesh with cartesian particle mesh and b) Particle mesh to find particle collision partners [146]

A Cartesian, homogeneous particle mesh is coupled with the fluid mesh and goes beyond the fluid mesh boundaries to ensure that every particle belongs to one single particle mesh cell (Figure 3.2a). Particles in the same and neighbouring particle cells are potential collision partners only (gray particles in Figure 3.2b) to find quickly current and potential collision partners.

The particle mesh is always self generated by MultiFlow. The fluid mesh needs to be generated by ANSYS ICEM-CFD and consists of one or multiple blocks. As MultiFlow is a curvilinear flow solver, topologically regular but geometrically irregular arrays of points are needed. This requires a hexahedra mesh in 3D. To achieve high computational performance with multiple processors, the goal is to partition the computational load if possible uniformly over available processors.

Interpolation between the fluid cell centre values (collocated grid arrangement) and the solid particles is achieved by four sub-interpolation steps described below (for details see [133]):

3.3.1 Interpolation from fluid cell to particle cell

The variables present in a collocated variable arrangement on the fluid phase mesh are interpolated to the corners of the particle mesh. As the fluid mesh is generally not Cartesian, this is done by so-called Shepard's interpolation between all fluid

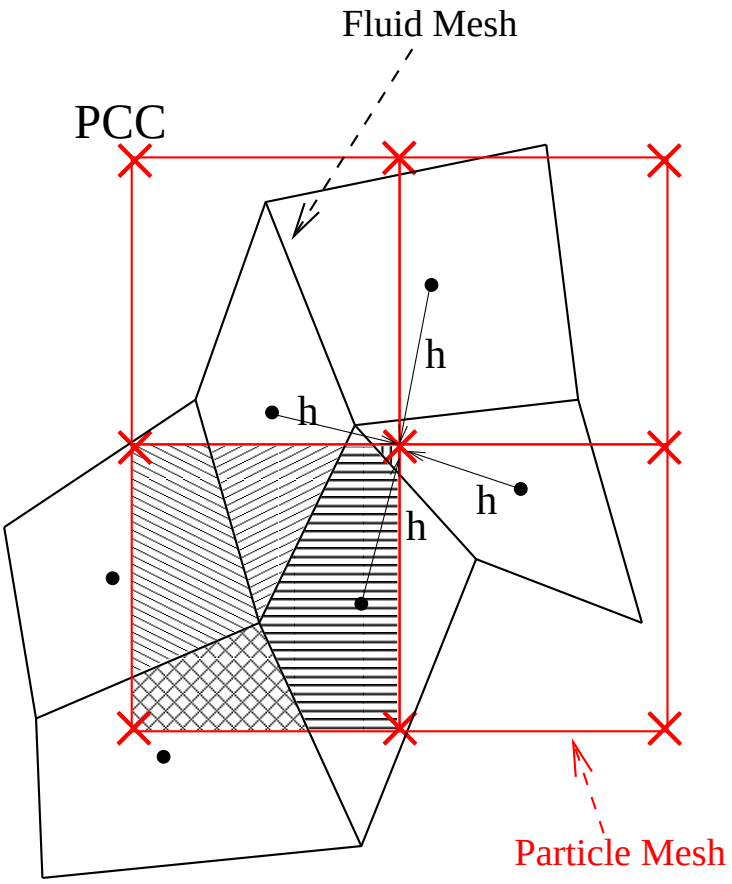

FIGURE 3.3: A few fluid mesh cells and a few particle mesh cells. The fluid properties are interpolated to the corners of the particle mesh. The particle mesh properties are interpolated to the underlying fluid cells using the relative volumes (filled). [133]

mesh cells neighbouring the particle mesh cell corner (PCC).

$$\phi_{PCC} = \sum_{i=1}^{NB} w_i \phi_i, \tag{3.15}$$

where the weighting coefficients w are given by

$$w_i = \frac{h_i^{-2}}{\sum_{j=1}^{NB} h_j^{-2}}, \tag{3.16}$$

and where h_i is the length of the line connecting the particle mesh corner to the neighbouring fluid mesh cell, see Figure 3.3.

3.3.2 Interpolation from the particle cell to the fluid cell

The variables interpolated from the particle cell to the fluid cell are typically volume fraction or source term (body force) based. Therefore, the interpolation is done on a volume basis. At run-time, all fluid mesh cells occupying a part of the particle mesh cell volume, so that their relative contribution to the volume is determined. Per particle mesh cell,

$$\sum_{n=1}^{\text{fluid cells}} V_{r,n} = 1, \tag{3.17}$$

where $V_{r,n}$ is the relative volume of the particle mesh cell occupied by underlying fluid mesh cell n. When the relative volume is multiplied with the volume of a particle mesh cell, the actual volume is obtained.
A similar statement can be made for any fluid cell; as it is completely covered with particle mesh cells,

$$\sum_{l=1}^{\text{particle mesh cells}} V_{r,i}(l) V_{PC}(l) = V_i, \tag{3.18}$$

where $V_{r,i}(l)$ represents the relative volume of fluid mesh cell i occupying particle mesh cell l and V_{PC} represents the particle mesh cell volume. As the particle mesh is Cartesian, isotropic and homogeneous, V_{PC} is a constant throughout the domain.

There are two types of interpolation, (1) the interpolation of a scalar, such as temperature or a concentration, and (2) the interpolation of a force or flux. In the latter case, the units of the considered variable are different; the Lagrangian framework considers a Lagrangian particle whereas the Eulerian framework considers a PDE written in units per volume.

Considering the first case, let ξ be a scalar value, such as temperature or concentration. The value of a variable in fluid cell i determined from its particle mesh cell values thus becomes

$$\tilde{\xi}_i = \frac{1}{V_i} \sum_{l=1}^{\text{particle mesh cells}} V_{r,i}(l) V_{PC}(l)\, \xi(l), \tag{3.19}$$

where V_i is the volume of fludi mesh cell i. Hence, it should be noted that the units of ξ in the Lagrangian framework are the same as in $\tilde{\xi}$ in the Eulerian framework. For example, the temperature of the particle, expressed in K, should also be expressed in K in the Eulerian framework.

Considering the second case, let ϕ be a force or flux which is present in the Lagrangian framework. This quantity in the Eulerian framework, denoted as $\tilde{\phi}$, should now be expressed per volume. The easiest way to do this, is to express the quantity per particle cell volume and then perform an average, i.e.

$$\tilde{\phi}_i = \frac{1}{V_i} \sum_{l=1}^{\text{particle mesh cells}} V_{r,i}(l) V_{PC}(l) \frac{\phi(l)}{V_{PC}(l)} = \frac{1}{V_i} \sum_{l=1}^{\text{particle mesh cells}} V_{r,i}(l)\, \phi(l) \quad (3.20)$$

Note that in this case the units of ϕ and $\tilde{\phi}$ are not the same. For example, the momentum transfer is expressed in the units $\frac{kg\,m}{s^2}$ in the Lagrangian framework and in $\frac{kg}{m^2\,s^2}$ in the Eulerian framework.

3.3.3 Interpolation from particle cell to particle element

When a variable is interpolated from the fluid cell to the particle cell, the next step is to interpolate a variable to the individual particles. To interpolate a property to a given point in a Cartesian space, usually some form of trilinear interpolation is employed. In trilinear interpolation, the properties of the eight corners of an interpolation box are weighted onto the control point to obtain the interpolated value. The interpolation of a variable ϕ to the particle location, (x_c, y_c, z_c) from its corners is given by:

$$\begin{aligned}
\alpha &= \frac{x_{i+1} - x_c}{x_{i+1} - x_i} \\
\beta &= \frac{y_{j+1} - y_c}{y_{j+1} - y_j} \\
\gamma &= \frac{z_{k+1} - z_c}{z_{k+1} - z_k} \\
\phi_{\vec{r}_c} &= \alpha\beta\gamma\phi_{i,j,k} + (1-\alpha)\beta\gamma\phi_{i+1,j,k} + \alpha(1-\beta)\gamma\phi_{i,j+1,k} \\
&\quad + \alpha\beta(1-\gamma)\phi_{i,j,k+1} + (1-\alpha)(1-\beta)\gamma\phi_{i+1,j+1,k} + (1-\alpha)\beta(1-\gamma)\phi_{i+1,j,k+1} \\
&\quad + \alpha(1-\beta)(1-\gamma)\phi_{i,j+1,k+1} + (1-\alpha)(1-\beta)(1-\gamma)\phi_{i+1,j+1,k+1} \qquad (3.21)
\end{aligned}$$

This is illustrated in Figure 3.4.

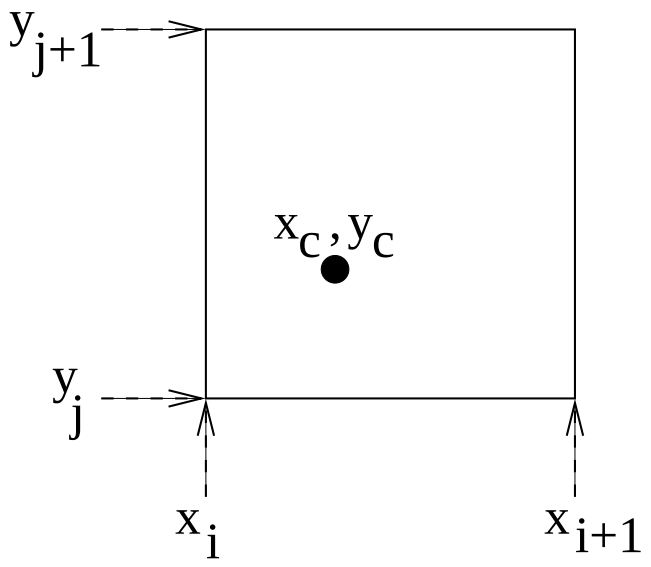

FIGURE 3.4: A two-dimensional Cartesian particle cell with corners $x_{i+\{0,1\}}, y_{j+\{0,1\}}$ and a particle located at x_c, y_c. [133]

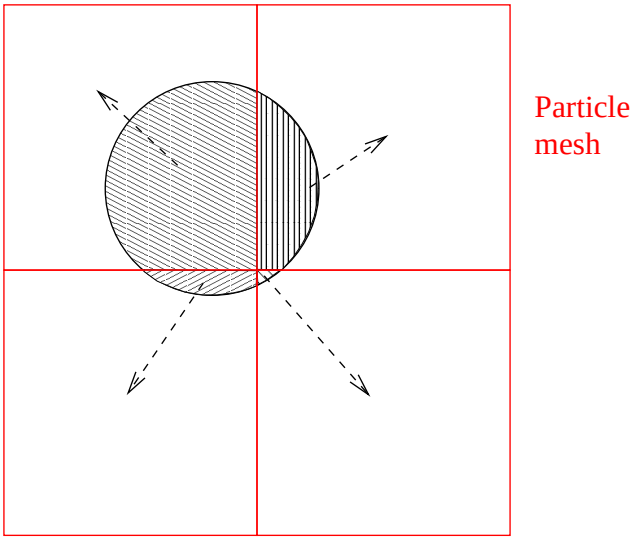

FIGURE 3.5: A particle may have contributions to a number of particle mesh cells. [133]

3.3.4 Interpolation from particle element to particle cell

When a variable is interpolated from a single particle to the particle mesh, it should be taken into consideration that a particle does not neccesarily lie solely within one particle mesh cell. More general, it will have contributions to multiple particle mesh cells, see Figure 3.5. When a variable is interpolated from an individual particle to the particle mesh, it is weighted by the volume of the particle lying

within each particle mesh cell. Hence,

$$\phi_{PC}(j) = \frac{\sum_{i=1}^{Nparticles} V_{P,i}(j)\phi_{P,i}}{\sum_{i=1}^{Nparticles} V_{P,i}(j)}, is \tag{3.22}$$

where $\phi_{PC}(j)$ represents the value of ϕ in the particle mesh cell j, $V_{P,i}(j)$ represents the volume of the particle i lying in particle mesh cell j (see the filled areas in Figure 3.5) and $\phi_{P,i}$ represents the value of ϕ at particle i.

Chapter 4

Drying of Large Particles

This chapter begins with a mathematical description of solving the main variables new to MultiFlow in both the gas and the particle phase. It further compares results from a 1D resolved particle model to an analytical solution for a 1D temperature profile to prove its correct implementation in the code. It is further shown that a particle model which has been extended with a water concentration profile for both bound and liquid free water is able to reproduce results similar to literature data. Advantages and drawbacks are discussed how this state-of-the-art (wood) drying model is suitable for modelling the drying process of numerous large particles. A study is presented which deals with the drying process of one batch of coffee beans - a typical example for drying Geldart D particles in fluidised beds. The CFD-DEM method has been extended, tested and validated by studying the drying process from a flow-scale to a sub-particle-scale level. Herein, heat, mass and momentum transport are solved on a fluid cell level; heat, mass and momentum transfer coefficients are solved at a particle scale level; and 1D temperature and moisture content profiles are solved inside each coffee bean on a sub-particle scale level. Therefore, this multiscale approach provides much more information compared to existing coffee bean roaster models.

4.1 Energy and Species Transport in the Gas Phase

The energy transport equation for the fluid phase is written as:

$$\frac{\partial(\epsilon\rho_f c_{p,f} T_f)}{\partial t} + \nabla\cdot(\epsilon\rho_f \vec{u}_f c_{p,f} T_f) = \nabla\cdot(\epsilon\lambda_f \nabla T_f) + \dot{Q}_f, \tag{4.1}$$

where $\dot{Q}_f$ is the heat exchanged between the fluid and the particle phase per time in one fluid mesh cell. Furthermore, T_f is the fluid temperature, λ_f and $c_{p,f}$ are the thermal conductivity and heat capacity of the fluid, respectively. The general species transport equation is given by eq. (4.2) and is used in the scope of this chapter to compute water vapour fractions $Y_{H_2O,f}$ in the gas phase. There is no further distinction of air, which is modelled as the second specie in the gas phase.

$$\frac{\partial(\epsilon\rho_f Y_{i,f})}{\partial t} + \nabla\cdot(\epsilon\rho_f \vec{u}_f Y_{i,f}) = \nabla\cdot(\epsilon\rho_f \Gamma_f \nabla Y_{i,f}) + S_i \tag{4.2}$$

The source term S_i is exchanged between the fluid and particle phase in one fluid cell per time. The diffusion coefficient Γ_f is defined as a function of the Schmidt number Sc (assumed to be 0.7 [147] for all species in this thesis) and the dynamic viscosity of the fluid μ_f as:

$$\Gamma_f = \frac{\mu_f}{Sc\rho_f}. \tag{4.3}$$

This simplification is justified, when it is assumed that properties such as temperature or species concentrations inside the particle are hardly affected by using the same diffusion coefficients of different gas species. In all simulations throughout this work, $c_{p,f}$, λ_f and μ_f are constant values specified in each section of this thesis. The fluid density ρ_f is set constant for single particle simulations while in fluidised bed simulations this value is modelled according to the equation of state. In this chapter, convection is the only heat transfer mechanism modelled so that the energy source term is expressed as:

$$\dot{Q}_f = \sum_{i=1}^{n} \left(\widetilde{h_i A_i} (\widetilde{T_i} - T_\infty) \right). \tag{4.4}$$

where the tildes indicate particle values as seen by the fluid (interpolated to the fluid mesh) and h is the convective heat transfer coefficient, which together with the vapour source term S_i is discussed in each relevant subsection individually as different models apply.

4.2 Particle Heat Transfer Implementation and Validation

The Biot number (Bi) is the ratio of the thermal conduction resistance R_{cond} inside the solid relative to the convection resistance R_{conv} at the surface outside the solid. When Bi $\rightarrow 0$ the gradient of the dimensionless temperature inside the particle can be neglected $\partial\theta/\partial\xi \rightarrow 0$ and for Bi $\rightarrow \infty$ the particle surface temperature will be similar to the fluid temperature

$$Bi = \frac{hl_0}{\lambda} = \frac{R_{cond}}{R_{conv}}, \tag{4.5}$$

where l_0 is the characteristic length defined here as the particle's volume to its surface ($r/3$ for a sphere), λ is the thermal conductivity of the particle and h is the heat transfer coefficient. A particle is considered to be thermally thin when $Bi < 0.1$, then the temperature within the sphere can be well approximated by the lumped capacitance method, assuming a uniform particle temperature. For $Bi > 0.1$, particles need to be numerically discretised (resolved) to obtain a correct temperature profile which refers to a thermally thick particle. The thermal wave regime is not discussed in this thesis. In the thermally thick regime, when a temperature profile is established inside the sphere, the thermal degradation (loss of water and volatiles) also progresses differently along the radius. Within this report, a resolved particle means the particle is numerically discretised into a number of sublayers to account for the temperature profile while an unresolved particle is not and can only have one temperature (does not differ along the radius). Eq. (4.6) has been implemented in MultiFlow to compute the temperature change of unresolved particles which are derived from an energy balance between stored energy by the particle and transferred energy to the surrounding.

$$\Delta T_p = \frac{\pi d_p \lambda_f Nu \Delta t}{mc}(T_p - T_f) = \frac{Ah\Delta t}{mc}(T_p - T_f) \tag{4.6}$$

Herein, A is the particle surface, c is the heat capacity and Δt is the fluid time step. Note, that eq. (4.6) is valid for zero-dimensional unresolved particles only as discussed in Section 5.2. To update the particle temperature more often than the fluid temperature would result in temperature "jumps" each fluid time step. Thus, the particle position is updated every particle time step while the particle temperature and species concentrations are updated each fluid time step. The accuracy of the particle temperature depends on particle and fluid properties.

Particle properties (m, c, A) are dependent on the mass (see Figure 5.12) and do change over one second real time. Fluid properties (T_f) do not change much quantitatively due to good mixing and consequently almost homogeneous thermal sand particle and fluid properties in fluidised beds. The accuracy of the particle temperature is not sensitive to the fluid time step chosen, which has been specified as $5 \cdot 10^{-5}$ seconds for studies described in Section 5.2.

Assuming that a larger thermally thick particle is exposed to symmetrical heating (constant h) with a uniform initial temperature, the particle temperature as a function of time and radial coordinate can be calculated as [148]

$$\theta(t,\xi) = \frac{T(t,\xi) - T_f}{T(0,\xi) - T_f} = \sum_{n=1}^{\infty} C_n \exp(-\mu_n^2 Fo) \frac{1}{\mu_n \xi} \sin(\mu_n \xi), \tag{4.7}$$

where $\xi = r/r_0$ and $Fo = \alpha t / r_0^2$. The Fourier number (Fo) is a dimensionless time and α is the thermal diffusivity - a measure for the ability of the material to conduct thermal energy relative to its ability to store the energy. The C_n coefficients are calculated as

$$C_n = \frac{4\left[\sin(\mu_n) - \mu_n \cos(\mu_n)\right]}{2\mu_n - \sin(2\mu_n)} \tag{4.8}$$

and the discrete eigenvalues μ_n are positive roots of the transcendental equation $Bi = 1 - \mu_n \cot(\mu_n)$. This method inherently includes boundary conditions, as the Bi number is defined by a characteristic length and the convective heat transfer coefficient.

This procedure gives theoretical solutions for the temperature but suffers from the fact that it cannot cope with source terms and changing boundary conditions. Therefore, the energy equation is discretised for the implementation in MultiFlow. Considering conduction inside the sphere as the only energy transport mechanism, the energy equation reads:

$$\frac{\partial(\rho c T)}{\partial t} \approx \overline{\rho c} \frac{\partial T}{\partial t} = \frac{1}{r^2} \frac{\partial}{\partial r} \left(\lambda r^2 \frac{\partial T}{\partial r} \right) + \dot{\omega}, \tag{4.9}$$

with

$$\overline{\rho c} = \left(\sum_i Y_i c_i \right) \rho_{total}. \tag{4.10}$$

As there is only a little change in ρc noticed each fluid time step during drying, this value has been updated according to eq. (4.10) each fluid time step and then kept constant $(\overline{\rho c})$ during iteratively solving eq. (4.9). Note, that Q_f is the source

term exchanged between fluid and particle while $\dot{\omega}$ is a source term applied at each sublayer inside the particle (e.g. when a phase transition of water inside the particle is encountered). The overall density of the material is determined by

$$\rho_{total} = \frac{1}{\sum \frac{Y_{H_2O}}{\rho_{H_2O}} + \sum \frac{Y_{DS}}{\rho_{DS}}}. \tag{4.11}$$

The subscript DS refers to the dry solid material. Boundary conditions for the particle centre and particle surface are given as follows:

$$\left.\frac{\partial T_p}{\partial r}\right|_{r=0} = 0 \qquad -\lambda_p \left.\frac{\partial T_p}{\partial r}\right|_{r=R} = h(T_p - T_f) \tag{4.12}$$

For the sake of simplicity, only convective heat transfer between the fluid and the particle is considered. For model comparisons in Sections 4.2 and 5.1, the convective heat transfer coefficient $h = Nu\lambda_f/d_p$ is derived from the Ranz-Marshall [149] correlation, valid for a single particle in a plug flow according to:

$$Nu = \frac{hd_p}{\lambda_f} = 2.0 + 0.6Re_p^{1/2}Pr^{1/3}, \tag{4.13}$$

and other boundary conditions are given in Table 4.1 or explained in Section 3.1. Eq. (4.9) is discretised as explained in Appendix A and solved with a fluid time step of 10^{-2} seconds, low enough to achieve good agreement with an analytical solution. The non-moving 500μm particle has been resolved with 40 sublayers. The results of both eqs. (4.7) and (4.9) are compared in Figure 4.1, where source terms are neglected for the time being to give proof of a reasonable implementation of eq. (4.9).

For a fluid temperature of 800K, the convective heat transfer coefficient for single particles rises to $h = 235W/m^2K$, while $Bi = 0.39$ and hence the temperature gradient inside the particle cannot be neglected (thermally thick). In Figure 4.1 the dimensionless particle temperature θ for the particle centre ($\xi = 0$) and for the particle surface ($\xi = 1$) is plotted over the dimensionless time where the data are computed from eqs. (4.7) and (4.9) respectively. Results are in excellent agreement indicating that eq. (4.9) is correctly discretised and implemented into MultiFlow.

By using the same boundary conditions as given in Table 4.1 but changing the particle diameter one obtains Figure 4.2. Herein, the heating times required from

TABLE 4.1: Material and setting parameters used in Section 4.2

Variables	Values
u_f	1 m/s
T_f	800 K
$T_{p,0}$	300 K
d_p	0.0005 m
λ_p	0.15 W/mK
c	1670 J/kgK
ρ_p	700 kg/m^3
ρ_f at $800K$	0.44 kg/m^3
λ_f at $800K$	0.05516 W/mK
$c_{p,f}$ at $800K$	1.1243 J/kgK
μ_f at $800K$	3.6e^{-5} m^2/s

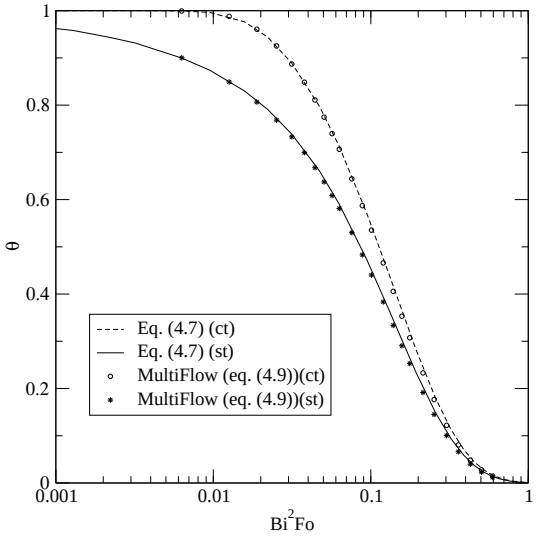

FIGURE 4.1: Dimensionless particle temperature during convective heating as a function of time

ambient to common fast pyrolysis temperatures for single biomass particles exposed to convective heat transfer is given. Under fast pyrolysis conditions discussed in Chapter 5, the convective heat transfer coefficient h is much higher (see Figure 5.16). Nevertheless, it indicates how much more real time for the drying process of larger particles is required. Depending on the remaining complexity of the (DEM) simulation, it shows that its feasibility is quickly restricted when larger particles are of interest.

The biomass particle diameter should be less than 2mm for bubbling fluidised beds pyrolysers, less than 6mm in circulating fluidised beds and around 20mm in ablative pyrolysis reactors [18]. As only bubbling fluidised beds are discussed

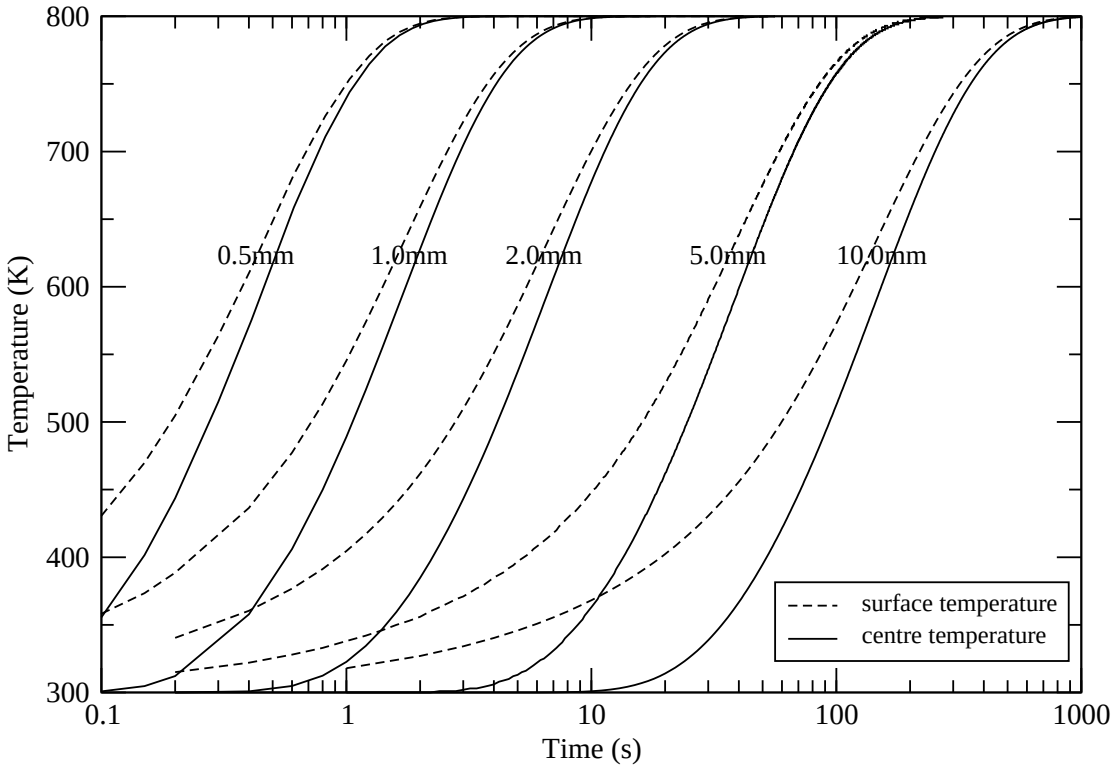

FIGURE 4.2: Wood particle temperature as a function of time and diameter for $T_f = 800K$

throughout this thesis, 2mm is thought of as the upper limit targeted in future simulations.

4.3 Drying of Single Large Particles

This section deals with the drying process of biomass particles with moisture contents more than 30%. This requires to distinguish between liquid and bound water which do migrate through the particle differently.

4.3.1 Theory and Model Description

Fresh harvested solid biomass feedstock contains typically about 40-100% water based on dry wood [150]. This water can be found mainly as bound (absorbed) water in the solid, water vapour in the pores, free (liquid) water in the pores and free water at the particle surface. The removal of all different forms of water inside a wood particle is considered as drying. Chemically (hydrate water) and physically (Van der Waals) absorbed water has the strongest bonding, their transport is

driven by concentration gradients (diffusion) and their removal requires the greatest amount of energy. Free water and vapour in the pores is mainly transported by pressure gradients generated by the local evaporation of liquid water (convection). Free water at the particle surface can only be found at very high moisture contents - which is not considered throughout the present study.

In the literature, many drying models have been proposed, based on different model assumptions. Models with heat transport limitation, diffusion limitation, equilibrium approaches, kinetic approaches and empirical models are compared by Raupenstrauch [151], where especially the range of validity and the model validation with experimental results are discussed. Drying under fast external heat transfer rates and/or high temperatures has been modeled with a high degree of complexity by several authors [57, 58, 152, 153]. The following model description is based on their work without modelling the gas phase inside the particle.

A particle-drying model in 1D has been implemented and tested in MultiFlow. Herein, the particle is treated as a two-phase mixture between solid dry virgin wood and liquid free and bound water. The vapour is considered to be released directly at the particle surface into the surrounding gas. Although free liquid water is transported by convection as pointed out earlier, the model assumes a diffusive transport to avoid modelling pressure inside the particle. During drying, the solid virgin wood density remains constant as no pyrolytic degradation is considered. This section further follows the conditions as used by Di Blasi [153] where no particle shrinkage and evaporation below 373K is considered. All spherical biomass particles are modelled as isotropic, although very high property differences in longitudinal, radial and tangential direction for wood are encountered [152]. The set of transport equations are given for
(1) liquid free water as

$$\frac{\partial(\rho_l^*)}{\partial t} = \frac{1}{r^2}\frac{\partial}{\partial r}\left(D_l r^2 \frac{\partial \rho_l^*}{\partial r}\right) + \dot{\omega}_l, \tag{4.14}$$

and (2) bound water as

$$\frac{\partial(\rho_b^*)}{\partial t} = \frac{1}{r^2}\frac{\partial}{\partial r}\left(D_b r^2 \frac{\partial \rho_b^*}{\partial r}\right) + \dot{\omega}_b. \tag{4.15}$$

All densities marked with an asterisk are phase averaged, partial or apparent densities. Densities without an asterisk are intrinsic properties with constant values (e.g. $\rho_l = \rho_b = \rho_{H_2O} = 1000 kg/m^3$). When the phase averaged water

densities ρ_l^* and ρ_b^* are solved, the moisture content can be determined as follows:

$$X_{H_2O} = \frac{\rho^*_{H_2O}}{\rho_{DS}} = \frac{\rho_l^* + \rho_b^*}{\rho_{DS}} = \frac{Y_{H_2O}}{1 - Y_{H_2O}} \tag{4.16}$$

$$X_b = MIN(X_{FSP}, X_{H_2O}) = MIN(0.3, X_{H_2O}) \tag{4.17}$$

$$X_l = X_{H_2O} - X_b \tag{4.18}$$

$$\rho_b^* = \rho^*_{H_2O}\frac{X_b}{X_b + X_l} \qquad \rho_l^* = \rho^*_{H_2O}\frac{X_l}{X_b + X_l} \tag{4.19}$$

X_{FSP} is the moisture content based on solid dry wood at the fibre saturation point. This fibre saturation point denotes the point in the drying process at which only water bound in the cell walls remain, all liquid free water from the cell cavities are removed. This value is assumed to be temperature independent and to be 0.3 for wood [152]. Absorbed water is attached or encapsulated by cellulosic material and needs to be removed with extra energy to break these bonds. Therefore, free water leaves the particle earlier than bound water. When all free water is removed, the remaining water is saturated in fibres. To overcome the extra energy required to turn bound water into vapour, the evaporation enthalpy is considered to be higher [154]. The same is true for the transport of liquid free and bound water [155] and consequently different diffusion coefficients are applied.

$$\Delta h_l = 2260\frac{kJ}{kg}; \qquad \Delta h_b = (3348 - 13085X_{H2O} + 60262X^2_{H2O} - 95778X^3_{H2O})\frac{kJ}{kg} \tag{4.20}$$

$$D_l = 5.0e^{-9}\frac{m^2}{s}; \qquad D_b = (exp(-9.9 - 4300/T + 9.8X_b))\frac{m^2}{s} \tag{4.21}$$

Following a mixing rule, the particle effective thermal conductivity λ_p is expressed as a function of the gas volume fraction ϵ and the volume fraction occupied by the water [153]:

$$\lambda_p = \lambda_{DS} + \epsilon_g\lambda_g + (\epsilon_l + \epsilon_b)\lambda_{H_2O}, \tag{4.22}$$

where

$$\epsilon_g = \epsilon_{g,0} - \epsilon_l \quad \text{with} \quad \epsilon_l = \rho_l^*/\rho_l \tag{4.23}$$

and

$$\epsilon_l + \epsilon_b = \epsilon_{H_2O} = X_{H_2O}\frac{\rho_{DS}}{\rho_{H_2O}}. \tag{4.24}$$

In this drying model, $\epsilon_{DS} + \epsilon_b + \epsilon_l + \epsilon_g = 1$. However, the volume fraction of bound water and of the dry solid (virgin wood) material are not further needed by the

code. The heat capacity at each node point along the particle radius is defined as:

$$c = c_{H_2O} Y_{H_2O} + c_{DS}(1 - Y_{H_2O}). \tag{4.25}$$

The source terms are given as

$$\dot{\omega}_{max} = MAX\left(0, \frac{(T - T_{evap})\rho_p c}{\Delta t}\right), \tag{4.26}$$

$$\dot{\omega}_l = MIN\left(\frac{\rho_l^*}{\Delta t}, \frac{\dot{\omega}_{max}}{\Delta h_l}\right), \tag{4.27}$$

$$\dot{\omega}_b = MIN\left(\frac{\rho_b^*}{\Delta t}, \frac{\dot{\omega}_{max} - \dot{\omega}_l \Delta h_l}{\Delta h_b}\right), \tag{4.28}$$

$$\dot{\omega} = MIN\left(\dot{\omega}_{max}, \frac{\rho_l^*}{\Delta t}\Delta h_l + \frac{\rho_b^*}{\Delta t}\Delta h_b\right), \tag{4.29}$$

where the first term in the MIN statement ensures that not more mass is transferred than is remaining and the second term is the actual mass considered in all other cases. Initial and boundary conditions are given in Table 4.2, where a constant heat transfer coefficient is assumed. Most fluid phase properties (c_p, μ_f, ρ_f, species concentration,...) are not used in this model. The discretisation for a general partial differential equation in 1D is given in Appendix A. A fluid time step of 10^{-2} seconds has been used. The 1D temperature and species profile have been resolved into 40 sublayers for all particle sizes studied - more than required as $Bi \approx 0.39$ indicates only a slightly developed temperature gradient profile. When water transport equations are solved (as in eqs. (4.14), (4.15) or (4.34)), the solution procedure can be described as follows. The energy equation (4.9) is solved first by using moisture concentration from the previous time step, followed by the water transport equation (e.g. (4.34)) by using new temperature values. Both equations are solved in each fluid time step and coupled by an iterative process.

4.3.2 Results and Discussion

A single wood particle of 0.01m in diameter, an initial temperature of 300K and a moisture content of 50% is exposed to high temperature at 600K. Further model parameters have been summarised in Table 4.2, except where stated otherwise. Figure 4.3a shows model results for the spatial temperature distribution inside the particle as a function of time. Temperature rise is almost uniform throughout the particle (high heat conduction) below the water boiling temperature of 373K

TABLE 4.2: Drying model parameters used in Section 4.3 according to Di Blasi [153]

Variables	Values	Variables	Values	Variables	Values
d_p	0.01 m	c_{DS}	1670 J/kgK	h	20 W/m^{2}K
ρ_{DS}	600 kg/m^3	c_{H_2O}	4200 J/kgK	λ_g	0.03 W/mK
T_f	600 K	D_b	0.0 m^2/s	λ_{DS}	0.14 W/mK
$T_{SD,0}$	300 K	$\epsilon_{g,0}$	0.6	λ_{H_2O}	0.61 W/mK

and remains there until the water is completely removed locally. A decrease in the local mass concentration of water vapour causes the water to evaporate at lower temperatures and vice versa leading to the fact that the temperature profile is much smoother than predicted by the model described above. After complete water evaporation, the temperature gradient becomes steeper (heat conduction is lower without water) and the process is controlled by internal heat transfer.

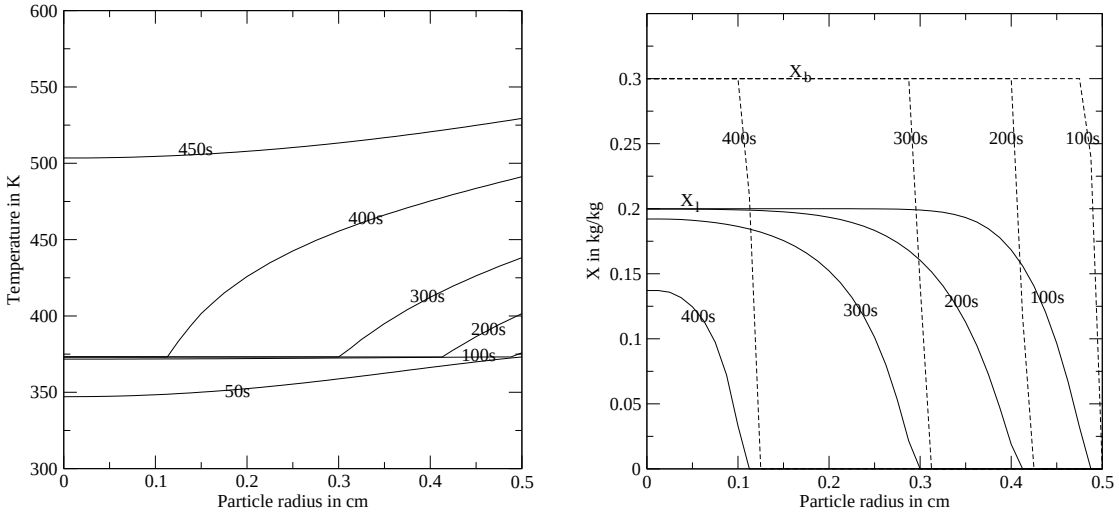

FIGURE 4.3: Spatial profiles of a) temperature and b) bound and free liquid water for different times inside a 1cm spherical wood particle with an initial moisture content of $X_0 = 0.5 kg_{H_2O}/kg_{DS}$.

Two different distinct drying fronts for bound and free liquid water propagate through the particle in time (Figure 4.3b). Bound water does not move much through the particle so that the drying front is steep. Capillary free liquid water migrates faster and establishes a smooth water concentration gradient between the drying front and the inside of the particle. Water evaporation simplified as boiling process around 100^{o}C takes place along a narrow region (layer) inside the sphere (Figure 4.4). This layer is characterised by a steep gradient towards the particle surface side (actual drying front) while a smoother side towards the particle centre side is influenced by the capillary free liquid water transported

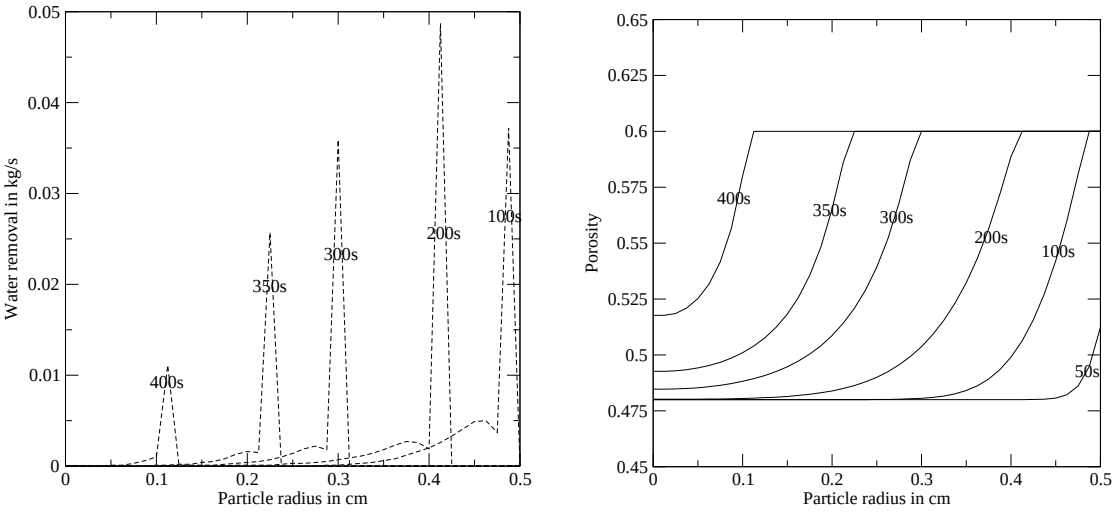

FIGURE 4.4: Spatial profiles of a) water removal rates and b) porosity for different times inside a 1cm spherical wood particle with an initial moisture content of $X_0 = 0.5 kg_{H_2O}/kg_{DS}$.

towards the front. A small minimum of water removal left to the big spikes can be observed in Figure 4.4a. This can be referred to as the diffusive transport (based on concentration gradients) of the free liquid water near the drying front where the gradient reduces (see Figure 4.3b). The amount of water reduced per time is higher towards the high temperature surface. The removal of capillary water gives room for gas cavities and increases the particle porosity (Figure 4.4b). In general, the higher the diffusion rates the shorter the drying period.

Boundary conditions have been selected to be comparable to outcomes of a similar drying model proposed by Di Blasi [153]. The present model is simplified in the way that it releases the vapour straight after the phase change has occurred. In reality and in the model discussed by Di Blasi vapour rises the gas pressure inside the particle and is transported by convection and diffusion to the particle surface. Pores are small enough to avoid an instantaneous vapour release at the surface. Due to the pressure rise, the boiling temperature of water rises above 373K and the duration of the drying process increases.

Under the same boundary conditions as given in Table 4.2, the drying process has been modelled for different external heat transfer coefficients, from 5 to 30 W/m^2K, as presented in Figure 4.5b. The overall drying process is strongly dependent on h and with increasing h the controlling mechanism shifts from external to internal heat transfer. All results are in excellent agreement with predictions modelled by Di Blasi [153].

In eq. (4.17) the maximum bound water content based on dry wood has been assumed to be 0.3. In practice, this value refers to ambient conditions, where $X_{FSP,0} = 0.3$ and X_{FSP} is temperature dependent and reduces according to [155]

$$X_{FSP} = X_{FSP,0} + 0.298 - 0.001T. \tag{4.30}$$

When the particle temperature rises, a portion of bound water turns into free liquid water, as the connectivity to cell walls gets weakened. Using eq. (4.30) means that more free water is considered resulting in lower latent heat, faster water transport and shorter drying times. Figure 4.5b shows results under consideration of eq. (4.30) where the level of liquid water is much higher (compare Figure 4.3b). After 400s water is completely removed indicating a faster drying progression. The consideration of a temperature dependent X_{FSP} leads to very different and more accurate results than the most often assumed constant value. This is not considered in the work of Di Blasi [153] and can be seen as an improvement to her work. From eq. (4.30) it becomes evident, that the bound water content around 100^oC is always above 10%. This water content is usually assumed for the virgin biomass material to be used in fast pyrolysis applications. In other words, liquid free water transport in particles can be neglected in most cases. Therefore, when modelling numerous particles, one partial differential equation can be avoided to be solved per fluid time-step and per particle saving a lot computational power. The gas porosity ϵ_g changes in time only because liquid water fills the initial pore. The stability of the porous material is hence rather dependent on $\epsilon_{g,0}$ which is constant and therefore not interesting to incorporate into the fragmentation model described in Chapter 6.

4.4 Drying of Multiple Large Particles

In this section, many large particles inside a fluidised bed dryer are modelled. The drying process is discussed from the sub-particle scale to the fluid scale level. Larger woody biomass particles (small wood chips or large sawdust) differ often significantly from the spherical shape and they are usually dried in other processes than fluidised beds. Therefore, a small fluidised bed coffee-bean roaster is chosen to test and validate the present model. Based on the given literature review (Chapter 2), coffee bean roasting has been found to be suitable to test and validate the present drying model.

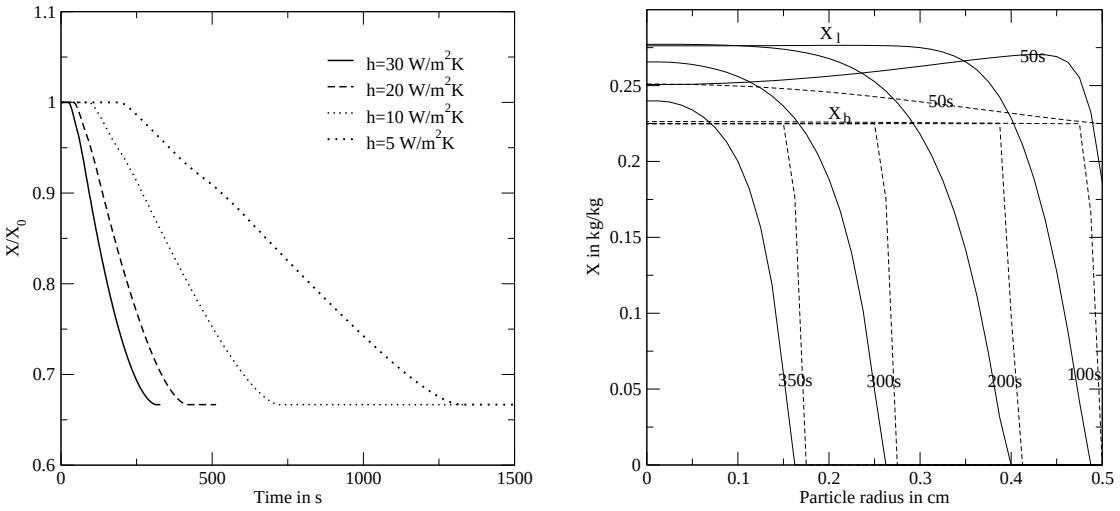

FIGURE 4.5: a) Normalised particle mass for different heat transfer coefficients as a function of time b) spatial profiles of bound and free liquid water under temperature dependent FSP

4.4.1 Model Description

The drying process in fluidised beds is characterised by lower fluidisation temperatures ($< 250^o$C) and drying of particles is supported by other means for example by good mixing and high heat transfer coefficients. When drying is treated numerically as a boiling process around 100^oC less information can be obtained compared to other theoretical approaches. Therefore, this section treats drying as a process where the source term is based on the vapour concentration at the particle surface and local gas environment. Furthermore, the moisture content of coffee-beans is below 10% in this study, so that water is treated as bound water only. It is assumed that inside a spherical particle, conduction is the only energy transport mechanism and reaction enthalpy, heat transport by water diffusion and condensation of water vapour are neglected. In that case the energy transport equation is solved inside each particle as given in eq. (4.9), although different boundary conditions at the particle surface apply due to the different drying approach used.

$$\left.\frac{\partial T_p}{\partial r}\right|_{r=0} = 0 \qquad -\lambda_p \left.\frac{\partial T_p}{\partial r}\right|_{r=R} = h(T_p - T_f) + k(c_s - c_f)\Delta H_{evap} \tag{4.31}$$

Here, h is the convective heat transfer coefficient and k the mass transfer coefficient. Both are derived from the Colburn (or Colburn-Chilton) analogy, where the Colburn "j-factor" has been obtained from the Gupta and Thodo's correlation [156] for fixed and fluidised beds. The convective heat and mass transfer

coefficients are then expressed as:

$$h = 2.06 Re_p^{-0.575} \frac{|\widetilde{\vec{u}_f} - \vec{u}_p|}{\epsilon} c_{p,f} \rho_f \left(\frac{\lambda_f}{c_{p,f} \mu_f} \right)^{2/3}, \tag{4.32}$$

$$k = 2.06 Re_p^{-0.575} \frac{|\widetilde{\vec{u}_f} - \vec{u}_p|}{\epsilon} \left(\frac{\rho_f D}{\mu_f} \right)^{2/3}, \tag{4.33}$$

where Re_p is the particle Reynolds number defined in Table 3.1. Evaporation takes place only at the surface of the particle and the source term $\dot{\omega}$ in eq. (4.9) is zero. Liquid water transport within the coffee bean is modelled via diffusion and the conservation equation for water without considering water generation due to condensation is given by

$$\frac{\partial Y_{H_2O}(r,t)}{\partial t} = D \left[\frac{\partial^2 Y_{H_2O}}{\partial r^2} + \frac{2}{r} \frac{\partial Y_{H_2O}}{\partial r} \right]. \tag{4.34}$$

The effective diffusion coefficient D is set to a constant value and has not been modified for all simulations. The boundary conditions at the particle centre ($r = 0$) and at the particle surface ($r = R$) are given as:

$$\left. \frac{\partial Y_{H_2O}}{\partial r} \right|_{r=0} = 0 \qquad - D \rho_p \left. \frac{\partial Y_{H_2O}}{\partial r} \right|_{r=R} = k(c_s - c_f), \tag{4.35}$$

where c_f is the vapour concentration in the fluid phase and c_s is the vapour concentration at the bean surface. The vapour concentration at the surface can be described as a function of material, temperature and water concentration according to:

$$c_s = a_w \left(Y_{H_2O,s}, T_{p,s} \right) c_{sat,s}, \tag{4.36}$$

where $c_{sat,s}$ is the vapour saturation concentration at the particle surface and a_w is the water activity obtained from Iglesias and Chirife [157]. The water activity is defined by the vapour pressure of the water in the material to the vapour pressure of pure water. Many materials contain salts and sugars so that the "escaping tendency" of the water is also influenced by dipole-dipole, ionic or hydrogen bonds. Batch fluid bed drying curves appear to be predictable on the basis of single particles [158]. The vapour pressure of saturated air at the particle surface $p_{sat,s}$ is given by the Antoine equation with constants taken from Gmehling and Kolbe [159].

$$p_{sat,s} = 10^3 \ 10^{\left(7.19621 - \frac{1730.63}{233.426 + (T_{p,s} - 273.15)}\right)} \tag{4.37}$$

The vapour saturation concentration at the surface is then determined by

$$c_{sat,s} = MIN\left(\frac{p_{sat,s}W}{R_u T_{p,s}}, Y_{H_2O,s}\rho_{p,s}\right), \tag{4.38}$$

where W is the molar mass of water. The thermal conductivity λ_p inside the wet coffee bean has been assumed to be constant for low moisture contents [75] and the thermal heat capacity c of the wet particle is a function of species concentration as stated in Table 4.3. Each particle's temperature and moisture content profiles have been resolved into 15 sublayers as the heat conduction resistance inside the particle is much higher than the heat convection resistance at the particle surface ($Bi >> 1$).

Single, non-moving particle heat and mass transfer studies with a different number of sublayers (10, 15, 40 sublayers) and with the same flow rate and temperature mentioned above have been conducted. All results can not be distinguished on a fluid-scale or particle-scale level. On a sub-particle-scale level, results with 15 sublayers correspond fairly well with 40 sublayers (being almost identical with many more) and show a fairly good improvement to 10 sublayers. The sub-particle heat transfer model is updated every fluid time step ($10^{-3}s$) when new fluid values (T_f and $Y_{H_2O,f}$) are available. It has been found that the heat transfer model is very stable under such time steps.

4.4.2 Results and Discussion

The CFD code MultiFlow and its DEM module have been used to model discrete, spherical, non-isothermal, non-homogeneous but isentropic coffee beans in a fluidised bed roaster. Boundary and initial conditions, geometric and experimental data have been taken from Heyd et al. [77]. The fluid density is solved according to $\rho_f = \frac{p}{R_u T_f}\sum_i W_i Y_{m,i}$ while other gas properties are set to constant values ($\mu_f = 2.77e^{-5}kg/ms, c_{p,f} = 1.03kJ/kgK, \lambda_f = 0.0417W/mK$). These data are assumed and set constant and valid for such temperatures. Other initial and boundary conditions are given in Table 4.3. For this batch process, 100g coffee beans with an initial moisture content of 0.082 kg_{H_2O}/kg_{DS} and a temperature of 20°C (both gas and coffee beans) are roasted for 10 minutes with a fluidising air temperature of 210 and 250 °C. Coffee is roasted within this temperature range [77]. A variety of global and local data are discussed to better understand and judge the roaster performance and to better control these processes.

TABLE 4.3: Setting parameters used in Section 4.4. Soft-sphere DEM parameters are the same for walls and particles.

Variables	Values
d_p	6.6 mm [79]
c	$(1.099 + 0.007T_b + 5.0X_{H_2O})/(1 + X_{H_2O})$ [76]
ρ_{DS}	800 kg/m^3 [75]
ρ_{H_2O}	1000 kg/m^3
λ_p	0.07 W/mK [75]
T_p (initial)	293 K [77]
X_{H_2O} (initial)	0.082 kg_{H_2O}/kg_{DS} [77]
$d_{Roaster}$	80 mm [77]
$\dot{m}_f$	0.02 kg/s [77]
ΔH_{evap}	2790 kJ/kg [76]
D	3 $10^{-9} m^2/s$
E	1 $10^{+8} N/m^2$
ν	0.3 $-$
e	0.9 $-$
μ	0.3 $-$

As expected and as it can be seen in Figure 4.6a, the gas temperature near dense particle regions reduces quickly due to negative heat source terms. A very early stage (2 seconds after the start) has been chosen to show a clear temperature difference which reduces in time. Figure 4.6a shows that the gas velocity is higher on the left hand side where the gas passes slightly less number of particles. Similar effects can be seen when the water vapour mass fraction is plotted (Figure 4.6b), where the water concentration in the gas phase significantly increases when the gas passes through the dense particle bed. Due to the coarse particles and in turn the required coarse fluid mesh, this setup does not account for turbulence. In case where turbulence would matter, this current setup would not be able to resolve the required flow field. Therefore, appropriate turbulence models may be needed, which might be part of future work.

In these simulations the fluid mesh has 33 cells in X-Y plane and 24 cells in Z-direction (height of the domain). The cylinder is 8cm in diameter and 24cm in height, which means the fluid cell size is roughly 1cm in each direction. The particle mesh is a uniform Cartesian mesh with 6.6mm in each direction.

Fluidised beds are known for their good mixing of the overall particle charge. Effective mixing is important to achieve a uniform product quality. During initialisation, each particle has been allocated with a different particle number, starting

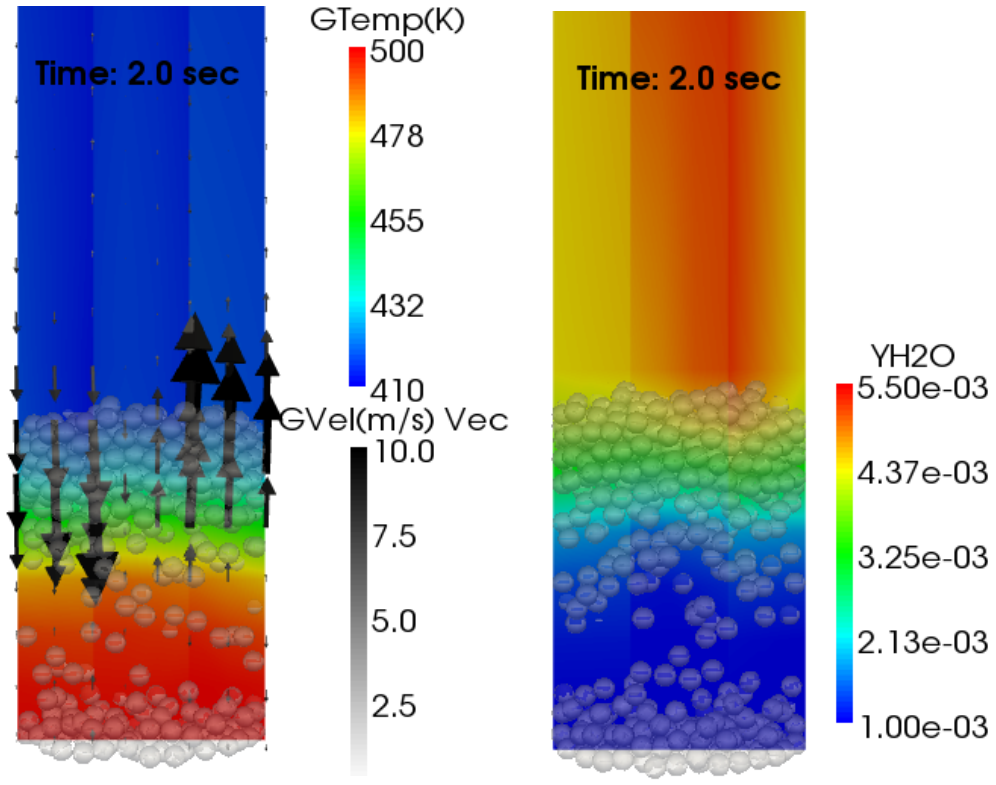

FIGURE 4.6: a) Gas temperature scalar values and gas velocity vectors and b) water vapour mass fractions after 2 seconds of roaster operation

with the bottom right and front particle (number 1) up to the final at the top, left and back of the domain (780 particles in total). Then, each particle can be identified and traced back in time. Figure 4.7a shows the disorder of particles at time t=7.44 seconds based on their given particle number during initialisation. One criterion to judge fluidised bed roasters is how quickly the particle charge is partially or completely mixed.

The bean temperature is of particular significance as it affects the drying process and pyrolytic reactions which determine the bean quality in the first place. Each product has an optimal water content (longest shelf life associated with it) and a specific degree of roasting is important to obtain the right aroma. Therefore, the time period in certain particle temperature windows is important. However, pyrolytic reactions and their reaction enthalpy have not been considered in this study, although the temperature of 250 °C is usually known as the upper temperature limit for coffee bean roasting where a certain activity for chemical reactions might be expected. Figure 4.7c presents the average temperature of individual

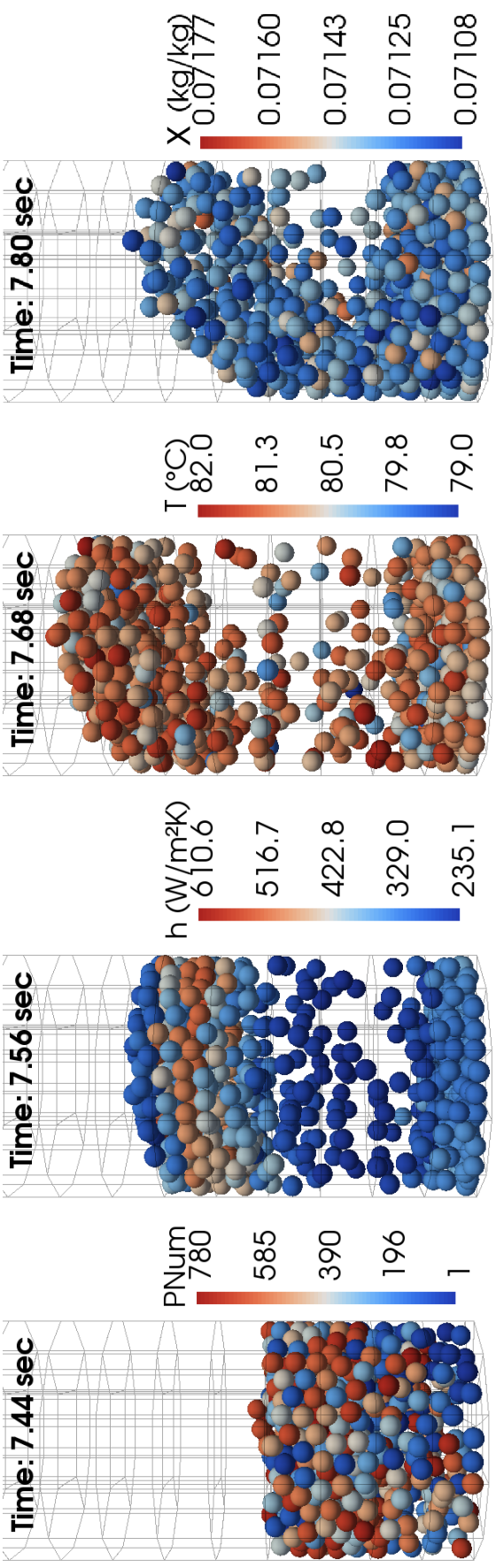

FIGURE 4.7: a) Particle numbers indicating disorder, b) convective heat transfer coefficient of individual particles and the fluid, c) average temperature of individual particles and d) average moisture content of individual particles

particles. The difference between the coldest and hottest particle is 3K at 7.68 seconds and reduces when the simulation progresses.

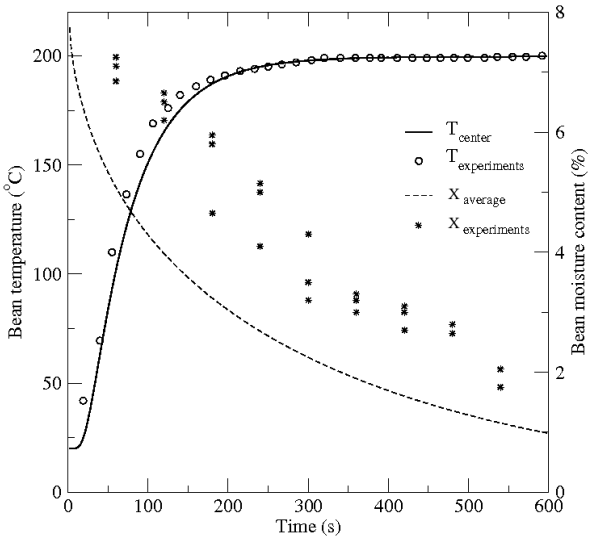

FIGURE 4.8: Simulated bean temperature and moisture content and experimental data at an air temperature of 210°C

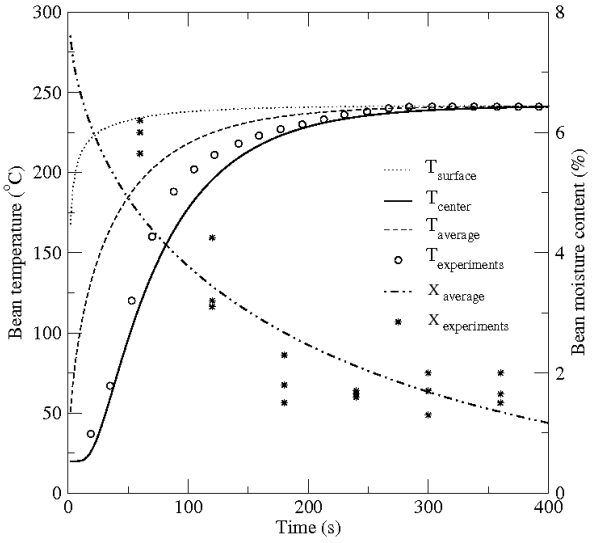

FIGURE 4.9: Simulated bean temperature and moisture content and experimental data at an air temperature of 250°C

The Colburn analogy is used to model convective heat transfer using eq. (4.32). All fluid parameters do not change significantly but the fluid volume fraction ϵ and the fluid flow velocity u do. Although a higher fluid velocity in dense particle regions is observed, the fluid volume fraction is low - causing the heat transfer

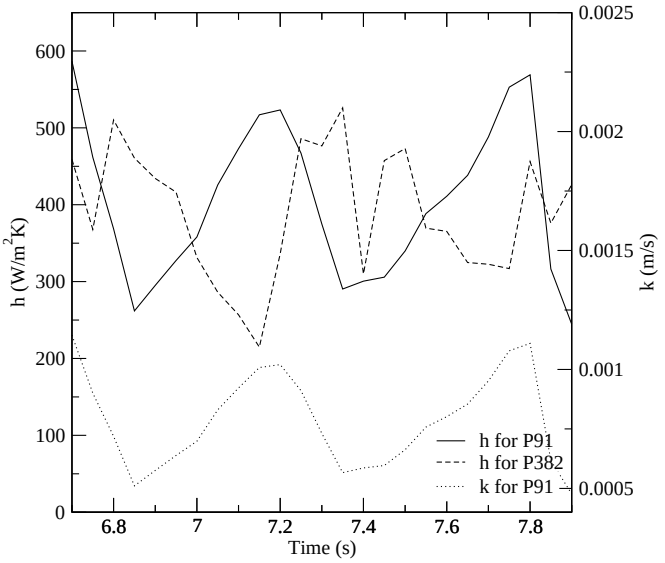

FIGURE 4.10: Heat and mass transfer coefficient of selected particles

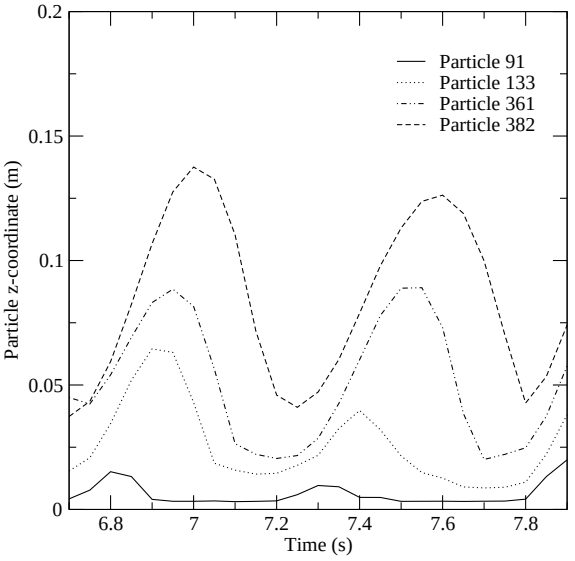

FIGURE 4.11: Z-coordinate of selected particles

coefficient to be high and vice versa. This phenomenon is well known as reported by Kunii and Levenspiel [1]. Figure 4.7b illustrates the convective heat transfer coefficient at a distinct time during the simulation.

Higher moisture contents go along with bacterial growth and lower expected shelf life. Monitoring and controlling the bean moisture content is essential during coffee bean processing. Figure 4.7d shows the average moisture content X of individual particles after 7.8 seconds of operation. Differences between particles are very little.

Figures 4.8 and 4.9 show experimental data and simulated average, surface and centre bean temperatures (averaged over all particles). Experimental data are bean centre temperatures of individual particles and measured according to the Association Francaise de Normalisation (AFNOR [160]). Experimental data and model results are in very good agreement for an inlet air temperature of 250 °C but differ in the moisture content for 210°C. In both cases, the effective water diffusivity has been kept constant so that very similar moisture content profiles appear. Nevertheless, the model predicts very good outcomes for the bean temperature as exothermic pyrolytic reactions [76] are not taken into account and the thermal conductivity and again the water diffusivity are constant values which do change in practice. One more difference between experiment and model lies in the particle shape (spherical assumpion for the model). Simulated centre, surface and average temperature values do indicate a distinct temperature profile ($Bi \approx 45$) in each bean which dwindle with progressing operation time. Minimum and maximum modelled centre temperatures (coldest and hottest particle) do not vary a lot.

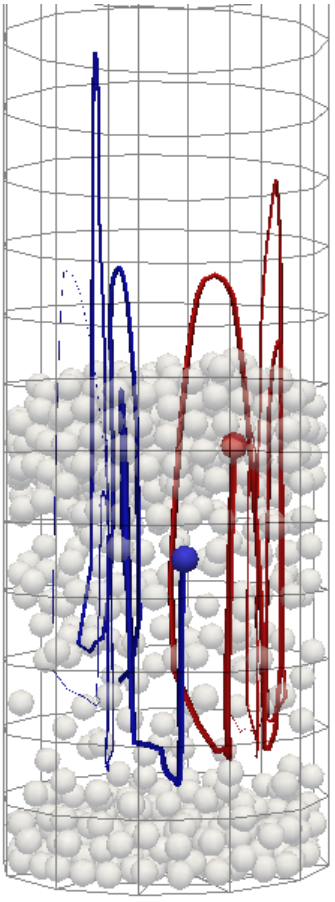

FIGURE 4.12: Hottest (red) and coldest (blue) particles including their trajectories

The overall fluidisation behaviour of these particles is reported by Heyd et al. [77] as spouting. As depicted in Figure 4.11, there is a periodic lifting of particles which goes along with a development of large gas bubbles which coalesce and grow and become large enough to spread across the vessel, known as slugging (Figure 4.7). These periodic particle lifts start at the bottom of the bed (particle 91), causing the upper particles to rise with a small delay in time. In this fluidised bed coffee roaster, the spouting motion ensures that high and low heat transfer coefficients are well balanced (Figure 4.10). Particles in different bed heights experience usually similar heat exchange rates although the minimum and maximum values are encountered at different times. Heat and mass transfer coefficients are related via the Colburn analogy and are directly proportional to each other (Figure 4.10).

DEM models compute particle collision forces to update the particle position. These collision forces and frictional forces on the coffee bean can be analysed for breakup studies. Next to the bean quality, it is desired to know how many coffee beans remain unbroken and how fragments affect the fluidisation. In addition, particle coordinates deliver a trajectory in time, which can be used to study the roaster performance (e.g. vortices, trapped particle location) and might explain extreme particle properties due to their spatial history. In this particular fluidised bed, very good mixing is achieved in a very short time, indicated by the 3K temperature difference between coldest and hottest particle (Figure 4.7c). Trajectories compared between hottest (red particle with red trajectory) and coldest (blue particle with blue trajectory) particle in Figure 4.12 can be used to study preferably continuous drying processes or more geometrically complicated reactors to find maladjustments or geometric problems.

4.5 Conclusions

In this chapter, the drying process of large particles is studied, using different drying models and assumptions. Based on the results from this chapter, it can be concluded that all 1D transport equations to determine the temperature and moisture content profile(s) along the particle radius are successfully implemented and tested in MultiFlow. Model validation has been carried out threefold:

1. A theoretical comparison is made between an analytical solution for 1D heat conduction through a spherical particle given by eq. (4.7) and results from

the implemented 1D energy equation given in eq. (4.9). Both results are in excellent agreement (Figure 4.1).

2. A drying model which distinguishes between free liquid and bound water for biomass moisture contents higher than 30% has been published by Di Blasi [153]. The same basic theoretical concept has been implemented and tested in MultiFlow and under very similar conditions very similar results have been obtained.

3. Experimental data have been compared to model results (Figure 4.8 and Figure 4.9) when applied to the process of coffee bean drying/roasting. The diffusion controlled drying model based on vapour concentration gradients between the particle surface and local gas environment is able to reproduce the essential moisture contents inside each coffee bean compared to measured data.

Figure 4.2 shows the required time for convective heating of larger wood particles. Even for higher convective heat transfer coefficients h in dense fluidised beds compared to single particles, it indicates that modelling the thermochemical degradation of larger wood particles in fluidised beds (using the DEM approach) cannot be achieved easily. Under provided conditions, a particle with a 10 times larger diameter requires a 100 times longer heating time. So far, no endothermic reactions as seen during fast pyrolysis have been considered, which can prolong the heating time even further.

Drying of single large particles is modelled by treating evaporation as a boiling process around 100^{o}C. This model distinguishes between capillary free liquid and bound water, accounts for a porosity change and delivers useful information on the drying front inside the particle. However, free liquid water transport inside the porous particle has not been modelled by convection. Doing so would increase the models applicability, accuracy and validity. However, particularly for predried wood, liquid free water is less important to consider. Modelling free liquid water would require one differential equation more for each particle and each fluid time step. Also, the concept for liquid/bound water is only applicable to porous material such as wood.

The drying process of coffee beans has been modelled with $Bi \approx 45$, indicating a rather large difference in surface and centre temperatures (see Figure 4.9). The dimensionless temperature of wood particles which are heated with $Bi \approx 0.39$ is less distinctive (see Figure 4.1), however still highlights the importance to resolve

a temperature (and species concentration) profile in 1D along the particle radius for 500μm wood particles. For fluidised bed applications, inert particles (sand) do not need to be resolved, as they stay roughly at the same temperature. They can be treated as thermally thin (unresolved).

Coffee bean roaster simulations have been applied to conditions given by Hyed et al. [77]. 780 particles are modelled as discrete, spherical, isotropic but inhomogeneous particles where the temperature and moisture content profiles are resolved in 1D. Particle data have been analysed based on their location, mixing, heat and mass transfer coefficients and particle-fluid interactions. The advantage over all other existing coffee bean models is that it provides much more detailed information at all levels: particle flow-scale, particle-scale and sub-particle scale. Although many sub-models can be included for future studies (e.g. pyrolytic reaction model, varying diffusivity or conductivity inside the particle), the model predictions are in generally good agreement with experimental data.

All simulations were run on a single node desktop pc (3.2GHz, 4GB RAM). The entire batch coffee bean drying process of 10 minutes real drying time was modelled in less than 24 hours simulation time.

Chapter 5

Fast Pyrolysis of Biomass Particles

In this chapter, fast pyrolysis modelling of biomass particles has been analysed in detail. First, a state-of-the-art pyrolysis model for single large particles has been investigated by discussing its ability to model many particles. Then, fast pyrolysis in a bubbling fluidised bed has been modelled, reproduced to a large extend and scrutinised with the help of DEM. The 3D model is compared to experimental results from a 100g/h bubbling fluidised bed pyrolyser and delivers variables such as particle composition at the outlet and gas/vapour/water yields as a function of fluidisation conditions, biomass moisture concentrations and bed temperatures. Multiprocessor simulations on a high-end computer have been carried out to enable the tracking of each of the 0.8 million individual discrete sand and biomass particles, making it possible to look at accurate and detailed multiscale information (i.e. any desired particle property, trajectory, particle interaction) over the entire particle life time. The overall thermochemical degradation process of biomass is influenced by local flow and particle properties and therefore accurate and detailed modelling reveals unprecedented insight into such complex processes. It has been found that the temperature and superficial fluidisation velocity is important, while the particle moisture content is less significant for the final bio-oil yield.

5.1 Fast Pyrolysis of Single Particles

Simulations of single, non-moving, thermally thick biomass particles have been performed to look at generally applied methods to describe the thermochemical

degradation of particles. The temperature and species concentrations computed are resolved along the radius. First, this section introduces the model theory used for single particles followed by a discussion of results obtained.

5.1.1 Theory and Model Description

It is generally accepted that thermochemical conversion of biomass leads to decomposition into the main products gas, tar and char. The released gas is a mixture mainly of CO, CO_2 and some smaller quantities of H_2 and C_1-C_2 hydrocarbons. Tar contains more than a hundred compounds (phenol, levoglucosan, furfural,...) and char is the remaining solid carbon-rich residue when all gases and tars have left the particle. All of these products are rather complex and further analysis is mostly restricted to experimental work. The thermochemical degradation of biomass/wood is most often numerically described by means of chemical reaction models. The simplest of all are single-step reaction models of the following form:

$$\text{Wood} \xrightarrow{k_1} f(1-\chi)\text{Gas} + (1-f)(1-\chi)\text{Tar} + \chi\text{Char}. \tag{5.1}$$

where f and χ are constants defining a fixed ratio between 0...1. Biomass consists mainly of cellulose, hemicellulose and lignin, and often the degradation behaviour is retraced back to its components. Gronli [152] pointed out that the thermochemical degradation process of wood is improved by an independent parallel reaction model [161] by considering its main constituents leading to a reaction mechanism shown as follows:

$$\left.\begin{aligned}\text{Cellulose} &\xrightarrow{k_1}\\ \text{Hemicellulose} &\xrightarrow{k_2}\\ \text{Lignin} &\xrightarrow{k_3}\end{aligned}\right\} \quad f(1-\chi)\text{Gas} + (1-f)(1-\chi)\text{Tar} + \chi\text{Char}. \tag{5.2}$$

Under low heating rates, char is the main pyrolysis product, while for high heating rates little or no char and high tar formation is observed [162]. This phenomenon cannot be taken into account by the reaction models described above because f and χ are constant product ratios independent of temperature or heating values. This thermochemical degradation behaviour during fast pyrolysis has to be captured by a reaction model with competing chemical pathways. Figure 5.1 illustrates the reaction model introduced by Shafizadeh and Chin [163] which is most often applied in fast pyrolysis simulations [88, 92, 162] and is considered herein

as state-of-the-art. This reaction model consists of two stages, primary pyrolysis which describes biomass degradation into different fractions of main products depending on temperature and heating rates. The second stage considers tar to be partially converted into gas and char due to thermal cracking, recondensation and repolymerisation - known as secondary tar reactions. Secondary tar reactions are undesired but consideration in reaction models can significantly improve the prediction of tar yields under certain conditions.

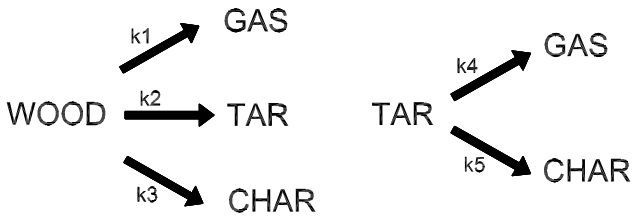

FIGURE 5.1: Two-stage, semi global model

Secondary tar reactions take place both inside pores of the solid material where the vapour gases migrate towards the particle surface and in the gas phase after tars have been released. This model does not take into account a remaining particle char layer where gas and tar need to pass through. In practice, char acts as a catalyst and enhances secondary tar reactions and therefore can strongly reduce the bio-oil yield. Secondary tar reactions in the gas phase are important under high gas temperature and long vapour residence times. Secondary tar reactions in the gas phase have been neglected in this study.

Reactions can be adequately represented as first order in case of pyrolysable material, having an Arrhenius type of temperature dependence [164] where A is the preexponential factor, E is the activation energy, R_u is the universal gas constant and k is the reaction rate given as

$$k = A \exp\left(-\frac{E}{R_u T}\right). \tag{5.3}$$

Based on the reaction scheme described above, mass conservation equations for wood, char, tar and gas can be expressed as follows, where k_1, k_2, k_3, k_4 and k_5 are reaction rates between substance and products as depicted in Figure 5.1. Kinetic parameters refer to pine wood and have been taken from Chan et al. [165] for the primary pyrolysis reactions and from Liden et al. [166] and Di Blasi [167] for the

fourth and fifth reaction respectively. All parameters used in this simulation are given in Table 5.1.

$$\frac{dm_{Wood}}{dt} = -(k_1 + k_2 + k_3)m_{Wood} \tag{5.4}$$

$$\frac{dm_{Gas}}{dt} = k_1 m_{Wood} + k_4 m_{Tar} \tag{5.5}$$

$$\frac{dm_{Tar}}{dt} = k_2 m_{Wood} - (k_4 + k_5)m_{Tar} \tag{5.6}$$

$$\frac{dm_{Char}}{dt} = k_3 m_{Wood} + k_5 m_{Tar} \tag{5.7}$$

Eqs. (5.4 - 5.7) are solved in each sublayer at each fluid time step. In this study, 40 sublayers have been used to resolve the temperature and species concentration profiles. The stationary particle is exposed to a high temperature gas flow (as in Section 4.1) and undergoes heating and pyrolysis without drying. In practice, wood properties are different in longitudinal, radial and tangential direction. This model assumes spherical, non-shrinking particles with isotropic properties. Furthermore, the assumption has been made that created tar inside the particle reaches the particle surface (is released) in one fluid time step (10^{-2} seconds). This is according to the work of Papadikis et al. [92, 93], where convective tar transport inside the particle has not been considered. Unfortunately, the same problem is present in this work too, so that it is not possible to account for a better approximation for tar residence times.

The time-step which has been used to integrate explicitly the chemical reaction model (eqs. (5.4-5.7)) has been checked for 0.1, 0.01 and 0.001 seconds and results are shown in Figure 5.2. It can be seen, that there is hardly any difference by numerically solving the mass degradation of wood by using time-steps of 0.01 and 0.001 seconds. Time-steps of 0.1 seconds lead to very small deviations - indicating a very low time-step dependency of the overall reaction model. A time-step of 0.01 seconds is used for the subsequent results shown indicating a correct integration of the reaction model.

The energy equation in eq. (4.9) now becomes

$$\frac{\partial(\rho c T)}{\partial t} \approx \overline{\rho c}\frac{\partial T}{\partial t} = \frac{1}{r^2}\frac{\partial}{\partial r}\left(\lambda_p r^2 \frac{\partial T}{\partial r}\right) + \Delta H \frac{\partial \rho}{\partial t}, \tag{5.8}$$

where the same boundary conditions apply as in eq. (4.12). Convective heating is the only heat transfer mechanism considered to heat the particle and the

TABLE 5.1: Pyrolysis model parameters

Quantity	Symbol	Value	Reference
Particle diameter	d_p	$0.0005\ m$	
Fluid velocity	u_f	$1.2\ m/s$	
Fluid temperature	T_f	$773\ K$	
Fluid density	ρ_f	$0.435\ kg/m^3$	
Fluid viscosity	μ_f	$3.51 \cdot 10^{-5}\ kg/ms$	
Fluid conductivity	λ_f	$0.0537\ W/mK$	
Wood density	ρ_{Wood}	$650\ kg/m^3$	[168]
Char density	ρ_{Char}	$220\ kg/m^3$	estimated
Wood heat capacity	$c_{p,Wood}$	$1500\ J/kgK$	[168]
Char heat capacity	$c_{p,Char}$	$1100\ J/kgK$	[168]
Wood conductivity	λ_{Wood}	$0.1256\ W/mK$	[169]
Char conductivity	λ_{Char}	$0.0837\ W/mK$	[169]
Activation energy	E_1	$140 \cdot 10^3\ J/mol$	[165]
Activation energy	E_2	$133 \cdot 10^3\ J/mol$	[165]
Activation energy	E_3	$121 \cdot 10^3\ J/mol$	[165]
Activation energy	E_4	$108 \cdot 10^3\ J/mol$	[166]
Activation energy	E_5	$108 \cdot 10^3\ J/mol$	[167]
Preexponential factor	A_1	$1.3 \cdot 10^8\ s^{-1}$	[165]
Preexponential factor	A_2	$2.0 \cdot 10^8\ s^{-1}$	[165]
Preexponential factor	A_3	$1.08 \cdot 10^7\ s^{-1}$	[165]
Preexponential factor	A_4	$2.6 \cdot 10^6\ s^{-1}$	[166]
Preexponential factor	A_5	$1.0 \cdot 10^6\ s^{-1}$	[167]
Primary reaction enthalpy	$\Delta H_{1,2,3}$	$418.0\ kJ/kg$	[165]
Secondary reaction enthalpy	$\Delta H_{4,5}$	$-42.0\ kJ/kg$	[85]

convective heat transfer coefficient in eq. (4.13) has been used. Species transport inside particles is not considered. Heat capacity and thermal conductivity for each component and density of solid compounds (wood and char) are constant while the rule of mixture applies (updated for each particle layer in each fluid time step) according to

$$\lambda_p = \lambda_{Char} + (\lambda_{Wood} - \lambda_{Char}) Y_{Wood}, \tag{5.9}$$

$$\overline{\rho c} = \rho^*_{Wood} c_{Wood} + \rho^*_{Char} c_{Char}. \tag{5.10}$$

The amount of wood converted into the three products is dependent on the kinetic rates and in turn on the temperature. However, the amount of mass change during this endothermic process has again a temperature effect. First, eqs. (5.4-5.7) are solved with an old temperature value, followed by solving the energy equation with a new species concentration (as described in Appendix A). Then, this process is

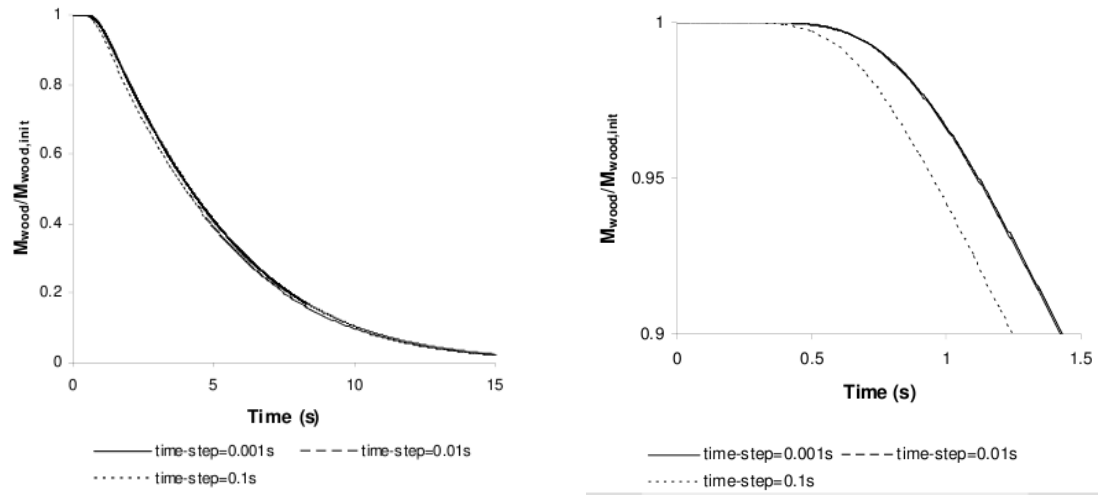

FIGURE 5.2: Time-step dependency check of the chemical reaction model shown in Figure 5.1; left: Chemical time scale for the overall degradation of a wood particle with properties given in Table 5.1 and right: A more resolved section of the left figure.

repeated by using an an underrelaxation factor of 0.8 for the temperature until the temperature satisfies a convergence criteria. When no pyrolytic reactions take place no underrelaxation is used. For the single particle considered, the number of iterations per time step vary form one (when no pyrolysis heat source is considered) to about 40 when pyrolysis reactions are intense. The procedure used to solve the partial differential equations is semi-implicit in that, even though implicit schemes are used, the coupling among equations is treated through iterations.

5.1.2 Results and Discussion

Figure 5.3a shows the temperature profile inside the particle for a gas temperature of 773K. During heating a temperature gradient is present which reduces in time. The overall process is endothermic and the particle does not reach the gas temperature level right after the start. Within roughly two seconds a rather constant temperature profile along the radius is established which is somewhat below the gas temperature level. After thermochemical degradation declines, the particle temperature rises towards the gas temperature of 773K - which is not shown in the figure. Herein, the convective heat transfer coefficient in eq. (4.13) does not represent fast pyrolysis conditions in fluidised beds - therefore temperature gradients are expected to be slightly higher.

Gas, tar (oil) and char yields obtained from a pine wood particle of 500μm in diameter exposed to different gas temperatures are shown in Figure 5.3b. Higher

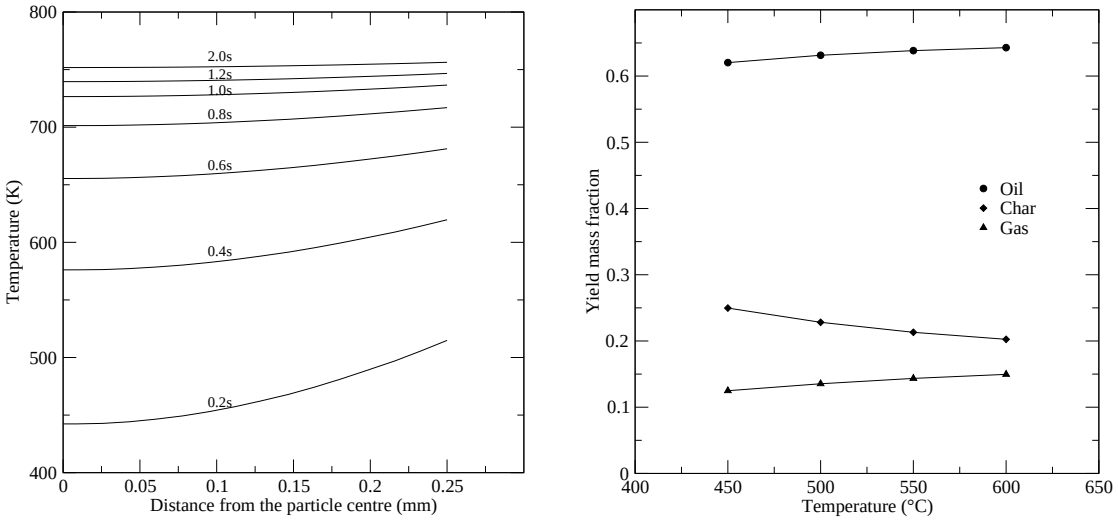

FIGURE 5.3: a) Spatial temperature profiles inside the sphere exposed to 773K and b) yield fractions as a function of gas temperature

temperature causes a higher gas yield and lower char yield which corresponds to other studies [162]. The maximum tar yield is reached most often around 500^oC [170, 171] while this model predicts higher oil yields at even far higher temperatures. The reason for such discrepancy is that the present model does not account for correct secondary tar reactions. Secondary tar reactions are less important for temperatures below 773K and they become significant for higher temperatures [172–174]. Hence, the assumption to choose the tar residence time according to the fluid time step is not appropriate - a complete convective gas transport model inside the particle is required.

The bio-oil yield reduces when larger particles are taken into account as shown in Figure 5.4a. The oil-yield reduction occurs due to the resolved heat transfer method only. In practice, secondary tar reactions are much more intense inside larger particles due to longer gas hold up and the presence of char. For larger particles than 500μm in diameter, the simplified approach to model fast pyrolysis leads to erroneous predictions as pointed out by Di Blasi [162,167]. Similarly, only thermally thin particles can be correctly modelled unless a complete convective transport model inside the particle is used.

The kinetic model shown in Figure 5.1 requires three kinetic rates which need to be determined from experiments. Di Blasi [106] summarised all published kinetic data available for this reaction model, being in total, five. Their maximum (no secondary tar reactions considered) oil-yield is depicted as a function of temperature in Figure 5.4b. There are two pine wood data shown which distinguish a lot

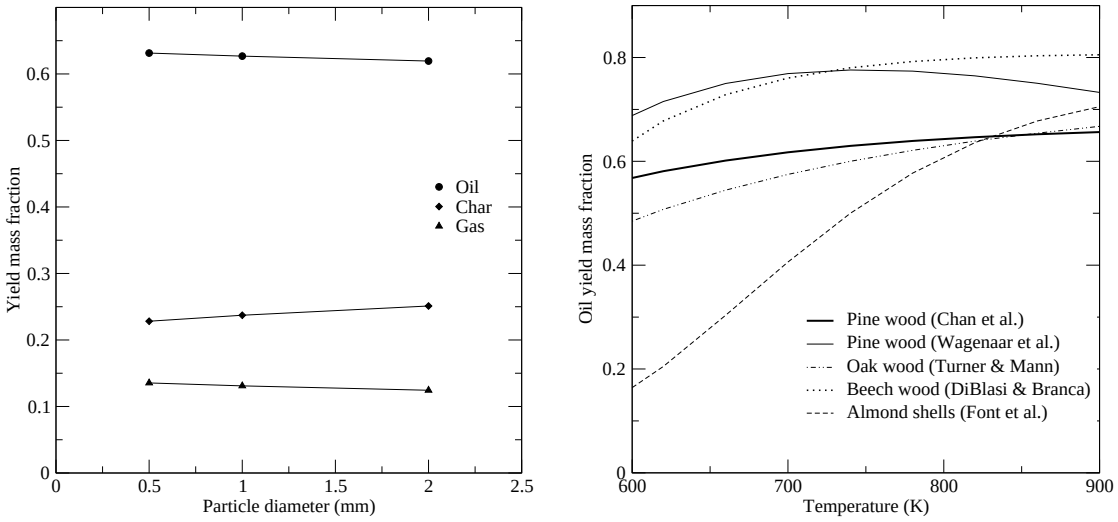

FIGURE 5.4: a) Yield fractions as a function of particle size and b) maximum oil-yield for different biomass feedstocks from Chan et al. [165], Wagenaar et al. [175], Thurner & Mann [164], Di Blasi & Branca [176] and Font et al. [177]

due to different feedstock size and pyrolysis conditions. When another feedstock or reactor condition is of interest, this reaction model does not seem to be applicable.

The reaction model shown in Figure 5.1 is generally accepted for biomass pyrolysis. However, it relies on kinetic data which are determined under very specific experimental conditions (particle size, heating rate, reactor domain) and cannot be easily used for general applications as found in fluidised beds. This reduces the validity of this overall kinetic approach.

For multiple particle degradation studies, thermally thick particles are too computationally demanding. Pyrolysis requires more and much smaller particles as they are processed in drying applications which indicates that thermally thick pyrolysis modelling of numerous particles is challenging. Particles need to be small enough to predict accurate results. If possible, this reaction model is very limited for future studies and is better replaced by a more generic approach to describe the thermochemical degradation process of biomass.

5.2 Fast Pyrolysis of Multiple Particles

This section investigates fast pyrolysis of many thermally thin biomass particles from a particle-scale perspective without disregarding the largest scales present in fluidised beds. The modelled process is semi-continuous in the sense that it is modelled from the moment when biomass feeding is started to the moment

when the main variables (i.e. the amount of gas/tar/water in the gas phase) are converged to steady-state, which has been approximately achieved after five seconds. Mixing, segregation and entrainment of the biomass phase in the reactor are analysed and the impact on and change of particle properties throughout their entire particle life-time has been monitored.

5.2.1 Theoretical Model

This section deals with a detailed description of the modelling assumptions and methods used. A different approach from Section 5.1 has been used which is described herein.

5.2.1.1 Fluid-Phase Modelling

The fluid-phase is modelled as a continuum, known as an Eulerian type model and is considered to be a mixture of nitrogen as the inert fluidisation gas and water vapour, tar and non-condensible gases released during the degradation process of biomass particles. The volume-averaged fluid phase continuity, momentum, energy and species transport equations are solved for each time step associated with the fluid. Partial differential equations describing the fluid phase are given in Sections 3.1 and 4.1. Turbulence is suppressed in dense particle regions due to high solid volume fractions while in dilute particle regions (bubbles) turbulence might affect only slightly particle trajectories or reactions. Van der Hoef et al. [5] argued that turbulence in fluidised beds is suppressed even for moderately high particle Reynolds numbers (<2000). To assume laminar flow is therefore believed to be a good approximation [135, 178]. The particle motion in the freeboard is assumed to be controlled by splashing rather than turbulent diffusion [136]. In this work, no chemical reactions are considered in the gas phase so that there is no specific need to resolve turbulence.

5.2.1.2 Particle-Phase Modelling

The general description of the particle phase is given in Section 3.2. The collision model is based on physical particle and wall properties with the following values: Young's modulus $E = 5 \cdot 10^5 Pa$ [144], Poisson ratio $\nu = 0.3$ [44, 94], friction coefficient $\mu = 0.3$ [8] and the coefficient of restitution $e = 0.95$ [8]. All values are equally valid for walls and particles.

Heat transfer at the particle surface is considered to occur by a combination of convective and radiative mechanisms. Particle-particle radiation must be included in fast pyrolysis studies to accurately predict the tar yield [104]. The conductive inter-particle heat transfer contribution compared to convection and radiation has been found to be less than 5% for conditions used in this work ($\lambda_{Wood} = 0.12W/mK$, in fluidised beds u_f=3u_{mf}, T≈ 500^{o}C) [94, 95, 104, 147] and thus has not been considered in this thesis. Latent heat during water evaporation and heat of reaction during pyrolysis are applied. In that case, the zero-dimensional particle energy equation is expressed as:

$$\begin{aligned} m_p c \frac{\partial T_p}{\partial t} &= -hA(T_p - \widetilde{T}_f) - \omega\sigma A(T_p^4 - T_{bed}^4) \\ &-H_{evap}\Delta S_{H_2O} - H_{1/2/3}\Delta S_{1/2/3} \end{aligned} \tag{5.11}$$

where ω is the particle emissivity and the Stefan Boltzmann constant is $\sigma = 5.67 \cdot 10^{-8} W/(m^2K^4)$. $\widetilde{T}_f$ represents the interpolated fluid temperature as seen by the particle, H is the heat of reaction to evaporate water (latent heat) or one of the three pyrolysis reactions discussed in the next section and ΔS is the source term of the reactant. Due to low gas emissivities, gas radiation is not considered. The bed temperature T_{bed} is averaged over all particle temperatures in the present and adjacent particle cells given as:

$$T_{bed} = \frac{1}{N_{nb} + 1} \left(T_p + \sum_{i=1}^{N_{nb}} T_{p,i} \right). \tag{5.12}$$

The convective heat transfer coefficient $h = Nu\lambda_f/d_p$ for individual particles in bubbling beds is taken from the Nu correlation of Gunn [179] valid for a wide range of particle volume fractions (0...0.65).

$$\begin{aligned} Nu &= \left(7 - 10\epsilon + 5\epsilon^2\right)\left(1 + 0.7Re_p^{0.2}Pr^{1/3}\right) \\ &\quad + \left(1.33 - 2.4\epsilon + 1.2\epsilon^2\right) Re_p^{0.7}Pr^{1/3} \end{aligned} \tag{5.13}$$

5.2.1.3 Drying and Pyrolysis Model

All particles in this work are treated as thermally thin where any transport mechanism within the particle is negligible. To conserve each solid or liquid species i, the general conservation equation is solved according to:

$$\frac{\partial \Phi_i}{\partial t} = S_i. \tag{5.14}$$

In fast pyrolysis applications, biomass particles experience very high heating rates and drying occurs almost regardless of moisture concentration gradients between surface and the local gas environment. Therefore, drying can be seen and simplified as a boiling process around 100°C by a thermodynamic balance between the energy needed to evaporate water and the energy transferred from the local sourrounding to the particle. In this model, evaporation takes place when $T > T_{evap}$ while the amount of water exchanged between the particle and the local gas environment is given by its source term as:

$$S_{H_2O} = MIN\left(\frac{(T - T_{evap})m_p c}{H_{evap}\Delta t}, \frac{Y m_p}{\Delta t}\right). \tag{5.15}$$

After updating the water content Y, the particle density is solved according to eq. (4.11) and the heat capacity is given by:

$$c = c_{H_2O} Y + c_{SD}(1 - Y). \tag{5.16}$$

The thermochemical degradation process of biomass can be modelled in different ways [106]. In this Section 5.2, primary pyrolysis is modelled by a generalised reaction scheme with competing chemical pathways proposed by Miller and Bellan [180]. The model is based on a superposition of kinetics of the primary components of biomass: cellulose (C), hemicellulose (H) and lignin (L) as depicted in Figure 5.5. Multi-step, first-order, irreversible Arrhenius reactions are used where all kinetic parameters are summarised in Table 5.2. This pyrolysis mechanism is widely used for cellulose [182] and has been extended in the same way by Miller and Bellan [180] for the other two components. The model is based on a re-examination of literature data and found to be capable of making robust predictions of pyrolysis behaviour for a variety of conditions and feedstocks [180].

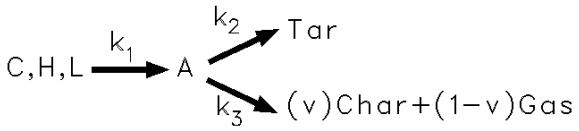

FIGURE 5.5: Semi-global multi-component mechanism for biomass pyrolysis

The initialisation reaction (k_1) is thought of as a repolymerisation step and does not produce any mass change or reaction heat. Therefore, wood is modelled as a composition of the three activated and non-activated components as $X_W = X_C + X_H + X_L + X_{AC} + X_{AH} + X_{AL}$. Furthermore, all mass fractions X are based on the constant initial dry solid wood mass, so that the equation $X_{Wood} + X_{Char} +$

Table 5.2: Kinetic parameters for the three main components of the generalised biomass model [180]

	Components			Reaction heat
	Cellulose(C)	Hemicellulose(H)	Lignin(L)	/ References
k_1	$2.80 \cdot 10^{19} \exp(-242.4/RT)$	$2.10 \cdot 10^{16} \exp(-186.7/RT)$	$9.60 \cdot 10^{8} \exp(-107.6/RT)$	0 kJ/kg
k_2	$3.28 \cdot 10^{14} \exp(-196.5/RT)$	$8.75 \cdot 10^{15} \exp(-202.4/RT)$	$1.50 \cdot 10^{9} \exp(-143.8/RT)$	+255 kJ/kg
k_3	$1.30 \cdot 10^{10} \exp(-150.5/RT)$	$2.60 \cdot 10^{11} \exp(-145.7/RT)$	$7.70 \cdot 10^{6} \exp(-111.4/RT)$	−20 kJ/kg
v	0.35	0.60	0.75	−
Red oak	46.9%	31.8%	21.3%	[181]

Table 5.3: Terminal velocity of sand, virgin wood and char particles

Criteria	Formula	Sand	Dry virgin wood	Char residue
Terminal velocity ($u_0 = 0.365$ m/s)	$u_t = \sqrt{\frac{4}{3}\frac{d_p g(\rho_p - \rho_f)}{\rho_f C_D}}$	2.45 m/s	1.19 m/s	0.574 m/s
Terminal velocity ($u_0 = 0.76$ m/s)		3.20 m/s	1.56 m/s	0.766 m/s

TABLE 5.4: Property settings for the particle and fluid phase

Property	Value	Unit	Sources
Wood specific heat (dry)	$c_{DS} = 1112.0 + 4.85T_p$	J/kgK	[183]
Char specific heat	$c_{Char} = 1003.2 + 2.09T_p$	J/kgK	[184]
Sand specific heat	$c_{Sand} = 860$	J/kgK	[185]
Red oak density (dry)	$\rho_{DS} = 660$	kg/m^3	[59]
Char density	$\rho_{Char} = 350$	kg/m^3	[169]
Sand density	$\rho_{Sand} = 2600$	kg/m^3	[186]
Solid emissivity	$\omega = 0.8$	–	[94]
Fluid density	$\rho_f = \frac{p}{R_u T_f} \sum_i W_i Y_{m,i}$	kg/m^3	[185]
Sand diameter	$d = 520$	μm	–
Initial biomass diameter	$d = 500$	μm	–
Initial moisture content	$X = 0.161/0.7$	$\mathrm{kg_{H_2O}/kg_{DS}}$	–
Superficial gas velocity	$u_0 = 0.365/0.760 (u_0 = 1.3/3u_{mf})$	m/s	–
Number of sand particles	$N = 600711$	–	–
Number of wood particles fed	$N = 37724/36764$	1/s	–

$X_{Gas}+X_{Tar} = 1$ is valid at any time during the simulation. Note that Y is the mass fraction based on the total mass which can alter. Mass fractions for gas and tar are recorded for post-processing reasons only. For each individual biomass particle an additional set of nine ordinary differential equations of the form given in eq. (5.14) are solved for the pyrolysis model; for each activated (A) and non-activated component and the three products tar, char and gas. Due to the small biomass size, intra-particle secondary tar reactions are negligible [85] so that condensible and non-condensible gases are released at the particle surface instantaneously. A particle property Φ is updated linearly depending on its composition as:

$$\Phi = \Phi_{Char} + (\Phi_{DS} - \Phi_{Char})\, X_{Wood} \tag{5.17}$$

for $\Phi = \rho, c$ as given in Table 5.4. Shrinkage during the drying process is neglected while during pyrolysis mass-proportional shrinkage [8,187,188] is assumed for each biomass particle. To conserve mass at any instant of time, the biomass particle diameter shrinks according to:

$$d_p = \sqrt[3]{\frac{6}{\pi}\frac{m_p}{\rho_p}}. \tag{5.18}$$

It is further assumed that reactions are uniform throughout the particle and the ash layer (if exists) peels off instantaneously (see Figure 5.6). Although, shrinkage has a negligible effect on pyrolysis for small particles [59], the remaining char particle volume and mass strongly affect particle trajectories on its way out of

the reactor. High heating rates produce only little char formation [162] so that without particle shrinkage char entrainment would be highly over-predicted.

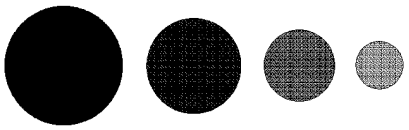

FIGURE 5.6: The applied progressive shrinkage mechanism for biomass particles

5.2.1.4 Experiments and Simulation Setup

Experiments have been performed at Iowa State University on a cylindrical fast pyrolysis bubbling fluidised bed reactor, with dimensions shown in Figure 5.7. An outside-cooled side pipe (attached radially 2.54cm from the bottom) feeds fine red oak biomass particles with a screen size of 500μm by a rotating shafted screw feeder with a rate of 100g/h into the reactor. Nitrogen, water vapour, char particles, condensible and non-condensible gases leave the reactor through the outlet at the top where they get separated subsequently by travelling through cyclones, condensers and an electrostatic precipitator. Electrical heaters surrounding the reactor vessel are used to maintain pyrolysis at the desired reaction temperature and to ensure to a best degree adiabatic wall conditions. After pre-heating inside the plenum, pure nitrogen enters the bottom perforated distributor plate and fluidises the sand bed. The distributor plate consists of 31 holes with a diameter of 1.65 mm each while the bottom distributor plate in the simulation has an inlet velocity of zero except for the 31 cell faces coloured black in Figure 5.8b. The nitrogen flow through these 31 cells is thought to be a better approximation than the often assumed plug flow through all inlet cells. The reactor has been recently modified after the process has been numerically investigated by Xue et al. [105]. They have used a few different geometrical dimensions and initial/boundary conditions different to the ones used in this work.

The gas flow through the plenum and the particle feeding process in the attached feeding tube are not modelled. Biomass particles (black colour) are inserted at the side of the domain as shown in Figure 5.7 and travel with the same constant feeding speed towards the bed centre. This resembles biomass feeding by a screw which presses the biomass into the reactor without using a carrier gas. Particle trajectories are updated normally according to the second law of Newton as soon as they made space for a new batch of virgin biomass particles to be inserted. As particles can only be inserted into voids (no artificial overlaps with other particles

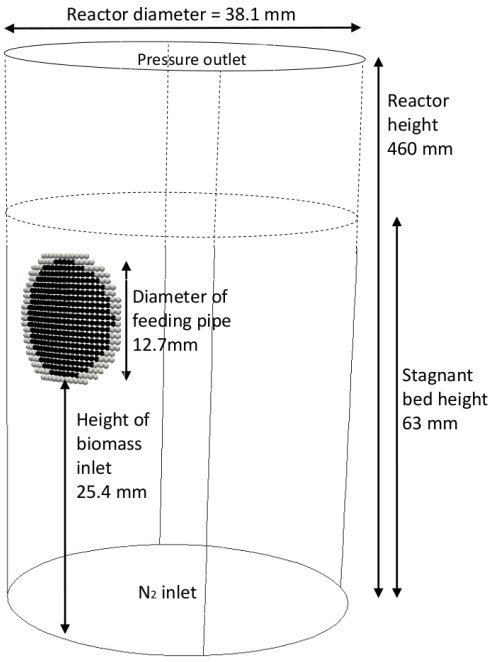

FIGURE 5.7: Reactor dimensions including one batch of biomass particles (black) surrounded by non-moving sand particles (grey)

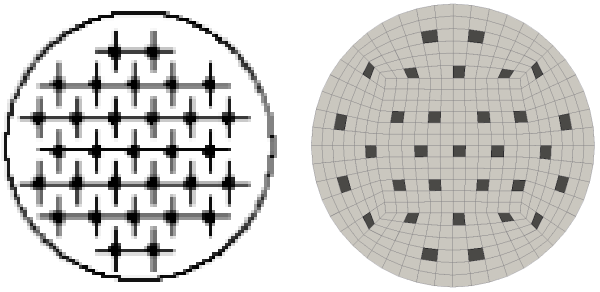

FIGURE 5.8: Perforated bottom distributor plate in (a) the experiment and (b) the simulation

are allowed), a circular layer of non-moving sand particles (gray colour) along the wall is simulated to avoid that other particles enter that area. In the simulation, a batch consists of 318 biomass particles, which are inserted simultaneously. To achieve a feeding rate of 100g/h, roughly 115 batch injections are made every second. This corresponds to roughly 37000 virgin biomass particles entering the domain per second. This depends slightly on the chosen initial biomass moisture content of 7.0 or 16.1%. The composition of biomass in terms of cellulose, hemicellulose and lignin are typical for red oak (see Table 5.2). Extractives and ash content are incorporated in the hemicellulose component as proposed by Miller and Bellan [180]. In the model, biomass feeding is started after stable fluidisation which is achieved in about 5 seconds of real time. Silica sand is used as the bed material

with a particle diameter of $520\mu m$. Nitrogen, water vapour, condensible and non-condensible gases are modelled as individual Euler phases. Nitrogen enters the bed from the bottom with a uniform temperature of 758/699 K and a mass flow rate of 52/42/26 l/min. The thermal conductivity, heat capacity and dynamic viscosity of the fluid have been assumed to be that of nitrogen at a pressure of $1.013 \cdot 10^5 Pa$ and the selected pyrolysis temperature. Table 5.4 summarises all property settings for the particle and fluid phase. As a simplification, fluid properties are assumed to be those of nitrogen at 758K $\lambda_f = 0.0528 W/mK, \nu_f = 3.461e^{-5} m^2/s$ and $c_{p,f} = 1.113 J/kgK$ and at 699K $\lambda_f = 0.0496 W/mK, \nu_f = 3.2771e^{-5} m^2/s$ and $c_{p,f} = 1.097 J/kgK$. The cylindrical domain has 432 cells in X-Y plane and 230 cells in Z direction (reactor height). A fluid time-step of $5 \cdot 10^{-5}$ seconds has been chosen to solve the stated problem.

The initial sand and gas temperature in the domain are set equal to the inlet gas temperature of 758/699K. It has been assumed, that injected virgin biomass particles enter the domain with a temperature of 323K. At walls, adiabatic and no-slip boundary conditions for the fluid-phase are applied while particles are allowed to slip freely. Energy transfer between particles and walls are neglected (zero-flux boundary condition). For the bottom distributor plate, Dirichlet boundary conditions are employed for all fluid variables, while particles experience the same boundary conditions as for walls. Particles are removed instantaneously when they reach the outlet at the top of the domain. The pressure at this boundary is fixed to a reference value of $1.013 \cdot 10^5 Pa$. The fluid velocity is calculated from that pressure and Neumann boundary conditions are applied for the temperature and species mass fractions requiring a fully developed fluid flow.

The following major assumptions and justifications are made for the simulation work and can be summarised as follows:

1. In this work, all biomass particles are treated as zero-dimensional thermally thin point sources, although $Bi \approx 0.75$. According to Bryden et al. [59], particles belong to the thermally thick regime if $0.2 < Bi < 10$, indicating temperature and species gradients inside particles exist but do not necessarily affect drying or pyrolysis times. Koufopanos [85] postulated that for biomass particles bigger than 1mm in diameter, the internal heat transfer and secondary pyrolysis reactions are important.

2. Secondary tar reactions in the gas phase are not taken into account. A first simple criterion for the significance of secondary tar reactions in the gas

phase of the reactor is given by Lathouwers and Bellan [104]. They proposed that the tar-to-gas conversion mechanism is of importance as long as

$$\tau_R/\tau_t = \frac{L}{u_0} A_t \exp(-E_t/R_u T_f) > 0.1, \tag{5.19}$$

where τ_R is the mean gas residence time, τ_t is the tar conversion time scale, $A_t = 4.28e^{+6}$ 1/s and $E_t = 108.0$ kJ/mol [180]. In this work, for a temperature of 758 K and a fluidisation velocity of 0.76 m/s, $\tau_R/\tau_t \approx 0.09$. They further pointed out that small lab-scale reactors are able to operate without significant tar-to-gas conversion while secondary tar reactions in large-scale reactors are significant due to higher domain heights L.

3. In this work, shrinkage due to drying (4-7%) is too small to significantly impact drying times and therefore has a negligible impact on the final product yield [59].

5.2.2 Results and Discussion

Work has been carried out to investigate the effects of different distributor plates and their impact on the bed hydrodynamics. Then, the thermochemical conversion from solid virgin wood particles to condensible vapours (bio-oil) has been studied under different conditions. This includes different (1) superficial fluidisation velocities and therefore a bubbling bed behaviour, (2) biomass moisture contents and (3) reactor temperatures. Analysis has been conducted based on the origin of entrained particles and the underlying mechanism for entrainment in this small-scale reactor.

5.2.2.1 Fluidisation of Sand

Figure 5.9 depicts the fluidisation of the sand bed for different superficial velocities and inlet distributor plates. The higher inlet velocity ($u_0 = 0.76$ m/s) has been chosen according to experiments and provokes a rather vigorous fluidisation. The bubble size is usually big ($d_B > D/3$) and the fine sand particles are raining down mainly at the cylinder walls indicating an axial slugging behaviour [1]. A rather faint bubble formation is observed for a superficial velocity of $u_0 = 0.365$ m/s predominantly in the lower part of the reactor. Herein, bubbles still contain a rather high fraction of solids.

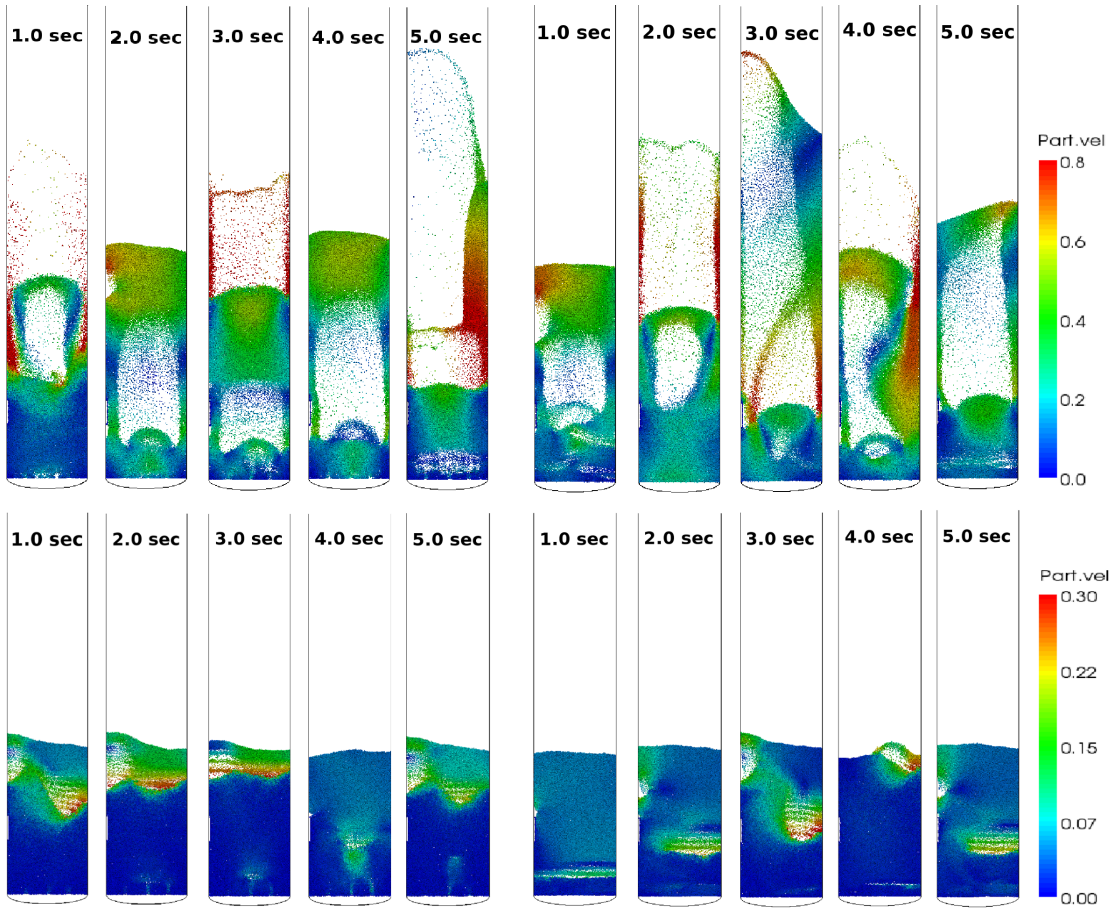

FIGURE 5.9: Particle velocity magnitude (m/s) under different fluidisation conditions - $u_0 = 0.76$ m/s at the top and $u_0 = 0.365$ m/s at the bottom; perforated distributor plate (Figure 5.8) to the left and plug flow inlet to the right

The section in which the biomass is fed into the fluidised bed, as illustrated in Figure 5.7, is included in any study throughout this work. Due to different packing and space holding for future biomass feeding, a bypass is created at the left side of the bed (see Figure 5.9). This triggers a higher frequency of bubble formation to the left and affects the overall bubbling bed behaviour. This behaviour is believed to have a negligible effect on averaged degradation statistics and is not unlikely to be present in experiments as well.

Further simulations have been conducted to test the difference between the inlet flow passing only selected orifices/cells (see Figure 5.8) or the entire surface (uniform plug flow). No significant difference related to the bed and bubble characteristics have been observed for both beds. However, a clear distinction between channelling and plug flow is observed in the bottom part of the bed. Channelling flow above orifices bridges dead zones (hardly moving particles at the bottom) and generates bubbles preferably in the middle of the bed causing slightly larger

disturbance and better mixing. Flat plug flow bubbles almost stretching across the reactor are created right at the distributor plate itself and grow to rather spherically shaped bubbles when they burst the bed surface. In this 100g/h rig, bubble characteristics are fairly similar in the upper bed section regardless of the distributor plate used. It has been found that the perforated distributor plate slightly improves mixing in the bottom regions of the bed but negligible differences have been found in terms of the overall particle heat transfer and therefore bio-oil yield. Biomass does not even reach the bottom of faintly bubbling beds and if good mixing is achieved as in vigorous bubbling beds, the volume fraction differs not much between both cases and therefore biomass particles are believed to be similarly in contact with sand using plug flow inlets.

5.2.2.2 Injection, Segregation and Drying Prior Pyrolysis

Biomass is continuously pushed by a screw feeder into the reactor without carrier gas and the initial particle temperature is assumed to be 323K. Figure 5.10 shows how biomass particles change their location right after injection. To the left, a general segregation effect is shown where biomass ($\rho \approx 660$ kg/m^3) rises inside the dense sand bed ($\rho_S \approx 2600$ kg/m^3). In this faintly bubbling bed, biomass particles remain together as long as the "biomass bubble" is big enough to rise through the dense sand bed. The separation process between the biomass bubble and newly injected particles is also dependent on how much gas bubbles interfere with the process. There are hardly any biomass particles travelling on their own - except in the biomass bubble wake. At the top of the bed a growing layer of biomass particles are created as long as gas bubbles remain small and only light mixing takes place. In that case, biomass particles are surrounded mostly by other cold biomass particles and pyrolysis is delayed and turns gradually into slow pyrolysis.

To the right of Figure 5.10, injection into a vigorous bubbling bed with strong bubble formation is shown. The large gas bubble originated from the left bottom corner quickly expands to the right and upward direction to reach the freeboard. Such bubbles allow very efficient mixing - particles are literally torn into the gas bubble with high gas velocities and causes disturbance and therefore good particle mixing. This is particularly the case when the gas volume migrates to upper bed areas and gains momentum. The figure shows only particles which have not been completely dried (X >0.005), however all other biomass particles are well distributed throughout the bed (compare Figure 5.11). Biomass bubbles are far smaller and likely being destroyed quickly due to good mixing and they hardly

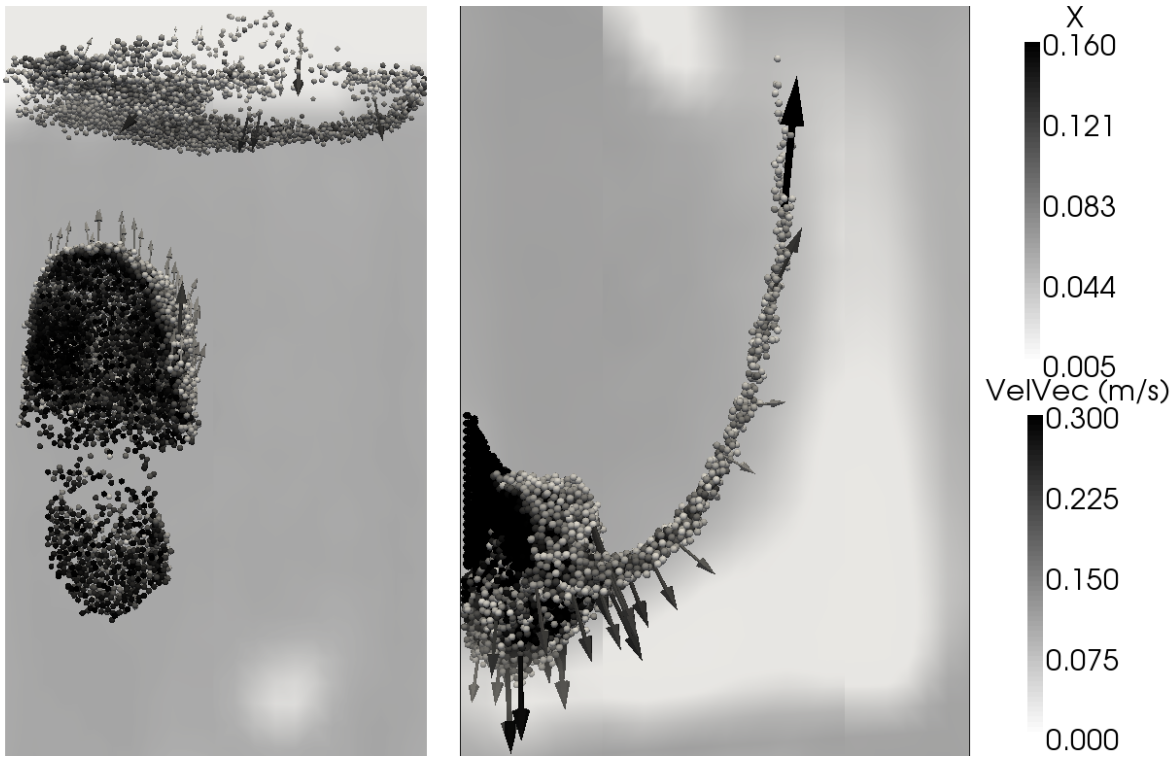

FIGURE 5.10: Biomass particles inside the dense bubbling sand bed during the drying process for $u_0 = 0.365$ m/s (left) and $u_0 = 0.76$ m/s (right). The colour legend refers to the biomass moisture content X and particle velocities (as arrows) shortly after injection. The rest of the bed is represented by high particle volume fractions (dense bed) in gray and low particle volume fractions (bubbles) in white. The sand phase is modelled discrete but visualised non-discrete.

reach the top of the bed in clusters. Biomass particle velocities can be far higher in vigorous bubbling beds.

Bubbling fluidised beds are known for their good heat transfer while circulating beds are usually very effective in mixing. The faintly bubbling bed simulation shows very high heat transfer coefficients around 1000 W/mK, however drying and pyrolysis is less effective lacking in sufficient disturbance and local exchange between sand and biomass. Figure 5.10 reveals the water content of biomass particles and it can be seen that biomass particles inside clusters (left picture) have a rather uniform high water content while an outer thin biomass bubble layer with direct contact to the sand phase shows only little water left. As particles are very small, their overall heat transfer surface area even locally is large and the convective heat transfer is high so that the gas temperature quickly adapts the local particle temperature. A layer of two or three particles (≈1mm) can be enough to prevent particles inside the biomass bubble from fast drying as only

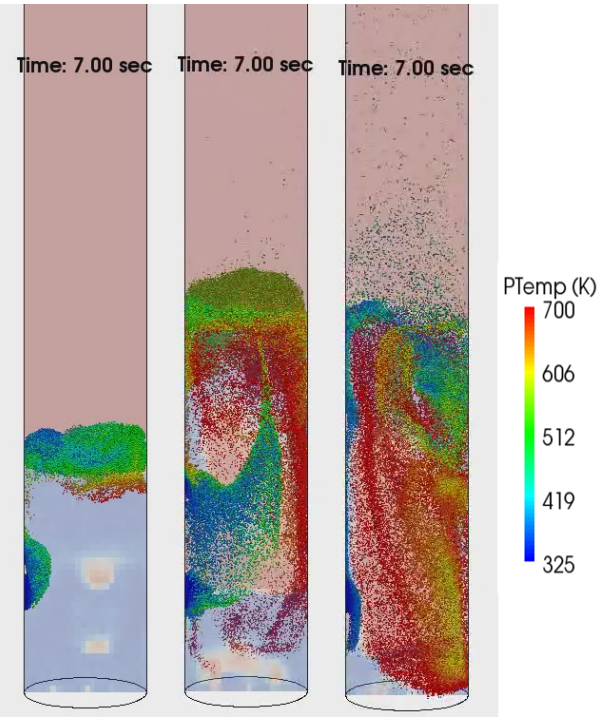

FIGURE 5.11: Biomass distribution at 7 seconds for different superficial fluidisation velocities (u_0=0.356m/s (26 l/min), u_0=0.61m/s (42 l/min), u_0=0.76m/s (52 l/min)). Other conditions: T=758K, X_{H_2O}=16.1%

little moisture has been removed on its way towards to bed surface as shown in Figure 5.10 (left).

TABLE 5.5: Comparison of yield fractions (in %) obtained in experiments and simulations. The yield released by particles is added over all biomass particles in the simulation after 5 seconds of first biomass injection. The time required for drying has been recorded as a maximum, minimum and averaged value originating from the first batch (318 particles injected at the same time).

Bed description (case,T, X_{H_2O})	Experimental results			Results from simulations						
				Pyrolysis				Drying		
	Tar	Gas	Char	H_2O	Tar	Gas	Char	Avg	Max	Min
1, 758K, 16.1%	71.7	12.6	15.7	24.6	52.5	9.7	13.2	0.276s	0.58s	0.13s
2, 758K, 7.0%	65.1	14.6	20.3	9.9	60.8	12.3	17.0	0.257s	0.565s	0.15s
3, 699K, 7.0%	60.2	12.8	27.0	21.7	42.5	14.8	21.0	0.345s	0.71s	0.21s

Table 5.5 summarises the time required to dry wet biomass particles in fluidised beds under different operating conditions, which are numbered from one to three. These values are averaged over one batch (318 biomass particles) injected at the same time. The only difference in the first two cases is the biomass moisture content. It requires more time to evaporate more water - however, other effects like local bubble formation and segregation have an impact on the local heat

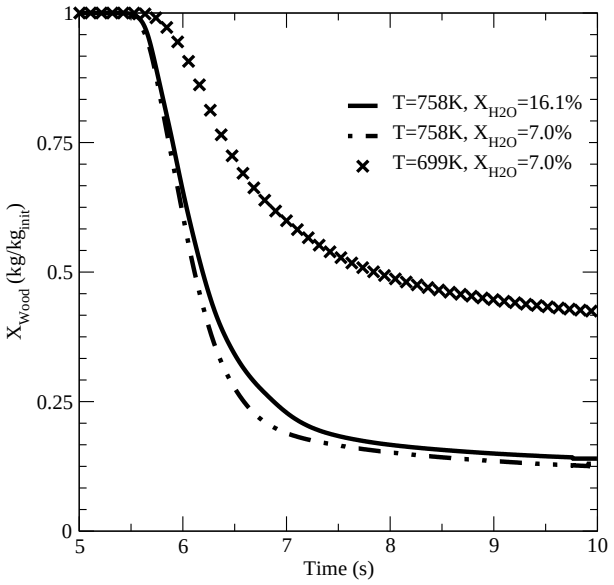

FIGURE 5.12: The remaining unreacted wood portion averaged over the first batch (318 particles) injected at 5 seconds.

transfer and drying times. It has been found that the difference related to the drying time of case one and two is so close (also compare the pyrolysis part in Figure 5.12), that even other effects matter more than the moisture content itself. A bed temperature difference has a much bigger effect on both drying times and pyrolysis degradation.

5.2.2.3 Fast Pyrolysis Modelling

Pyrolysis starts roughly 0.5-1 seconds after injection for the bed conditions studied (Figure 5.12). During that time, particles have probably left the drying region close to the inlet, characterised by the presence of many cold (new) biomass particles and the presence of lower temperature due to latent heat absorption. Figure 5.13 illustrates a particle trajectory and reveals the spatial sections attributed to heating and pyrolysis. The assumption to disregard the first heating stage in fast pyrolysis modelling is well justified. Vapour gases are released appreciably when the biomass particle temperature rises beyond 630K. Similarly to drying, the process time for pyrolysis is strongly linked to the degree of mixing.

Figure 5.11 compares three bubbling beds operated with different superficial velocities. The fluidisation velocity is a very efficient if not the most important parameter to achieve different levels of mixing. Good mixing improves the contact between virgin cold biomass and hot sand and in turn achieves the high heating rates desired. It can be seen in Figure 5.11 that for higher fluidisation velocities

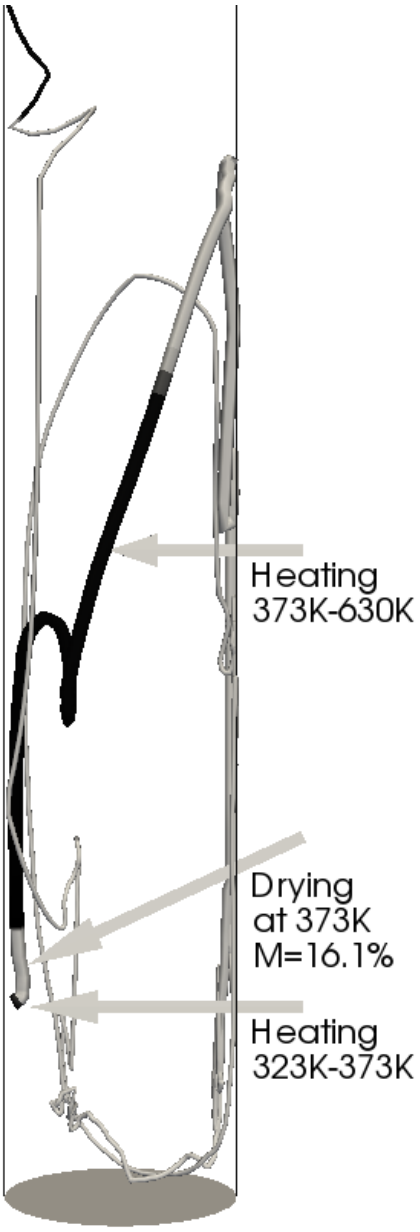

FIGURE 5.13: A single particle trajectory is illustrated showing spatial sections where heating up to 373K (first black section), drying at 373K (white section) and further heating to 630K (another black section) takes place. The particle had a moisture content of initially 16.1%. Pyrolysis prevails along the last white coloured section of the trajectory and has not be seen terminated troughout any of our simulations for any particle.

the average biomass particle temperature within 2 seconds of biomass feeding rises without changing other bed conditions. High tar vapour is produced by particles particularly in areas where high heat transfer is achieved - more precisely when particles are close to the sand phase and inside dense beds where the convective heat transfer coefficient is high. Figure 5.14 reveals the highest tar release for dispersed particles inside the dense bed while particle clusters generally show

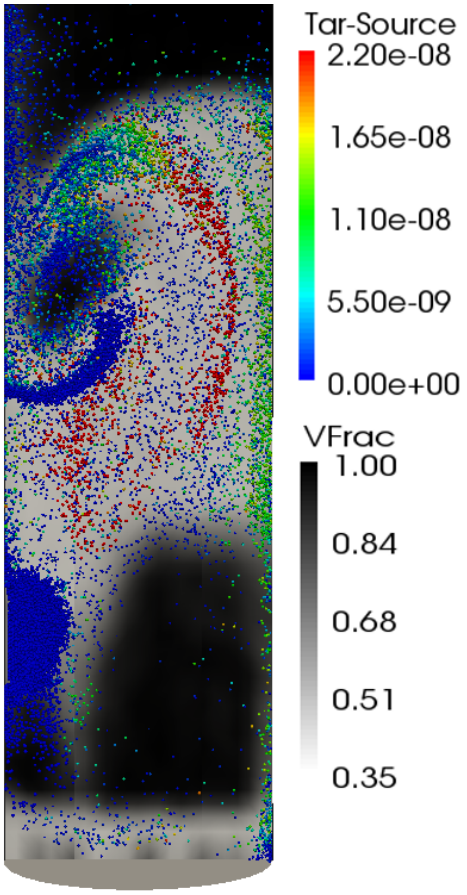

FIGURE 5.14: Tar source terms (kg/s) of individual biomass particles inside the bed. Unlike common practice, herein black background colour refers to high gas volume fractions while grey colour refers to low gas volume fractions. Bed conditions: u_0=0.76m/s, X_{H_2O}=7.0%, T=758K

little tar formation. The local tar formation agrees well with findings in Figure 5.15 where the injection area is cold and not easy to access by partially depleted biomass particles. The main local tar formation takes place in near-wall areas - except for the injection area to the left. When bubbles burst at the bed surface, they preferably rise in the middle of the bed, pushing bed particles towards the walls. In Z-direction, a vigorous bubbling bed shows always higher particle volume fractions at the bottom (averaged over time) and therefore tar is predominantly released in such areas. For a strongly segregated biomass phase as in the first case of Figure 5.11, the tar formation profile in Z-direction displays a sharp spike indicating less efficient mixing and distinct segregation.

Biomass particles reaching a maximum temperature level after slightly more than one second after injection as shown in Figure 5.16. Later in time temperature reduces due to the applied reaction heat given in Table 5.2. The heat transfer coefficient is derived from the Nusselt number given in eq. (5.13) and gives very

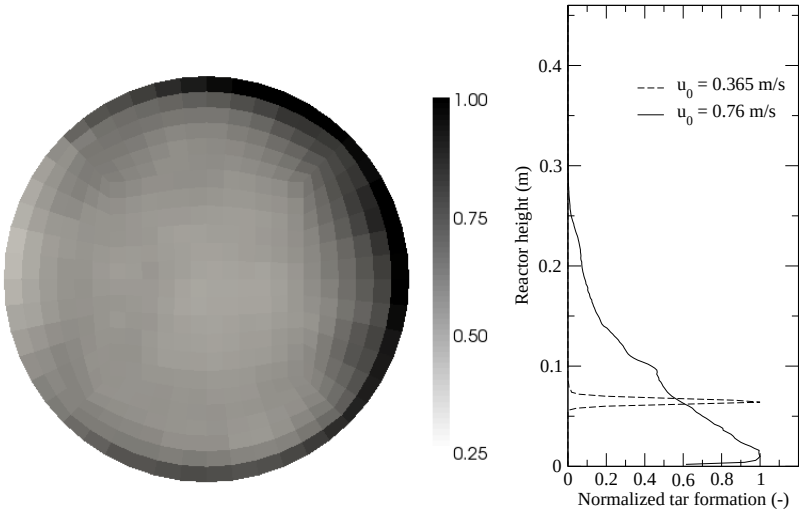

FIGURE 5.15: Left: spatial tar formation in X-Y plane, where each cell value represents the sum of all cells in Z-direction (reactor height) divided by the maximum value found in the X-Y plane (normalised) for $u_0 = 0.76$ m/s and right: normalised spatial tar formation in Z-direction (reactor height).

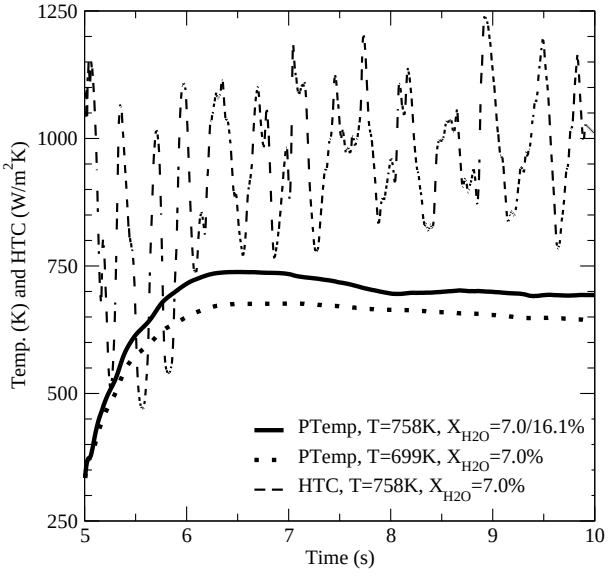

FIGURE 5.16: Particle temperature and convective heat transfer coefficient averaged over one batch of particles (318 particles). Other conditions: u_0=0.76m/s

high values around 1000W/m^{2}K. The heat transfer coefficient rises slightly due to particle shrinkage.

Table 5.5 compares simulation results with experimental data obtained from the Iowa State University 100g/h pyrolyser. The tar fraction in experiments contains water and the condensed vapour fraction while the simulation distinguishes between the water which originates from the drying process only and the condensed vapour fraction (tar) which includes water generated during the degradation process at elevated temperatures. Simulation results after 5 seconds of real time

indicate a slightly overprediction of water and/or tar and underpredict the char yield in all three test cases when compared to experimental steady-state results. The second (758K, X_{H_2O}=7.0%) and third (699K, X_{H_2O}=7.0%) run produce the same absolute amount of water at the outlet due to the same moisture content and feeding rate applied. This indicates that the second run produces more than twice the amount of tar, gas and char together than the third one. Figure 5.12 indicates that this is possible although for a fully steady-state process the ratio would reduce and more char would be created. In other words, in the first five seconds biomass is not entirely converted and the remaining X_{Wood} portion contains mainly lignin which preferably turns into char, however the relative water content would reduce. Similarly, the first run (758K, X_{H_2O}=16.1%) produces more than twice the amount of water compared to the second run and both undergo similar conversion during pyrolysis. Therefore, a very good agreement between experimental and simulation results has been obtained. It has to be kept in mind, that simulation results are not obtained at the outlet, they are monitored as the sum of all biomass particle source terms in the simulation.

It is difficult to determine the product yield directly at the outlet as char particles leave the reactor erratically and it seems that steady-state particle entrainment is reached far later than water, tar and gas yields. Because only shrinkage is considered in this simulation work, it is believed that far more tiny char particles leave the reactor being created additionally by breakage and attrition. To perform simulations in a reasonable time period, a further reduction in particle size is prohibited. Figure 5.17 illustrates the gas composition at the outlet which matches very well with steady-state experimental data from Table 5.5. According to Figure 5.17 steady-state is reached for water. A steady-state tar and gas mass flow rate is only approximately achieved after 2.5 seconds as the number of biomass particles still grow and most of them only deplete slightly after 2.5 seconds after injection (Figure 5.12).

5.2.2.4 Entrainment of Particles

The function of the freeboard above a fluidised bed is to disengage gas and particles. Particles which fall back into the bed can only reach a maximum height above the bed (transport disengagement height - TDH) as their terminal velocity u_t is larger than the fluidisation velocity u_0. In case of entrainment during fast pyrolysis, particles are harmful as char contains inorganics (ash) which causes fouling, corrosion, erosion and plugging of orifices [189]. Consequently, there is an

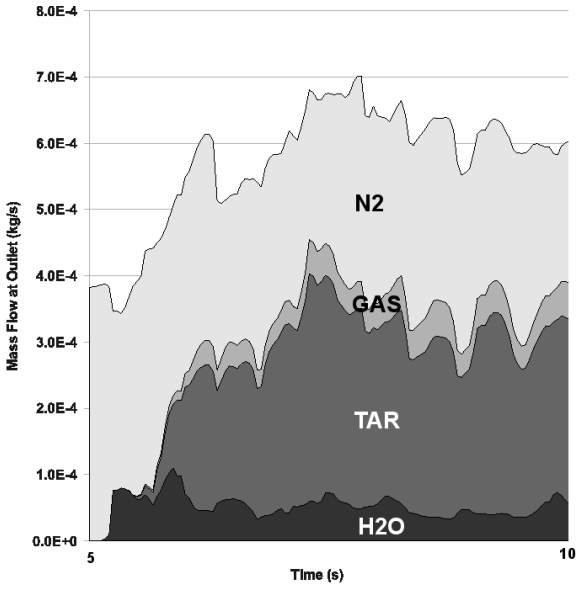

FIGURE 5.17: Gas composition at the reactor outlet obtained from the simulation. Lighter non-condensible gases such as CO_2, CO, H_2 and CH_4 are summarised as GAS. Tar might also include a smaller water fraction. Other conditions: u_0=0.76m/s, X_{H_2O}=7.0%, T=758K

optimum reactor height - short enough to reduce the residence time of tar but tall enough to reduce particulates in bio-oil and post-processing equipments (cyclones, filters, condensers).

Table 5.3 contains the superficial velocity used and the terminal velocity associated to different particles in this work. It can be seen that the terminal velocity is always higher than the superficial fluidisation velocity. Although no particle entrainment has been encountered in the faintly bubbling fluidised bed model for the first 5 seconds of fast pyrolysis operation, entrainment becomes important in the vigorous bubbling stage as the TDH becomes greater than the actual reactor height. Due to different and unaccounted physical multiphase flow conditions in the freeboard, there is considerable quantitative disagreement between estimated TDHs, entrainment rates etc. [1, 136, 190]. TDH values can be calculated for the 100g/h small-scale fluidised bed reactor with an inlet flow rate of 52/25 l/min from Baron et al. [136] (TDH=3.94m/1.74m), Horio et al. [191] (both TDH=3.33m) or Smolders et al. [192] (TDH=1.98m/1.08m). All of these calculated values are not dependent on particle properties and do not consider effects of a slugging regime ($d_B > D/3$) or multi-modal particle composition in very small lab-scale reactors. Despite of the uncertainty of calculated TDHs, theoretical expectations and experimental results confirm the qualitative entrainment behaviour modelled in this work.

The vigorous bubbling bed is characterised by its large bubble development and its intensive bubble eruptions by which light particles often reach the upper freeboard area where they are eventually entrained. Figure 5.18 captures three different moments prior to entrainment of several large particles. The left figure illustrates a huge bubble formation at the bottom - probably one of the key prerequisites to obtain high velocities necessary for entrainment. Four particles are highlighted which are going to be entrained. All originate from different locations. Later in time, the upper three particles come very close together on the bubble dome and will be entrained similarly. In slugging beds, it is expected that mainly roof solids are thrown into the freeboard while wake particles are not [1]. The fourth lower particle gains height by ending up in the middle of the bubble where it has been accelerated by the fast upward moving gas flow. These gas velocities can easily approach 4 m/s locally when operating the bed with a superficial velocity of 0.76 m/s only.

Before entrainment occurs, most particles change their direction due to collisions just above or near the top of the bed. They can experience even negative Z-velocities as long as they are repositioned (by collisions) into a fast upward moving gas stream (originating from a big bubble). Numerous potential collision partners are available in the lower freeboard region while the particle concentration reduces exponentially [190] with the freeboard height. Hundreds of entrained particles have been looked at throughout this work having in common that they are positioned rather in the middle of the X-Y plane and do not collide on its recent path before leaving the reactor. The upper freeboard usually displays a very flat and characteristic rather laminar Hagen-Poiseuille flow profile in which particles experience very low relative velocities regardless of their current location. In case of collisions, particles are more likely to change their directions and finally fall back (preferably near the wall) into the bed. Figure 5.18 shows 30 trajectories of particles which are entrained in the same time-window between 8.60 and 8.70 seconds of reactor operation.

After 5 seconds of first biomass injection into the fluidised bed (second case in Table 5.5) the following information can be obtained from the simulation. A total number of 188781 biomass particles remain in the reactor while only 429 particles have left the reactor through the outlet. Based on the first batch of 318 biomass particles, only 8 particles have left the reactor. Figure 5.19 illustrates the Z-velocity of entrained particles. It can be seen that particles are getting entrained periodically in clusters depending on the eruption of very large bubbles. Although the hydrodynamic behaviour is similar between the second and third

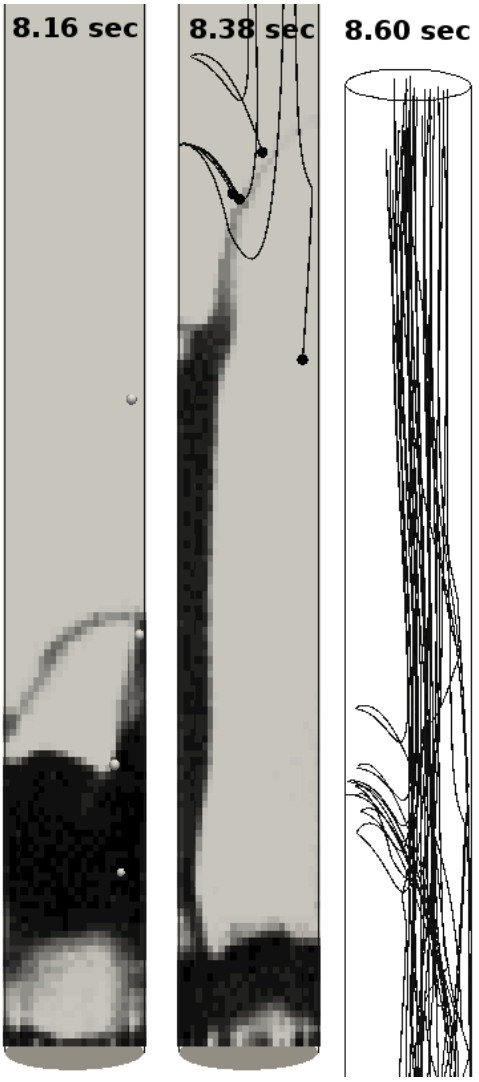

FIGURE 5.18: Four selected biomass particles and their way through the reactor inside the dense bubbling sand bed which are going to be entrained later in time (at ≈8.60 seconds). The right figure shows numerous particle trajectories which are entrained approximately at the same time.

case, entrainment results are different. In the third run, the conversion of particles to lower densities takes much longer (Figure 5.12) and entrainment of higher density biomass has hardly been observed throughout any simulation. All particles entrained in the third simulation case have a higher average density and have been entrained almost at the same time originating from one large bubble. For the second case, the composition of entrained individual particles are summarised in Figure 5.20. The remaining wood fraction can be associated with mainly lignin which slowly reacts in time representing roughly 20% of the original particle mass. This fraction slightly reduces in time which indicates that steady-state has not been reached completely. The char and tar mass fraction grow slightly accordingly. These results indicate that the majority of entrained particles are expected

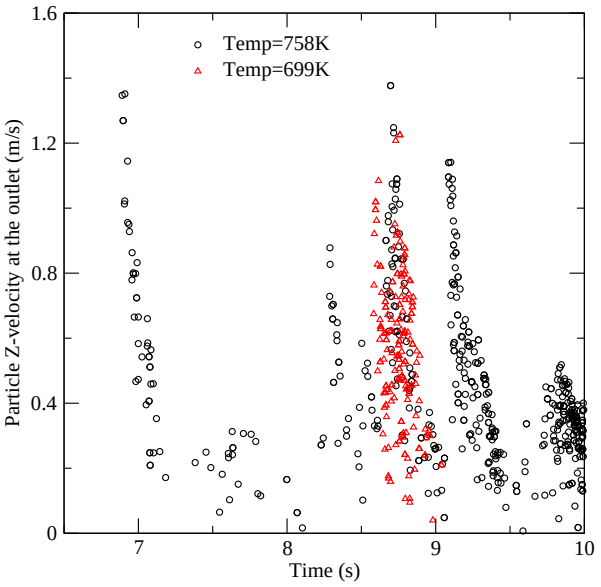

FIGURE 5.19: Z-velocity of entrained particles at the outlet of the reactor. Other conditions: u_0=0.76m/s, X_{H_2O}=7.0%

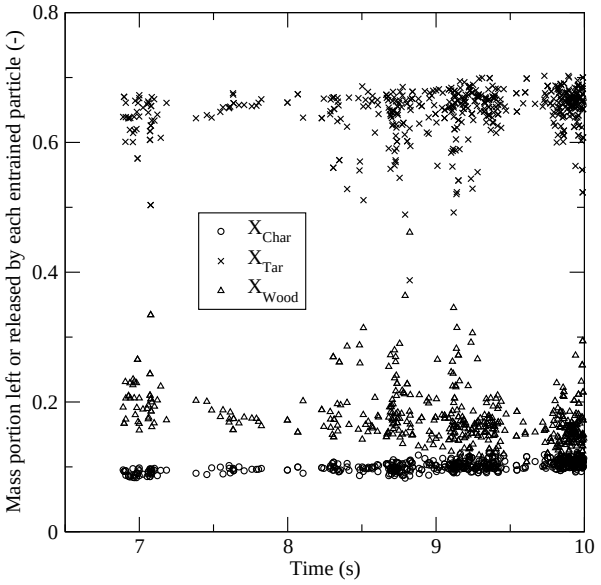

FIGURE 5.20: Remaining wood and char fraction of entrained particles and the released tar yield fraction based on the initial wood mass. The fraction of released non-condensible gases is not shown. Other conditions: u_0=0.76m/s, X_{H_2O}=7.0%, T=758K

to have a similar yield fraction.

5.3 Conclusions

Single, thermally thick, stationary particle thermochemical degradation modelling using a reaction scheme with competing pathways proposed by Shafizadeh and Chin [163] has been performed. It has been found that not many kinetic data are available from the literature to describe primary wood pyrolysis. Furthermore, the thermally thick approach is not useful without modelling convective gas transport inside the particle to capture secondary tar reactions. By using the zero-dimensional thermally thin approach, simulations are less demanding and more applicable for numerous biomass degradation studies.

A CFD-DEM model has been presented which is able to model the thermochemical degradation of biomass inside a lab-scale bubbling fluidised bed reactor containing roughly 0.8 million particles. The model treats all particles as spherical discrete elements where each is associated with a range of physical and material properties. This allows detailed investigations at different scale levels with high precision. Collisions, chemical reactions, fluid- and thermodynamic interactions are solved during biomass depletion and shrinkage. Such sophistication allows to study fast pyrolysis from a novel perspective, and to raise the level of understanding. The model has been validated with experimental data.

First, bed hydrodynamics have been modelled depending on different inlet distributor plates at the bottom of the bed. Only small changes in the motion of bed particles have been recognised without changing the particle volume fraction much and it is strongly believed that this has hardly any effect (in the reactor studied) on the final pyrolysis yield composition. Therefore, modelling pyrolysis under plug-flow conditions in slugging beds should not result in erroneous predictions.

It has been found that the fluidisation velocity is a very important parameter which affects mixing and in turn heat transfer to particles. The fluidisation velocity should not be chosen close to the minimum fluidisation velocity to avoid segregation and small bio-oil yield fractions. Two cases with different bed temperatures have been compared where secondary tar reactions are not important. In agreement with the literature [104, 105], it has been shown that the bed temperature strongly affects the yield composition - obtaining generally a good yield around 750K. Simulations undertaken in the scope of this work indicate that the biomass moisture content has hardly any effect on the pyrolysis process itself but does affect the water content in the final oil fraction. The product yields obtained in experiments and simulations are in good agreement for all conditions tested.

Taking into account an expected slight increase in char and a slightly smaller water content for a steady-state result, both experiments and simulations would be in even better agreement.

Although particle entrainment results are far from being steady-state, the main characteristics of the entrainment process have been studied. Generally it is assumed, that particles in the bed are splashed into the freeboard when bubbles burst at the surface [107]. However, in this lab-scale fluidised bed model, it has been observed that the size of the bubble determines the fast upward moving gas stream responsible for carrying the particles up to the reactor outlet. Rather free moving particles positioned at the bubble dome or inside the bubble itself are more likely to be entrained. No entrained particles originate from the bubble wake. Entrained particles leave the reactor periodically in small clusters.

The 3D simulations undertaken are able to reliably reproduce overall conditions encountered in experiments and deliver a powerful tool to understand and examine local and global effects and aspects relevant to further optimise these complex processes.

All simulations were run on the HECToR Phase 2a system (2.3GHz, 48 nodes with 4 cores each). The first 5 seconds real time to obtain a stable fluidisation behaviour with only sand inside the reactor required 80,000 CPU hours. After biomass feeding has started, simulation times went up with increasing progression of the simulation. For the other remaining 5 seconds of real time of biomass feeding into the bubbling bed required another 320,000 CPU hours. The simulation with the lower bed temperature took about 300,000 CPU hours due to less depleted biomass particles.

Chapter 6

Fragmentation of Brittle Particles

A novel discrete fragmentation method (DFM) for spherical brittle particles using the discrete element method (DEM) has been developed, implemented and validated. Trajectories of individual fragments can be studied from the moment of breakage where the progeny might originate from incremental, simultaneous and/or repetitive fragmentation events. The onset of fragmentation is modelled by using a breakage probability which considers incremental impact breakage by summation of accumulated damage. In principle, this model can be provided with any particle size distribution (PSD) - however, a breakage index t_{10} - a single value to determine the entire PSD has been used. This approach offers several advantages over others as it depends on material parameters only. Furthermore, it has been proven to be valid for multiple impact breakage and for many brittle materials. Discrete fragments are created depending on the given PSD and packed randomly into their parent particle volume with a minimum child-child particle overlap. Mass, momentum and energy is conserved during breakage. Each fragment is assigned with a kinetic (velocity) component derived from the momentum conservation and an elastic (spring force) component derived from the energy equation. A theoretically consistent description of the fragmentation and particle cloud formation process has been developed. Using a particle size distribution sub-model based on the assumption of a t_{10} distribution, the predicted PSD is in good agreement with experimental data for the PSD resulting from fragmentation of plaster balls. All material parameters have been varied independently to study the sensitivity of the model under dynamic fragmentation of numerous particles in a semi-autogenous (SAG) mill. SAG mills are essentially autogenous mills, but using grinding (mostly steel) balls to aid in grinding like in a ball mill. Autogenous mills are so called due to their self-grinding process of ore inside a rotating drum.

6.1 Fragmentation model theory

This section provides a description of the discrete fragmentation model and discusses the theory used.

6.1.1 Onset of fragmentation

When collision forces acting on a particle, the particle initially deforms elastically and it absorbs impact energy as elastic strain energy [193]. According to the Griffith criterion [194], stresses inside the particle grow further until the critical stress of the most sensitive flaw is reached. This critical stress level is strongly related to the mass specific threshold energy $W_{m,min}$ to further damage a particle. Because there is evidence of a continuous transition for most materials between a fractured (damaged) and a fragmented state [195–197], particle damage is incremented when the specific impact energy rises beyond $W_{m,min}$. Fracture begins at one of a number of weak spots at the surface of the particle known as the Griffith cracks [198] where the particle suffers from surface breakage. Whenever the destroyed fraction of the particle or the probability of breakage P is high enough, body breakage (cleavage or shattering depending on the impact energy) will occur [199].

Not many approaches are able to model the onset of fragmentation considering the particle damage history on the basis of purely material parameters. Vogel and Peukert [200] introduced a probability function for comminution based on two aspects. It has been derived first from a similarity of breakage of particles of similar shape but different materials and second a mechanical fracture model for comminution. Herein, the probability of breakage P is computed as

$$P = 1 - \exp\left[-f_{Mat}\ d\ k\ \ (W_m - W_{m,min})\right], \tag{6.1}$$

where $W_{m,min}$ is the mass specific threshold energy which a particle can absorb without fracture, k is the number of stress events with a constant mass specific impact energy W_m, f_{Mat} is a material parameter characterising the resistance of particulate matter against fracture and d is the particle diameter. The product $(d\ W_m)$ is size independent as shown by Vogel et al. [200].

For DEM applications, eq. (6.1) can be modified to eq. (6.2) as the accumulated damage and the resultant probability of breakage after a number of impacts of

different specific impact energies E_i are of interest [201].

$$P = 1 - \exp\left[-f_{Mat}\ d\ \sum_i (E_i - E_0)\right] \tag{6.2}$$

In experiments, E_0 is defined as the energy at which the probability of breakage in an infinite number of hits is below 5% [24] and should be at least approximately equivalent to $W_{m,min}$ [201]. In this work, the product $f_{Mat}d$ is used following the notation of Vogel et al. [200, 202] which has the advantage that different particle sizes (incremental fragmentation) can be modelled by specifying one single material parameter f_{Mat}. However, the disadvantage is that f_{Mat} is more difficult to obtain. One way has been described by Vogel et al. [200] and the other way is by approximation of the following equation: $b \approx f_{Mat}d$. The value b is the Julius Kruttschnitt (JK) standard "slope" parameter determined experimentally in drop weight tests. Material values for f_{Mat} and (d E_0) can be found for rock [203] or polymers, glass and limestone [202]. Napier et al. [204, chap.5] provide more details on how to measure the comminution specific material parameters A (see next section), b and E_0.

6.1.2 Size distribution and number of fragments

The resulting stress field inside particles depends on the nature of loading, the deformation behaviour, the particle shape and their structural inhomogeneities which precede the breakage event. Because of this complexity, no generally valid function can be found to describe the progeny PSD (particle size distribution) [205]. A number of mathematical functions have been proven to be useful to obtain a correct PSD for specific applications. The most common ones are the Rosin-Rammler and the Gaudin-Schuhmann / Gaudin-Meloy (power-law) distributions all are two parameter equations purely empirical in nature. Three parameter equations are introduced to improve curve fittings [206, 207] and other authors [208–210] have shown that repetitive fracture approaches a logarithmic-normal size distribution. All these functions have in common, that they do not depend on physical particle or material properties. Gilvarry [211] introduced a size distribution law for single fracture which incorporates flaw densities inside the particle. Fractures begin at structural flaws but do not solely depend on them. Shi et al. [212] modified Vogel and Peukert's breakage probability model to compute the breakage index t_{10} as shown in eq. (6.3) depending on material properties, particle size and cumulative

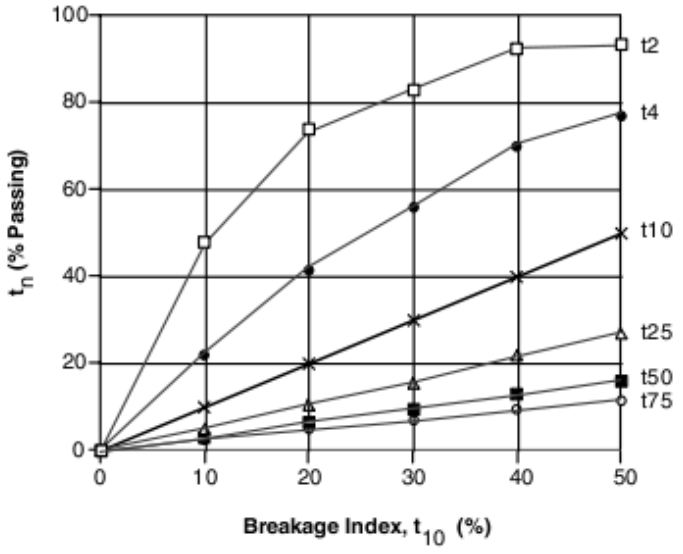

FIGURE 6.1: Determination of other size distribution parameters t_n from the breakage index t_{10} [213]

impact energy for comminution processes.

$$t_{10} = A \left\{ 1 - \exp \left[-f_{Mat} \; d \; \sum_i (E_i - E_0) \right] \right\} \tag{6.3}$$

The breakage index t_{10} is the cumulative mass percentage of the progeny which passes 1/10 of the parent particle diameter and A is the maximum achievable t_{10} in a single breakage event and ranges from zero (cleavage into a few number of fragments) to 50 (attrition-like fragmentation). Once t_{10} is known, it is uniquely related to a family of PSD curves, t_n, plotted in Figure 6.1 [213]. This correlation has been proven to be robust across several thousand drop weight tests based on many brittle materials and a wide range of hardness [201]. It has been used in this model to obtain the cumulative mass fraction of fragments t_n, passing a given size fraction d/n of the initial parent particle size d. With the help of spline regression analysis, the whole progeny PSD can be obtained (details see [212,214]), based on the single breakage index t_{10}. Although any other function can be used to model the progeny PSD, the advantage of the t_{10}-approach is its applicability to multiple impact breakage [201] and its validity for many brittle materials [201].

When the PSD is known, discrete fragments of different diameters are generated. To do so, a virtual size starting from the parent particle diameter is multiplied by a value of 0.999 as often as it is required to match the mass of a new fragment (given by its diameter) and the remaining cumulative mass percent given by the size

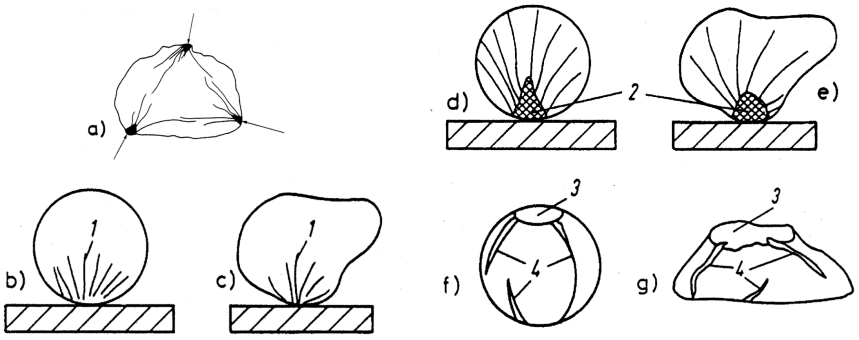

FIGURE 6.2: Crack pattern a) under multiple forces, b/c) crack rays and d/e) destroyed cones in elastic and f/g) cracks in plastic material [205]

distribution curve. This procedure continues until a minimum fragment diameter d_{min} is reached. The specified minimum fragment diameter in this model is very important for the resulting total number of fragments and is required to avoid numerical instability and sustain the efficiency of simulations. When the model stops at the specified minimum diameter, there is still some mass which would belong to smaller fragments. The accumulated mass of all tiny fragments (smaller than d_{min}) is used to generate one single fragment which violates against a correct size distribution aforementioned but accounting for a correct mass balance. This can be changed if desired.

6.1.3 Spatial distribution of fragments

Fractures in spheres approximately follow principal stress pattern depending on whether elastic or plastic deformation occurs. The deformation behaviour depends on many parameters like the material, size, stress level and temperature. The quicker the rate of stressing, the bigger the particle size and the lower the temperature, the shorter is the plastic stage and the faster the material becomes brittle. As indicated by Jaeger [215], cracks develop from one force contact point towards another force contact point (Figure 6.2a). During impact loading of purely elastic spheres, fractures propagate like rays (1) from the impact point (Figure 6.2b and 6.2c). As the theory shows, the cone region inside the sphere at the impact point possesses the highest energy density before fracture and when it is released it results in the production of mainly fine material (Figure 6.2d and 6.2e). In contrast to elastic breakage, the cone at the impact point inside plastic particles remain undestroyed, pushing orange-like slights away from the centre, initially leading to meridional fracture patterns (Figures 6.2f and 6.2g) [216].

Crack formation patterns deliver important information about the spatial distribution of fragments. Unfortunately, even elastic brittle material seldomly shows a purely elastic deformation behaviour. The simulation time is strongly dependent on the particle diameter and might increase rapidly if too many tiny fragments are considered. Furthermore, all fragments are restricted to be spherical in shape. This means an accurate prediction for a realistic spatial distribution of fragments is difficult. Compared to finite element models and other agglomerate DEM models applied to fragmentation, the present model considers only incremental damage but does not resolve flaws or cracks inside the particle to maintain efficiency and applicability for models considering numerous particles. Therefore a random distribution of fragments has been chosen. Fragments are inserted into the parent particle volume eventually with unacceptable mutual overlaps (e.g. 100%) but no overlaps with outer boundaries (walls or other parent particles). A minute spatial displacement of individual fragments is then suggested randomly (if needed several times) to remove these unacceptable mutual overlaps and to achieve highest code stability. This is achieved by proposing a random but maximum fragment displacement distance of half the fragment's radius in each direction where no overlaps with walls or the parent particle surface are allowed. Once a valid possible fragment displacement is found, the displacement is checked again whether it increases the mutual fragment distance with all neighboring fragments. The desired number to reposition fragments inside one parent particle has to be chosen a priory.

6.1.4 Momentum and energy conservation during fragmentation

During fragmentation, kinetic energy of the parent particle is transformed as fragments are halted by contact with the surroundings, destroying fragment momentum and generating forces on the surroundings [217]. Momentum of the parent particle goes also partially into the extention of cracks so that the momentum of child particles after breakage should be smaller than the initial parent particle momentum. In this work, a momentum factor e_F is proposed, which is used only once at the moment of breakage and can be thought of as a coefficient of restitution for fragmentation as:

$$e_F = -\frac{u_{cp,ab}}{u_{pp,bi}}, \tag{6.4}$$

where $u_{cp,ab}$ is the child particle velocity after breakage (and all fragments have the same velocity at this stage - as clarified below) and $u_{pp,bi}$ is the parent particle velocity before impact. The momentum equation in the normal impact direction for a parent particle can be written as:

$$u_{pp,bi}\ m_{pp} \quad = \quad -\left[m_{pp}u_{pp,b} + \sum_{col}\int F\ dt\right], \tag{6.5}$$

where the left hand side is the momentum before impact and the right hand side is the momentum at the moment of breakage, which accounts for the kinetic and elastic part. By dividing eq. (6.5) by the parent particle mass m_{pp} and by putting this equation into eq. (6.4), an expression for the child particle velocity (first velocity component) is obtained:

$$u_{cp,ab} = e_F\left[u_{pp,b} + \sum_{col}\int \frac{F}{m_{pp}}\ dt\right]. \tag{6.6}$$

At the moment of breakage, the force to trigger fragmentation has passed its culmination so that the sign of the parent particle velocity $u_{pp,b}$ is always the same as that of $u_{cp,ab}$.

The integral over the remaining virtual collision time is approximated by linearisation in eq. (6.7).

$$\int \vec{F}\ dt = \vec{F}_1\Delta t + \vec{F}_2\Delta t + \ldots \tag{6.7}$$

Each individual force $\vec{F}_1, \vec{F}_2, ...$ is computed from $\vec{F}_{en}$ in Table 3.1 and the appropriate overlap distance $\delta_1, \delta_2, ...$ which is reduced according to eq. (6.8) as often as it would be needed for the parent particle to rebound unhindered from the external contact body (to convert impulse into momentum).

$$\delta_n = \delta_{n-1} - \Delta\delta = \delta_{n-1} - \left[\frac{\sqrt{\sum\limits_{x,y,z} F^2}}{m_{pp}}\Delta t^2 + u\Delta t\right] \tag{6.8}$$

Here, Δt is the particle time step used and u is the velocity of the colliding parent particle starting from zero. The subscript n refers to the integer number of the integration time-step, where $n = 1$ refers to the first time-step. The integral is solved, when the remaining δ_n from eq. (6.8) becomes zero. It should be pointed out, that each fragment's momentum is a mass weighted portion of the overall momentum leading to a minimum kinetic energy of the fragments. At this stage,

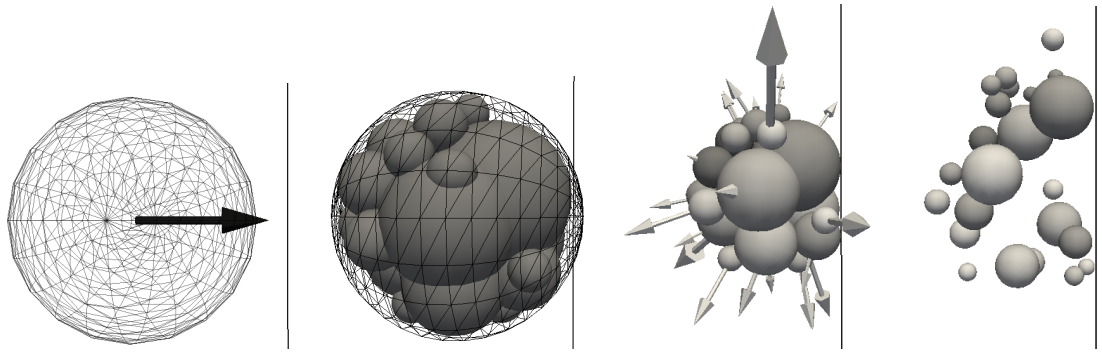

FIGURE 6.3: (a) A brittle particle moves towards a wall, (b) when the maximum elastic energy is reached (see overlap with the wall) and it comes to fragmentation, the parent particle is replaced by child particles which do not touch the wall (c) arrows indicate the direction and particles are coloured by their velocity (black=slow, white=fast) (d) pictures the progeny after fragmentation

the velocity of each fragment in eq. (6.6) is the same but will change when elastic forces on each fragment are considered (artificial overlaps between fragments due to fragmentation as shown in Figure 6.3b).

Collisions between child particles are considered as internal forces which do not change the total linear momentum of a system. Child particle collisions with the wall or other parent particles (external forces) do not exist (Figure 6.3b) at the moment of fragmentation as all fragments are inserted without external overlap. Conservation of angular momentum is not considered in the present model, as fragments might experience high shear forces between them.

Artificial overlaps between child particles need to be corrected in terms of their associated elastic energy. The artificial overlap between child particles at the moment of fragmentation is remembered in δ_{rem} and a dimensionless collision factor CF is applied to correct the associated artificial elastic energy. At each particle time step, δ_{rem} is updated according to $\delta_{rem} = MIN(\delta_{rem}, \delta)$ as long as the collision is found in the collision list (the collision exists). Eq. (6.11) is introduced to obtain CF by taking the energy balance eq. (6.9) into account.

$$E_{pp,kin} + \sum_{col} E_{pp,el} = \sum_{j} E_{cp,kin,j} + \sum_{col} E'_{cp,el} + E_{diss} \tag{6.9}$$

$$E'_{cp,el} = \frac{2}{5} k_n (\delta^*_{ar})^{5/2} CF = E^*_{cp,el} CF \tag{6.10}$$

$$\begin{aligned} CF &= \left[\frac{\delta'_{ar}}{\delta^*_{ar}}\right]^{3/2} \\ &= \frac{E_{pp,kin} + \sum_{col} E_{pp,el} - \sum_{j} E_{cp,kin,j}}{\sum_{col} E^*_{cp,el}} \end{aligned} \tag{6.11}$$

The asterisk indicates geometrically correct but not energetically correct values, the dash indicates energetically correct but geometrically incorrect values after replacement (ar) and j is a counter variable for the fragments. Eq. (6.10) is only used once during the breakage event so that the damping force does not need to be considered separately as it is already taken into account in the CF value and in turn in e_F. For $CF = 1$, eq. (6.10) is the integration of the elastic normal force $F_{en} = -k_n\delta^{3/2}$ (Table 3.1) and corresponds to the elastic energy for the Hertzian contact theory. The elastic energy stored by the parent particle until the instance of fracture (second term in eq. (6.9) is the well known particle fracture energy [218]. The CF value is the same for all fragment collisions created by the same broken parent particle and acts within $\delta \leq \delta_{rem}$ only, CF is set to unity otherwise.

The total energy required for fragmentation is often more than 100 times larger than the energy required to produce new surface and which finally might get dissipated. Stretching and disruption of intermolecular force fields require work to be done where almost all of this is recovered as kinetic energy when the force fields separate and return to their unstressed states [219]. For that reason, the term E_{diss} can be assumed to be small for most materials and should be considered for future studies as long as a reliable theory is provided.

6.2 Results and discussion

This section discusses the results from the discrete fragmentation model. The onset of fragmentation, the size distribution of fragments and the energy and momentum distribution after the moment of breakage are particularly analysed and as far as possible validated with available data.

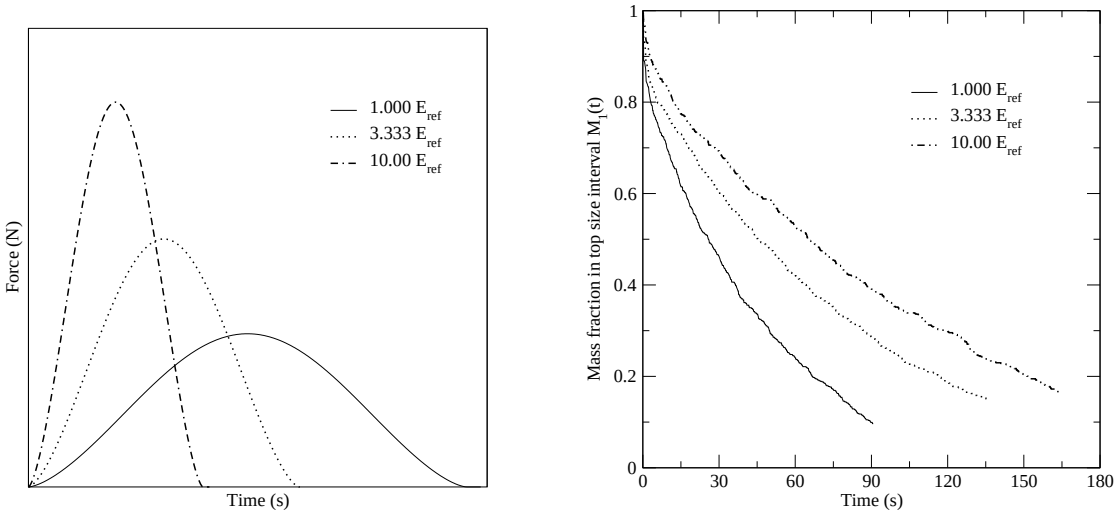

FIGURE 6.4: (a) Forces acting between a wall and a recoiling ball at normal incidence for different Young's moduli and (b) the breakage behaviour inside the SAG-mill for the same particle stiffness

TABLE 6.1: Particle property settings

Variable	Value	Units
$f_{Mat,ref}$	0.9	kg/Jm
$(d \cdot E_0)_{ref}$	0.15	Jm/kg
A_{ref}	10	–
d_{min}	0.0125	m
e_F	0.485	–
e	0.97	–
μ	0.1	–
$E_{w,ref}$	10^{+8}	N/m^2
$E_{p,ref}$	10^{+7}	N/m^2
ν	0.25	–
d_{ball}	0.1	m
$d_{charge,init}$	0.05	m

6.2.1 Onset of fragmentation

In order to model reliably the onset of fragmentation under consideration of incremental damage and to some extend the dependency of an arbitrary process, model results need to be averaged over many fragmentation events. To discuss model parameters and their influence on the onset of fragmentation (the frequency of breakage) an application is required which can be modelled for a decent period of time and considers a large number of particles. Herein, a semi-autogenous mill has been chosen.

Semi-autogenous mills are loaded with large heavy balls and small charge particles which suppose to be crushed by the balls. The geometric mill data are taken from [48], with an initial mill diameter of 1.19m and a length of 0.31m fitted with 14 metal lifters each 40 mm in hight. The rotating speed is 70 % of its critical speed[1] (3.14 rad/s). For each simulation, 24 large balls ($\rho = 6500kg/m^3$ and $d = 0.1m$) and 714 charge particles ($\rho = 2650kg/m^3$ and $d = 0.05m$) are loaded and ground in batch mode. Particle collision properties (E_p, E_w, ν, μ, e) are required in soft-sphere DEM models [30]. Both, small charge particles and the heavy balls do not represent a specific known material, they are assumed to have the same collision properties. Breakage properties are chosen in the range of existing very brittle materials but also under consideration of computational feasibility, so that their values are rather fictitious than related to an exact specific material. Note that E_0 is not constant and is the energy needed to damage a particle. Different sizes of particles require different impact energy to be damaged. The mill under discussion uses different particle sizes and therefore cannot use a constant E_0. However, according to Vogel and Peukert [200], the value of $(d \cdot E_0)$ is size independent and that's why a constant value of $(d \cdot E_0)$ has been chosen. All breakage and collision parameters have been summarised in Table 6.1, where reference values have been kept constant except otherwise stated. The dissipative nature of the material has been considered by specifying the momentum factor in eq. (6.4) to be $e_F = 0.485$ and the dissipated energy is chosen to be negligible in eq. (6.9) ($E_{diss} = 0$). Industrial to lab-scale applications often produce millions of particles down to sizes of microns. DEM models cannot solve such problems within a reasonable computational time so that simplifications are required - herein, only the large particle fraction is considered ($d_{min} = 0.0125m$). Charge particles are grouped into different bin sizes named as M_1, M_2,... which have been kept within the $\sqrt{2}$ sequence ($d_{min,n} = \sqrt{2}d_{min,n+1}$, where n is the number of the bin). In this study, particularly the mass reduction of particles in the top size (original size) of $d_{min,1} = 0.05m$ (M_1) is of interest as other size classes depend simultaneously on a created and reduced fraction.

Soft-sphere DEM models in general and their results rely on the particle stiffness (Young's modulus and Poisson ratio) and so does the DFM model. Figure 6.4a shows the force acting between a rebounding ball hitting a wall at normal incidence - indicating that for a softer material the contact will last longer with a smaller force magnitude. The same stiffness values have been used for grinding particles inside a semi-autogenous mill as depicted in Figure 6.4b, showing that the softer

[1] $N_c = 76.6\left(D^{-0.5}\right)$, where N_c is the critical speed in rad/min and D is the effective inside mill diameter in feed [220].

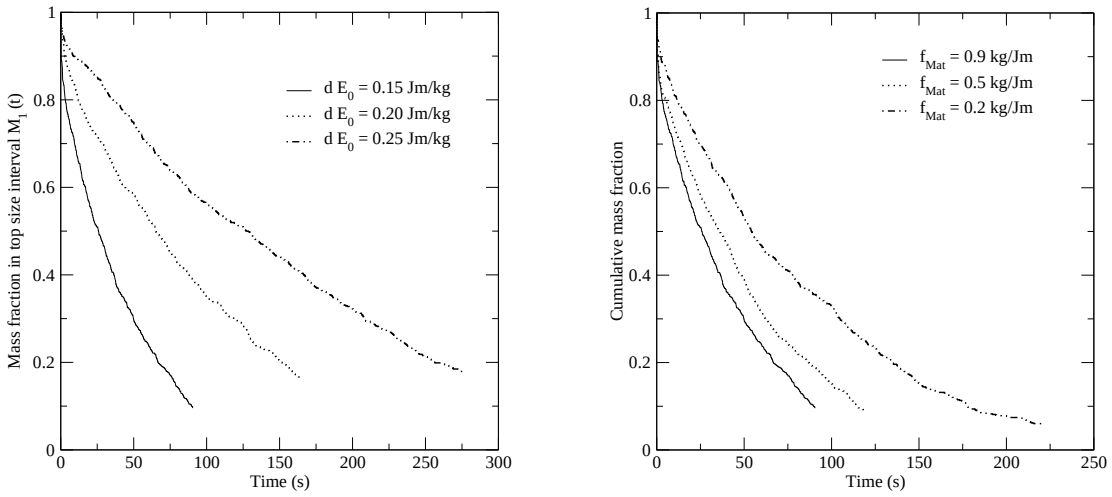

FIGURE 6.5: (a) Grinding times for different values of ($d\ E_0$) (threshold energy to achieve damage) and (b) different f_{Mat} values and their influence on the breakage frequency / grinding time and cumulative mass fractions of charge particles in other bins

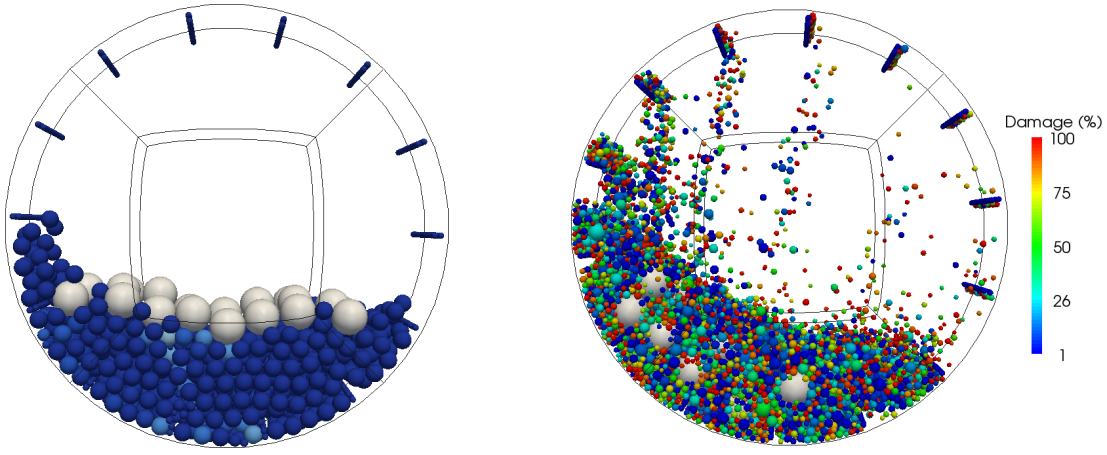

FIGURE 6.6: Damage of charge particles inside a SAG-mill just after the start (left) and when most (>95%) particles from the original size have been broken at least once (right), white balls are responsible for breaking charge particles and do not break

the material (the lower E) the higher the breakage frequency. This is because the time-scale to allow fragmentation is much longer. However, for single impacts, the onset of fragmentation is independent of the particle stiffness (one single request to trigger fragmentation). For particle agglomerates, one particle impact is likely to be disturbed by other particle forces so that multiple force maxima emerge (multiple requests to trigger fragmentation). This phenomenon might lead to incorrect predictions in some particular cases. The key point is the definition of the duration which is considered as one single impact, because theoretically in the same duration many maxima can be reached (e.g. vibration) to cause a wrong

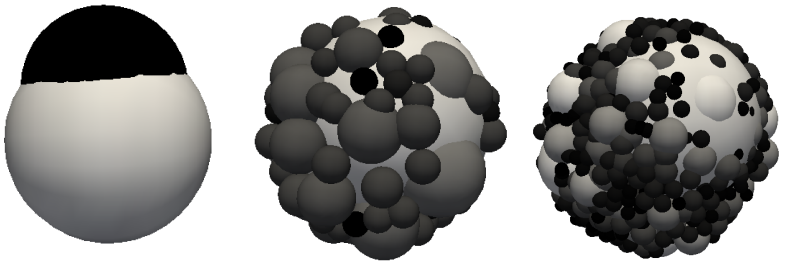

FIGURE 6.7: Fragments created under a constant probability of breakage P ($d_{pp} = 0.2m$) when (a) $A = 0.0$, $d_{min} = 0.02m$ (b) $A = 50.0$, $d_{min} = 0.02m$ and (c) $A = 0.0$, $d_{min} = 0.01m$

model prediction. All settings for the DFM model which have not been modified are summarised in Table 6.1 except otherwise stated.

Next to the particle stiffness, the material parameter f_{Mat}, the mass specific threshold energy E_0 and the particle size d do influence the onset of fragmentation according to eq. (6.2). Vogel et al. [200] indicated that the product $d\ E_0$ is constant for all particle sizes, also used in the present model as a single setting parameter so that its influence is tested and shown in Figure 6.5a. As a rough estimate, its dependency can be assumed to be linear with the required grinding time. The higher the threshold for damaging particles the lower the breakage frequency. The influence of the material parameters f_{Mat} is depicted in Figure 6.5b. The fracture material parameter f_{Mat} is inversely dependent on the well known fracture toughness K_{IC}, so that smaller values for f_{Mat} causing longer grinding times.

Figure 6.6 shows the particles inside the semi-autogenous mill right after the start and at the end of a grinding process. The big white balls are not damaged at all while smaller particles from the charge are coloured according to their degree of damage. Particles from the smallest bin are not allowed to break further as they are restricted by d_{min}, so that their damage might reach 100%. This leads to misinterpretation and needs to be changed in future studies.

6.2.2 Particle size distribution

In general, A and P in eq. (6.3) do influence the PSD but the PSD and d_{min} are responsible for the discrete number of fragments created (Figure 6.7). Figure 6.8 shows the cumulative mass fraction in bin M_1, obtained from two independent SAG-mill models where only A has been modified. A does not directly influence the onset of fragmentation of original particles in bin M_1 but the generated

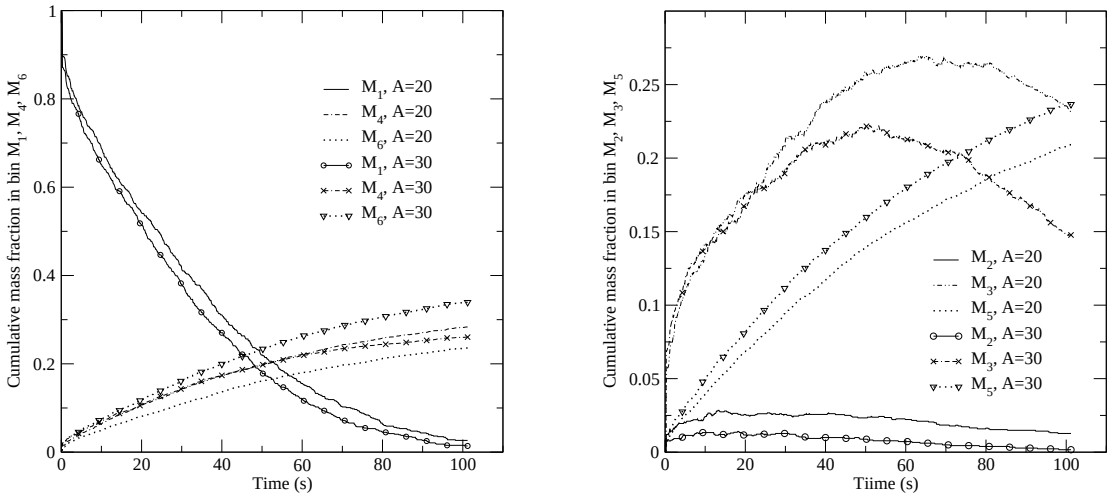

FIGURE 6.8: Cumulative mass fraction in each bin plotted over time for different values of A

progeny might cushion other particles differently. Furthermore, the model relies on a certain degree of randomness, so that slight variations are possible. Figure 6.8 further reveals other cumulative mass fractions in bin M_2, M_3, M_4, M_5 and M_6. For $A = 30$, less particles in bin M_2 and M_3 are created, a similar amount in bin M_4 but more in M_5 and M_6 compared to the $A = 20$ setting. These results are according to our expectation.

The progeny PSD from a single breaking plaster sphere has been compared between experimental data from Wu et al. [221] and model results obtained using the t_{10}-approach. Different diameters and impact energies have been used to verify its validity. The plaster used (material strength of 37MPa) is a brittle material, so that the minimum impact energy to achieve damage is low and has been set to $d\ E_0 = 0.1$. The material parameter $f_{Mat} = 0.03$ and $A = 13$ have been chosen to match the PSD of the plaster studied - a similar procedure as outlined by Vogel et al. [200] who found their breakage values by fitting their PSD to an expected master curve. All values for $d \cdot E_0$, f_{Mat} and A have been kept constant for the entire PDS plaster study. In the DFM model, dissipation does not affect the generated progeny PSD and is therefore irrelevant for this plaster study. Relevant model parameters are summarised in Table 6.2. It has been demonstrated that eq. (6.3) is able with constant material values to respond correctly to the PSD as a function of partice size and impact energy. Combined with the DFM model, rough predictions can be made for the size of each individual fragment. The reader should keep in mind that fragmentation is a very complex and to some extend random process and that the DFM model requires only a few material/breakage parameters. From that prospective, the size of each individual fragment obtained

TABLE 6.2: Parameters used for a comparison with experimental results

Variable	Value
Material parameter f_{Mat}	0.03 kg/Jm
Product (d E_0)	0.1 Jm/kg
A, the maximum achievable t_{10}	13
Particle density (assumed) ρ	1800 kg/m^3
Minimum fragment diameter d_{min}	1.0 mm

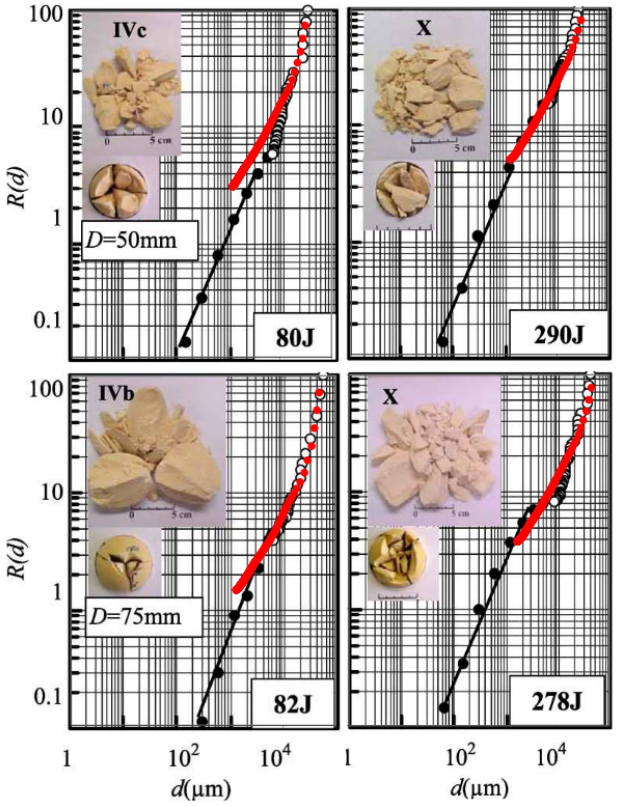

FIGURE 6.9: Cumulative weight in percentage $R(d)$ versus the fragment size in double logarithmic scale. The first and second row are for sphere diameter D=50 and 75 mm, respectively [221]. The red points are predictions from the DFM model.

in experiments (circle) and model predictions (red point in Figure 6.9) are similar and can be regarded as outstanding.

Creation of fragments is stopped, when roughly 96% of the original parent particle mass is used to create fragments and one single fragment has been created with the remaining mass. The same is valid for experiments where roughly 96% of the original particle mass is counted and measured by Wu et al. [221] and the remaining tiny fragments are approximated by a straight line (power law plotted over logarithmic axes). Both experimental results and model predictions are in excellent agreement, indicating a reasonable implementation of the theory (probability

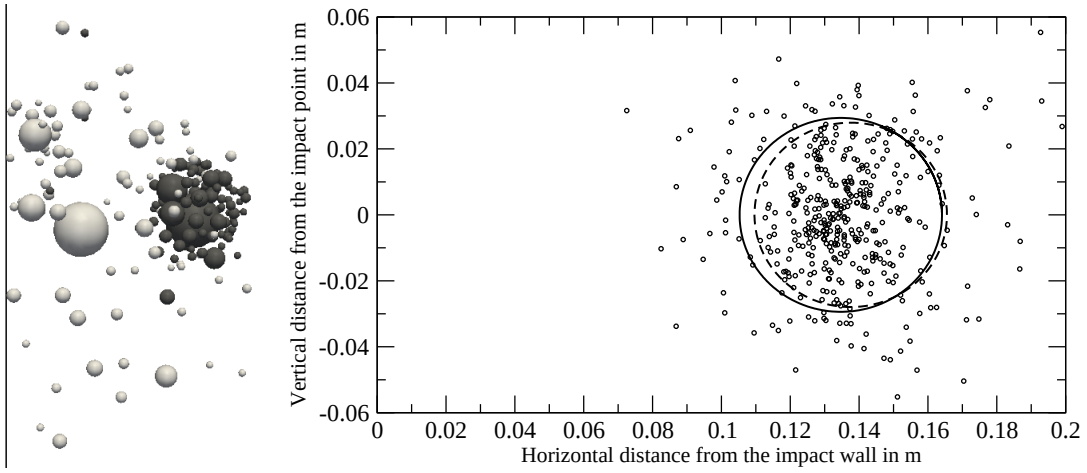

FIGURE 6.10: Left: Fragment cloud after normal incidence at the wall for a momentum factor of $e_F = 0.05$ (white fragments) and $e_F = 0.95$ (black fragments). Right: The averaged distance between each particle (points) and the cloud centre is drawn as a full circle (present model) which has been compared to the 2D hyper-velocity fragmentation model by Schäfer (broken circle) 27μs after wall impact.

of breakage and PSD).

As highlighted by Morrison et al. [201] the progeny PSD can be estimated by using the t_{10}-approach in eq. (6.3) for a variety of brittle materials - particularly rock and ore. During these studies it has been found that the t_{10}-approach is suitable for plaster but is not for e.g. glass where always an over-prediction of fine fragments has been observed.

6.2.3 Energy and momentum of the fragments

Fragment velocities indicate how the impact energy is partitioned and how the fragment cloud expands into the local surrounding. The momentum factor e_F in eq. (6.4) is responsible for the fragment cloud formation in the present model. The more initial momentum goes into the extensions of cracks, the lower is e_F and the bigger is the fragment cloud (the distance between fragments long after impact), which corresponds to the white particles in Figure 6.10 (left) and vice versa.

The present discrete fragmentation method considers particle kinetic and elastic energy separately like all soft-sphere discrete element models. At the moment of fragmentation, the model solves the momentum equation (6.6) to obtain the kinetic energy for each fragment (1. velocity component) and solves the energy equation (see eqs.(6.9-6.11)) to apply the remaining impact energy in the form

TABLE 6.3: Parameters used in the present 3D-DFM and Schäfer's 2D model, taken from Schäfer [222]

Variable	Value
Initial projectile velocity	6700 m/s
Initial projectile diameter	0.00496 m
Fragments diameter (monosize)	0.658 mm
Number of projectile fragments	428
Momentum of all wall fragments	0.2769 kgm/s
Energy of all wall fragments	649.95 J
Fraction of dissipated energy f'	0.23

of elastic energy between the fragments. The elastic energy is converted into kinetic energy, when all fragments have lost their mutual contact (2. velocity component). As this approach is novel for fragmentation models, it has been compared to the hyper-velocity-fragment-cloud model developed by Schäfer [222]. Both models have been simplified using 428 monosized fragments generated by a projectile with a diameter of 0.00496 m. The wall and projectile material is given as AL5754/AL1090 respectively. Therefore, typical aluminium properties have been used ($2700kg/m^3, E = 70GPa, \nu = 0.33$) throughout this study. The projectile hits the wall with normal incidence and a velocity of 6700 m/s. Schäfer's 2D fragmentation model spatially locates all projectile fragments uniformly distributed on the circumference of a circle (broken circle in Figure 6.10b). For the DFM model predictions, a similar circle (solid line) can be constructed, where the radius represents the average distance between the fragment cloud centre and each fragment position (points). To get equivalent boundary conditions, the DFM model has been corrected by the contribution of the momentum ($0.2769\frac{kgm}{s}$) and energy ($649.95J$) associated with the wall bumper fragments and energy losses (23% of the total impact energy) e.g. due to melting. The value e_F has been set to unity. This is because the effect of melting and wall bumper fragments cannot be considered in a coefficient of restitution. All other breakage parameters do not affect the results (probability of breakage is set to one and the size distribution is replaced by mono-sized fragments as used in the simplified 2D model developed by Schäfer). The fluid phase drag force is set to zero and the general coefficient of restitution is set to unity ($e = 1$). Wall or particle friction is not considered as tangential forces (rotation) are not taken into account during normal incidence or fragmentation. All model parameters for both models are taken from Schäfer [222] and summarised in Table 6.3.

All points in Figure 6.10 (right) belong to the DFM model and their average

distance from the cloud centre is plotted as the solid circle. It has been found that the first velocity component, given by the initial velocity derived from the momentum equation, differs by -2%. This value has been determined as the ratio of each model's predicted distance between cloud centre and impact point. The second velocity component, differs by 5%, determined as the ratio of the averaged cloud (circle) diameter of both models. Both numbers are in opposite directions, meaning that a higher first velocity component would decrease the second one. The result demonstrates that both predictions are in good agreement and that artificial overlaps are correctly translated. Small deviations have to be traced back to their working mechanisms (cloud centre or cloud radius during wall impact at the very beginning is not exactly the same, the aluminium stiffness used for the soft-sphere model influences the delay of the returning fragment cloud, etc.). The comparison of these two models is limited to the momentum and energy equations and their direct impact on the fragment cloud only as their field of application differs significantly. The present model cannot be applied for crater formation studies and cannot handle melting of metallic projectiles during hypervelocity impacts. However, it can be concluded that the implemented energy and momentum equation give fairly accurate results for missile velocities of up to 6700m/s to predict reasonable fragment velocities.

6.3 Conclusions

A new model has been developed, tested and validated to account for discrete, incremental, repetitive and/or simultaneous fragmentation events, particularly suitable for applications which involve numerous particles. Particles might fragment depending on the degree they have been previously damaged, their size, their material strength and the impact energy involved. Size distribution curves of broken plaster fragments have been modeled via the breakage index t_{10}, determined based on the breakage probability. Excellent agreement between experiments and model predictions is found. Fragmentation has been modelled up to impact velocities of 6700 m/s to demonstrate that momentum and energy equation are accurately implemented. The model is able to fragment particles into an infinite number of progeny particles as far as DEM-limitations concern. The code delivers much information about the fragmentation event, for instance the fragment velocity and trajectory from the moment of breakage, the degree of particle damage accumulated in the past, or PSDs to generate breakage rate curves to judge the performance of different applications. Information provided by the model can support

engineers in designing and optimising all kind of applications where fragmentation is involved without the use of empirical parameters. Material parameters used in that model are often derived from independent testing methods, providing they are not machine specific. Different approaches [200,202,203] might be useful to get appropriate model parameters. It is aimed to extend this yet purely mechanical-induced fragmentation model towards an even more general breakage model to include the effects of pressure and thermal stresses inside particles processed in fluidised beds.

The partition of the parent particle momentum and energy into the child particle values are compared to Schfer's method [222]. Results are in fairly good agreement. That gives some confidence that the momentum and energy distribution can be captured correctly by the two velocity component approach. Full validity cannot be claimed for the application in mills or fluidised beds as a direct validation with experiments of dense beds is almost impossible and the availability of parameters is limited (e.g. there are no experimental data or models to obtain e_F). However, with e_F chosen as a rather free parameter in the mill study, reasonable results (without the comparison to reality) have been obtained. It seems, the method is well applicable to dense bed fragmentation studies and is therefore recommended but suffers (still) from the availability of all parameters.

For all simulations undertaken, the fragmentation code itself is very time efficient. There is hardly any time delay recognisable for the moment of fragmentation ($<<$1 second)- it is rather the generated progeny of fine fragments which reduces the computational time performance of simulations (see eq. (3.14)). If there is a larger time delay during the fragmentation process, setting parameters are not wisely chosen (e.g. too many fragments?, packing algorithm needed?). The same is true for the cost of memory requirements, the moment of fragmentation itself is not a memory demanding process. However, the generated data quantity which need to be traced throughout the rest of the simulation can be high.

Chapter 7

Conclusions

7.1 Overall Conclusions

The combination of CFD and DEM is a very powerful numerical approach to investigate granular flow applications. Such simulations are simultaneous "measurements" of several properties which are difficult if not impossible to achieve by direct experimentation. CFD-DEM simulations including their multiphase flow coupling have been introduced by Tsuji [30] in 1993, went through tremendous attention ever since and turned into the most detailed numerical approach to model dense coarse granular multiphase flows today. Due to its novelty, further developments and customisations are needed to make this approach more applicable to engineering problems and to tackle its computational demand. This thesis introduces three novel cutting-edge DEM developments and corresponding simulations have been performed with a supercomputing infrastructure.

As pointed out in Section 1.2, 2D DEM modelling can lead to erroneous predictions. Most DEM studies are based on 2D or quasi-3D simulations - while 3D simulations are required to incorporate all necessary details [32]. Furthermore, DEM models are often used for very simplified overall conditions (e.g. too small domain) so that the overall set-up often appears to lack sophistication but not the DEM approach itself. Based on these findings from the literature review, much more attention needs to be paid to large-scale 3D simulations. There are simulation activities [223, 224] which consider far more than one million particles. They partially disregarded the fluid phase and large particles have been used to make simulations much faster (see eq. (3.14)). In the simulations discussed in this thesis, up to 0.8 million particles have been modelled where radiative and convective

heat transfer, shrinkage, drying and thermochemical degradation are considered for particle sizes down to 300μm (being less than a tenth of the size used by Tsuji et al. [223]). Currently, it can be concluded that the calculations performed in the scope of this thesis are one of the most advanced multi-processor simulations overall.

A drying model has been implemented and tested in MultiFlow. This model distinguishes between capillary free liquid and bound water migration, accounts for a porosity change and delivers useful information on the drying front inside the particle. It has been compared to a drying model developed by Di Blasi [162] and found to produce quantitatively similar results. It has been found, that this drying model is unnecessarily too complex to be widely applied in numerous particle simulations. Firstly, it only make sense to apply an appropriate model for the transport of liquid free water in a porous media and secondly for high moisture contents only. Therefore the computational demand can be reduced substantially for most applications by only modelling bound water transport (one partial differential equation for liquid free water, for each particle and each fluid time step can be dropped).

The simplified drying model based on bound water diffusion inside large drying particles has been applied to a batch drying process of 100g coffee beans inside a fluidised bed. It has been shown that the CFD-DEM approach with its multiscale capabilities can be further extended towards sub-particle scale modelling without eliminating flow or particle scale information. It has been successfully demonstated that this model is able to provide much more details than any other state-of-the-art coffee bean drying model. So far, it is the first attempt to model intra-particle energy and species transport inside numerous particles with the DEM.

As a second milestone, thermochemical degradation of biomass has been studied. To this end, the pyrolysis kinetic model originally proposed by Shafizadeh and Chin [163] has been used to numerically describe thermochemical degradation of a single, thermally thick, non-moving biomass particle. The model does not consider a gas phase inside the particle. Tar is released directly at the particle surface underestimating secondary tar reactions. It has been concluded, that for thermally thick particles or higher gas temperatures convective gas transport equations need to be implemented to capture the full extent of secondary tar reactions. Bubbling fluidised bed fast pyrolysis reactors operate with much smaller and much larger numbers of biomass particles compared to the previous coffee bean drying process.

This indicates that zero-dimensional, thermally thin particles are preferred when modelling fluidised bed fast pyrolysis processes.

This pyrolysis section has been extended towards a large-scale simulation in which biomass is fed into a bubbling fluidised bed. The thermochemical degradation process is still described by a reaction scheme with competing pathways but the model from Shafizadeh and Chin [163] has been replaced by a more generic approach introduced by Miller and Bellan [180]. The former depends on very specific kinetic data which are scarce in the literature while the latter is suited to describe the degradation behaviour of any biomass material. Results within this thesis support the theory that biomass in close contact with sand (good mixing) is the key to achieve rapid drying and high heating rates to obtain high bio-oil yields. In case of strong segregation, thermal particle isolation takes place and fast pyrolysis turns into slow pyrolysis. Most tar is released in near wall areas making it crucial for experimentalists to adjust wall temperature values. In case of low wall temperature values, biomass in its vicinity would deplete slowly producing mainly char while close to heated walls secondary tar reactions (see eq.(5.19)) become important. Heat transfer coefficients of single char particles are around 1000 W/m^2K - a very high but realistic value overall. The bio-oil yield is strongly dependent on the bed temperature but almost independent of the biomass moisture content. Entrainment of depleted biomass particles occur intermittently depending on the bubble behaviour. In case of entrainment, particles are not in contact with the wall in the upper freeboard section, all investigated particles stay in the middle of the reactor. Bubbles instead of splashes cause high particle accelerations and represent the main reason for entrainment. In the simulation, five seconds of real time are enough to obtain roughly steady-state gas compositions at the reactor outlet (see Figure 5.17). It requires much longer simulation times to obtain the same number of fed and entrained particles.

A new model has been developed for implementation into soft-sphere DEM models to improve the understanding of discrete fragmentation and for its use to model practical applications. Discrete, incremental, repetitive and/or simultaneous fragmentation events are taken into account as it can be often found during breakage where numerous particles are involved. Particles might fragment depending on the degree they got damaged before, their size, their material strength and the impact energy involved. Material parameters used in that model are often derived from independent testing methods indicating that they are not machine specific.

Compared to most other DEM model validations, each subsection is discussed individually. The onset of fragmentation has been discussed as a parametric analysis based on their sensitivity to the breakage frequency and results have been obtained according to our expectations. The fragment size distribution is modelled by using a single parameter t_{10}. It has been found that plaster fragment size distributions can be well predicted by the t_{10}-approach. The DFM model also predicts a discrete size of each fragment with generally good agreement found in experiments. As the first part of the model theory namely the probability of breakage and the t_{10} value are strongly related to each other, a reasonable implementation of the theory can be concluded. Fragmentation has been modelled up to impact velocities of 6700 m/s to demonstrate the reliability of the two velocity component approach used herein. The model is able to fragment particles into an infinite number of progeny particles as far as DEM-limitations concern. The code delivers much information related to the fragmentation event for instance the fragment velocity and trajectory from the moment of breakage, the degree of particle damage accumulated in the past or the progeny PSD. Model results can support engineers in designing and optimising all kind of applications where fragmentation is involved without the use of empirical parameters.

7.2 Future Work

Generally speaking, there is and there will be a high demand to further apply and extend CFD-DEM models to understand and optimise engineering applications. It is generally accepted [106, 225] that incorporation of inter-particle forces and intra-particle species (moisture, tar) migration are essential so that CFD becomes successful in modelling particle processing. This equally applies to any particle degradation process discussed in this thesis. Drying and pyrolysis of large particles can be better numerically represented when convective gas transport inside particles is considered. For drying and pyrolysis, intra-particle gas convection models in 1D have been extensively found in the literature and those are required to be implemented into MultiFlow.

The pyrolysis section can also be extended towards gasification. Homogeneous and heterogeneous reactions require a better understanding. It needs to be verified whether or not turbulence needs to be considered and if so, which model would be best suitable for such large grid approach (Reynolds-averaged Navier-Stokes or Large Eddy Simulations).

Convective gas transport inside particles allows to look at pressure build-up so that in turn primary and secondary fragmentation of fuel particles can be numerically scrutinised. The implementation of pressure-induced fragmentation is far more difficult as an inhomogeneous composition requires a reasonable redistribution to each fragment created and fragmentation parameters determining the size or energy distribution of fragments will be needed. Experimental data are less available for pressure-induced fragmentation of large fuel particles. The fragmentation model already implemented depends partially on random values which will increase the difficulty again to further validate such models.

Figure 7.1 illustrates the freeboard and splash zone of a fluidised bed. Herein, all blue particles are fragments due to mechanical-induced breakage in a fluidised bed. As a possible future outlook, particle deposition at walls is fairly easy to model as shown at the gray front wall section (these particles stick permanently to the wall). Together with studying entrainment of sticky char particles this work extension could lead to a better understanding of fouling or slagging in fluidised beds.

Most model extensions require more computational demand which desires compensation by more efficient simulation methods/approaches. One way could be to simply model only a rectangular domain e.g. a section of a cylinder. A better load partitioning is easier to achieve than it is for cylinders. There is not much experience on the best practice for the simultaneous fluid and particle mesh partitioning. There is certainly more potential to improve the computational performance on multiple cores.

Another larger project would be the development of a “dual-collision” approach, where each collision is updated based on the collision time. Very short lasting collisions could be solved with a hard-sphere approach while long-lasting collisions can be solved with a soft-sphere approach. This would save a lot of computational resources especially when tiny particles/fragments are created.

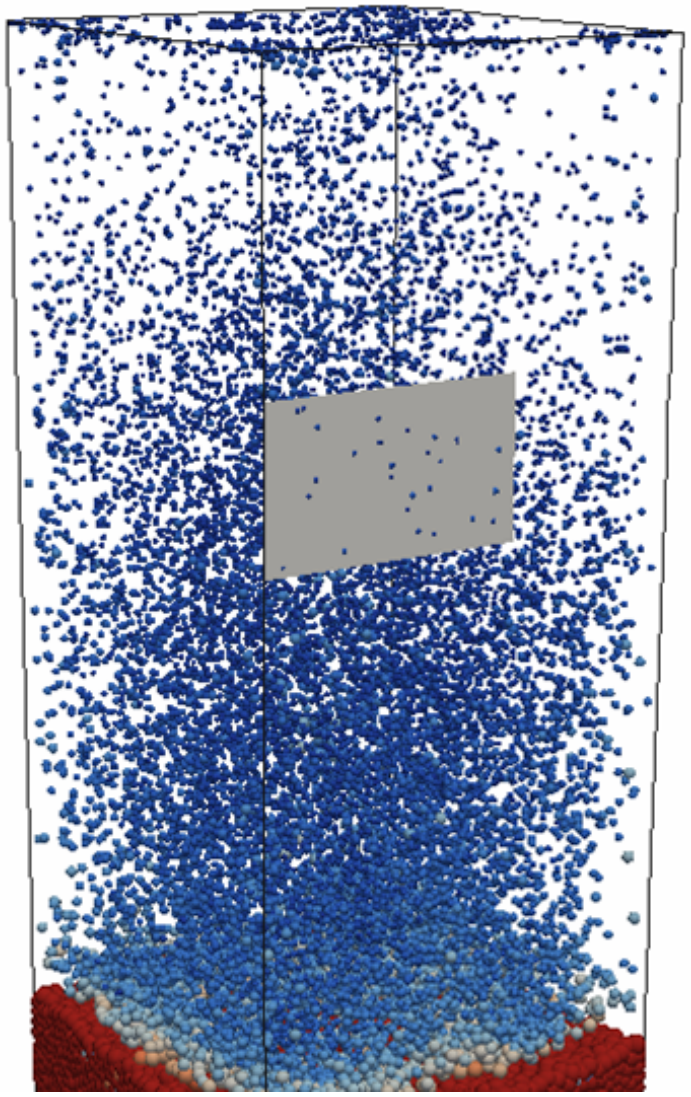

FIGURE 7.1: Freeboard of a fluidised bed with initially monosized particles and fragments generated by breakage

Appendix A

Discretisation procedure

This section deals with the discretisation via the finite difference method of any scalar transport equation applied within a spherical particle in one dimension. First-order forward Euler time discretisation is used while second-order fully implicit spatial discretisation is used with the central difference scheme [226]. The set of linear equations is then solved with the generalized minimum residual method with restarts (GMRES) with a tolerance set to 10^{-12} and a maximum number of iterations set to 50. A general partial differential equation in spherical coordinates reads:

$$\frac{\partial(\rho\Phi)}{\partial t} \approx \overline{\rho}\frac{\partial(\Phi)}{\partial t} = \frac{1}{r^2}\frac{\partial}{\partial r}\left(\Gamma r^2 \frac{\partial \Phi}{\partial r}\right) + \dot{\omega}, \tag{A.1}$$

where $\overline{\rho}$ is updated every iteration. Φ is the general scalar quantity, Γ is either the thermal or mass diffusivity and δr is the distance between two layer centres. Eq. (A.1) can be rewritten as

$$\begin{aligned}\frac{\overline{\rho}}{\Delta t}(\Phi_P - \Phi_P^0) &= \frac{2\Gamma_P}{r}\frac{(\Phi_E - \Phi_W)}{2\Delta r} + \frac{(\Gamma_E - \Gamma_W)}{2\Delta r}\frac{(\Phi_E - \Phi_W)}{2\Delta r} \\ &\quad + \Gamma_P \frac{(\Phi_E - 2\Phi_P + \Phi_W)}{\Delta r^2} + \dot{\omega}.\end{aligned} \tag{A.2}$$

For solving a system of linear equations, it is useful to rearrange eq. (A.2) into a general form according to eq. (A.3) and eq. (A.2) becomes eq. (A.4).

$$a\Phi_P = b\Phi_E + c\Phi_W + d \tag{A.3}$$

$$\left(\frac{\overline{\rho}}{\Delta t}+\frac{2\Gamma_P}{\Delta r^2}\right)\Phi_P = \left(\frac{\Gamma_P}{\Delta r^2}+\frac{(\Gamma_E-\Gamma_W)}{4\Delta r^2}+\frac{\Gamma_P}{r\Delta r}\right)\Phi_E + \left(\frac{\Gamma_P}{\Delta r^2}-\frac{(\Gamma_E-\Gamma_W)}{4\Delta r^2}-\frac{\Gamma_P}{r\Delta r}\right)\Phi_W + \left(\frac{\overline{\rho}}{\Delta t}\Phi_P^0+\dot{\omega}\right) \tag{A.4}$$

The scalar values in each layer inside the particle correspond to the solution vector Φ where A $\times\Phi = D$.

$$A=\begin{pmatrix} a_1 & -b_1 & 0 & 0 & \cdots \\ -c_2 & a_2 & -b_2 & 0 & \cdots \\ 0 & -c_3 & a_3 & -b_3 & \cdots \\ \cdots & \cdots & \cdots & \cdots & \cdots \end{pmatrix} \qquad \Phi=\begin{pmatrix} \Phi_1 \\ \Phi_2 \\ \Phi_3 \\ \cdots \end{pmatrix} \qquad D=\begin{pmatrix} d_1 \\ d_2 \\ d_3 \\ \cdots \end{pmatrix}$$

First, the boundary condition at the particle surface (r=R leading to a_1, b_1 and d_1) is discretised. The boundary condition is given by

$$\Gamma_P\frac{(\Phi_E-\Phi_P)}{\Delta r}=\Psi(\Phi_\infty-\Phi_P). \tag{A.5}$$

Ψ is typically the convective heat transfer coefficient or the mass transfer coefficient, if present. The scalar gradient outside the particle does not depend on a diffusion gradient inside the particle (it just depends on Φ_P) so that the right hand side of eq. (A.2) reads

$$\begin{aligned} = & \frac{2\Gamma_P}{r}\left(\frac{(\Phi_E-\Phi_P)}{\Delta r}+\frac{(\Phi_P-\Phi_W)}{\Delta r}\right) \\ & +\frac{1}{\Delta r}\left[\cancel{(\Gamma_E-\Gamma_P)}+(\Gamma_P-\Gamma_W)\right]\left(\cancel{\frac{\Phi_E-\Phi_P}{\Delta r}}+\frac{\Phi_P-\Phi_W}{\Delta r}\right) \\ & +\frac{\Gamma_P}{\Delta r}\left(\frac{(\Phi_E-\Phi_P)}{\Delta r}-\frac{(\Phi_P-\Phi_W)}{\Delta r}\right)+\dot{\omega} \end{aligned} \tag{A.6}$$

and after applying eq. (A.5) it reads

$$\begin{aligned} & \left(\frac{\overline{\rho}}{2\Delta t}+\frac{2\Psi}{r}-\frac{2\Gamma_P}{r\Delta r}-\frac{(\Gamma_P-\Gamma_W)}{\Delta r^2}+\frac{\Gamma_P}{\Delta r^2}+\frac{\Psi}{\Delta r}\right)\Phi_P \\ = & \left(-\frac{2\Gamma_P}{r\Delta r}-\frac{(\Gamma_P-\Gamma_W)}{\Delta r^2}+\frac{\Gamma_P}{\Delta r^2}\right)\Phi_W \\ + & \left(\frac{2\Psi}{r}+\frac{\Psi}{\Delta r}\right)\Phi_\infty+\frac{\overline{\rho}}{2\Delta t}\Phi_P^0+\dot{\omega}_P. \end{aligned} \tag{A.7}$$

At the particle centre, the scalar value and the diffusion coefficient Γ do not change compared to the west value and the boundary condition (r=0 leading to a_n, c_n

and d_n) is given as

$$\frac{\partial \Phi}{\partial r} = 0 = \frac{\Phi_P - \Phi_W}{\Delta r}. \tag{A.8}$$

The right hand side of eq. (A.2) can be written as

$$\begin{aligned} = \quad & \frac{2\Gamma_P}{r}\left(\frac{(\Phi_E - \Phi_P)}{\Delta r} + \cancel{\frac{(\Phi_P - \Phi_W)}{\Delta r}}\right) \\ & + \frac{1}{\Delta r}\left[(\Gamma_E - \Gamma_P) + \cancel{(\Gamma_P - \Gamma_W)}\right]\left(\frac{\Phi_E - \Phi_P}{\Delta r} + \cancel{\frac{\Phi_P - \Phi_W}{\Delta r}}\right) \\ & + \frac{\Gamma_P}{\Delta r}\left(\frac{(\Phi_E - \Phi_P)}{\Delta r} - \cancel{\frac{(\Phi_P - \Phi_W)}{\Delta r}}\right) + \dot{\omega}, \end{aligned} \tag{A.9}$$

leading to the discretised form for the particle centre written as

$$\begin{aligned} & \left(\frac{\overline{\rho}}{\Delta t} + \frac{2\Gamma_P}{r\Delta r} + \frac{(\Gamma_E - \Gamma_P)}{\Delta r^2} + \frac{\Gamma_P}{\Delta r^2}\right)\Phi_P \\ = \quad & \left(\frac{2\Gamma_P}{r\Delta r} + \frac{(\Gamma_E - \Gamma_P)}{\Delta r^2} + \frac{\Gamma_P}{\Delta r^2}\right)\Phi_E \\ + \quad & \frac{\overline{\rho}}{\Delta t}\Phi_P^0 + \dot{\omega}. \end{aligned} \tag{A.10}$$

The particle mesh is outlined in Figure A.1. The particle surface coincide with a cell centre while the particle centre coincide with a cell face. The relative distance to the centre r might otherwise become zero and is not numerically acceptable.

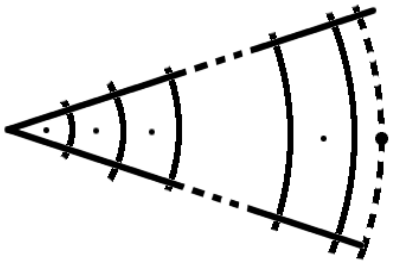

FIGURE A.1: 1D mesh used for temperature and species predictions within a spherical particle.

Bibliography

[1] Kunii, D., and Levenspiel, O., 2005. *Fluidization Engineering, Second Edition.* Elsevier.

[2] Syahrul, S., Hamdullahpur, F., and Dincer, I., 2002. "Exergy analysis of fluidized bed drying of moist particles". *Exergy, an International Journal,* ***2***, pp. 87–98.

[3] Geldart, D., 1973. "Types of gas fluidization". *Powder Technology,* ***7***, pp. 285–292.

[4] van Wachem, B., 2000. *Derivation, implementation and validation of computer simulation models for gas-solid fluidized beds.* PhD-Thesis, Delft-University of Technology.

[5] van der Hoef, M., van Sint Annaland, M., Deen, N., and Kuipers, J., 2008. "Numerical simulation of dense gas-solid fluidised beds: a multiscale modelling strategy". *Annu. Rev. Fluid. Mech,* ***40***, pp. 47–70.

[6] Passalacqua, A., Fox, R., Garg, R., and Subramaniam, S., 2010. "A fully coupled quadrature-based moment method for dilute to moderate dilute fluid-particle flows". *Chemical Engineering Science,* ***65***, pp. 2267–2283.

[7] Desjardin, O., Fox, R., and Villedieu, P., 2008. "A quadrature-based momentum method for dilute fluid-particle flows". *J. Comput. Phys,* ***227***, pp. 2524–2539.

[8] Oevermann, M., Gerber, S., and Behrendt, F., 2009. "Euler-Lagrange/DEM simulation of wood gasification in a bubbling fluidized bed reactor". *Particuology,* ***7***, pp. 307–316.

[9] Hajidavalloo, E., and Hamdullahpur, F., 2000. "Thermal analysis of a fluidized bed drying process for crops. Part I: Mathematical modeling". *International Journal of Energy Research,* ***24***, pp. 791–807.

[10] Geldart, D., 1986. *Gas Fluidization Technology.* John Wiley & Sons, New York, USA.

[11] van Wachem, B., Schouten, J., Krishna, R., and van den Bleek, C., 2001. "Experimental validation of Lagrangian-Eulerian simulations of fluidized beds". *Powder Technology,* ***116***(2), pp. 155–165.

[12] Feng, Y., and Yu, A., 2010. "Effect of bed thickness on the segregation behavior of particle mixtures in a gas fluidized bed". *Ind. Eng. Chem. Res,* ***49***, pp. 3459–3468.

[13] Freige, F., and Langston, P., 2004. "Integration schemes and damping algorithms in distinct element models". *Advanced Powder Technology,* ***15***(2), pp. 227–245.

[14] Akpinar, E., Bicer, Y., and Yildiz, C., 2003. "Thin layer drying of red pepper". *Journal of Food Engineering,* ***59***, pp. 99–104.

[15] Dincer, I., 1998. "Moisture loss from wood products during drying - Part I: moisture diffusivities and moisture transfer coefficients". *Energy Sources,* ***20***, pp. 531–539.

[16] Rhodes, M., 1998. *Introduction to particle technology.* John Wiley & Sons.

[17] Chandran, A., Subba Rao, S., and Varma, Y., 1990. "Fluidized bed drying of solids". *AIChE Journal,* ***36***(1), pp. 29–38.

[18] Bridgwater, A., 2008. *Fast Pyrolysis of Biomass: A Handbook.* ISBN: 978-1-872691-07-7.

[19] Laird, D., Brown, R., Amonette, J., and Lehmann, J., 2009. "Review of the pyrolysis platform for co-producing bio-oil and bio-char". *Biofuels, Bioproducts and Biorefining,* ***3***(5), pp. 547–562.

[20] Brewer, C., Schmidt-Rohr, K., Satrio, J., and Brown, R., 2009. "Characterization of biochar from fast pyrolysis and gasification systems". *Environmental Progress & Sustainable Energy,* ***28***(3), pp. 386–396.

[21] Czernik, S., and Bridgwater, A., 2004. "Overview of applications of biomass fast pyrolysis oil". *Energy & Fuels,* ***18***, pp. 590–598.

[22] Farrell, A., Plevin, R., Turner, B., Jones, A., O'Hare, M., and Kammen, M., 2006. "Ethanol can contribute to energy and environmental goals". *Science,* ***311***, pp. 506–508.

[23] Fuerstenau, D., and Abouzeid, A., 2002. "The energy efficiency of ball mill in comminution". *Int. J. Miner. Process,* ***67***, pp. 161–185.

[24] R.D.Morrison, and Cleary, P., 2008. "Towards a virtual comminution machine". *Mineral Engineering,* ***21***, pp. 770–781.

[25] Deniz, V., 2003. "A study on the specific rate of breakage of cement materials in a laboratory ball mill". *Cement and Concrete Research,* ***33***, pp. 439–445.

[26] Nemtsov, D., and Zabaniotou, A., 2008. "Mathematical modelling and simulation approaches of agricultural residues air gasification in a bubbling fluidized beds reactor". *Chemical Engineering Journal,* ***143***, pp. 10–31.

[27] Brown, R., Ahrens, J., and Christofides, N., 1992. "The contribution of attrition and fragmentation to char elutriation from fluidized beds". *Combustion and Flame,* ***89***, pp. 95–102.

[28] Gómez-Barea, A., and Leckner, B., 2010. "Modeling of bimass gasification in fluidized bed". *Progress in Energy and Combustion Science,* ***36***, pp. 444–509.

[29] Cundall, P., and Strack, O., 1979. "A discrete numerical model for granular assemblies". *Geotechnique,* ***29***(10), pp. 47–65.

[30] Tsuji, Y., Kawaguchi, T., and Tanaka, T., 1993. "Discrete particle simulation of two-dimensional fluidized beds". *Powder Technology,* ***77***, pp. 79–87.

[31] Hoomans, B., Kuipers, J., Briels, J., and Van Swaaij, W., 1996. "Discrete particle simulation of bubble and slug formation in a two-dimensional gas-fluidised bed: a hard-sphere approach". *Chemical Engineering Science,* ***51***, pp. 99–118.

[32] Deen, N., van Sint Annaland, M., Van der Hoef, M., and Kuipers, J., 2007. "Review of discrete particle modeling of fluidized beds". *Chemical Engineering Science,* ***62***, pp. 28–44.

[33] Schäfer, J., Dippel, S., and Wolf, D., 1996. "Force scheme in simulations of granular materials". *Journal de Physique,* ***6***(1), pp. 5–20.

[34] Xu, B., and Yu, A., 1997. "Numerical simulation of the gas-solid flow in a fluidized bed by combining discrete particle method with computational fluid dynamics". *Chemical Engineering Science,* ***52***(16), pp. 2785–2809.

[35] Xu, B., Yu, A., Chew, S., and Zulli, P., 2000. "Numerical simulation of gas-solid flow in bed with lateral gas blasting". *Powder Technology,* ***109***(1), pp. 13–26.

[36] Yu, A., and Xu, B., 2003. "Particle-scale modelling of gas-solid flow in fluidisation". *Journal of Chemical Technology and Biotechnology,* ***78***, pp. 111–121.

[37] Bokkers, G., van Sint Annaland, M., and Kuipers, J., 2004. "Mixing and segregation in a bidisperse gas-solid fluidised bed: a numerical and experimental study". *Powder Technology,* ***140***(3), pp. 176–186.

[38] Wang, X., and Rhodes, M., 2004. "Mechanistic study defluidization by numerical simulation". *Chemical Engineering Science,* ***59***(1), pp. 215–222.

[39] Wang, X., and Rhodes, M., 2005. "Using pulsed flow to overcome defluidization". *Chemical Engineering Science,* ***60***(18), pp. 5177–5181.

[40] Wang, X., and Rhodes, M., 2003. "Determination of particle residence time at the walls of gas fluidized beds by discrete element method simulation". *Chemical Engineering Science,* ***58***(2), pp. 387–395.

[41] Wang, X., and Rhodes, M., 2005. "A DEM study of particle motion near the walls of gas fluidized beds". *Powder Technology,* ***160***(1), pp. 15–19.

[42] Kawaguchi, T., Tanaka, T., and Tsuji, Y., 1998. "Numerical simulation of two-dimensional fluidized beds using the discrete element method (comparison between the two- and three-dimensional models)". *Powder Technology,* ***96***(2), pp. 129–138.

[43] Rhodes, M., Wang, X., Nguyen, M., P.Stewart, and Liffman, K., 2001. "Study of mixing in gas-fluidized beds using a DEM model". *Chemical Engineering Science,* ***56***(8), pp. 2859–2866.

[44] Feng, Y., Xu, B., Zhang, S., Yu, A., and Zulli, P., 2004. "Discrete particle simulation of gas fluidization of particle mixtures". *AIChE Journal,* ***50***(8), pp. 1713–1728.

[45] Takeuchi, S., Wang, S., and Rhodes, M., 2005. "Discrete element study of particle circulation in a 3-D spouted bed". *Chemical Engineering Science,* ***60***(5), pp. 1267–1276.

[46] Link, J., Cuypers, L., Deen, N., and Kuipers, J., 2005. "Flow regimes in a spout-fluid bed: a combined experimental and simulation study". *Chemical Engineering Science,* ***60***, pp. 3425–3442.

[47] Kawaguchi, T., Sakamoto, M., Tanaka, T., and Tsuji, Y., 2000. "Quasi-three-dimensional numerical simulation of spouted beds in cylinder". *Powder Technology,* ***109***, pp. 3–12.

[48] Djordjevic, N., Morrison, R., Loveday, B., and Cleary, P., 2006. "Modelling comminution patterns within a pilot scale AG/SAG mill". *Minerals Engineering,* ***19***, pp. 1505–1516.

[49] Goda, T., and Ebert, F., 2005. "Three-dimensional discrete element simulation in hoppers and silos". *Powder Technology,* ***158***, pp. 58–68.

[50] Cleary, P., and Sawley, M., 2002. "DEM modelling of industrial granular flows: 3D case studies and the effect of particle shape on hopper discharge". *Applied Mathematical Modelling,* ***26***(2), pp. 89–111.

[51] Fries, L., Antonyuk, S., Heinrich, S., and Palzer, S., 2011. "DEM-CFD modeling of a fluidized bed spray granulator". *Chemical Engineering Science,* ***66***, pp. 2340–2355.

[52] Ye, M., van der Hoef, M., and Kuipers, J., 2005. "The effects of particle and gas properties on the fluidization of Geldart A particles". *Chemical Engineering Science,* ***60***, pp. 4567–4580.

[53] Kafui, D., and Thornton, C., 2008. "Fully-3D DEM simulation of fluidised bed spray granulation using an exploratory surface energy-based pray zone concept". *Powder Technology,* ***184***, pp. 177–188.

[54] Limtrakul, S., Boonsrirat, A., and Vatanatham, T., 2004. "DEM modeling and simulation of a catalytic gas-solid fluidized bed reactor: a spouted bed as a case study". *Chemical Engineering Science,* ***59***, pp. 5225–5231.

[55] Brown, R., 2003. *Biorenewable Resources: Engineering New Products from Agriculture*. Iowa State Press A Blackwell Publishing Company.

[56] Di Blasi, C., 1998. "Multi-phase moisture transfer in the high-temperature drying of wood particles". *Chemical Engineering Science,* ***53***(2), pp. 353–366.

[57] Perre, P., and Degiovanni, A., 1990. "Simulation par volumes finis des transferts couples en milieux poreux anisotropes: sechage du bois a basse et a haute temperature". *Int. Journal of Heat and Mass Transfer,* ***33***(11), pp. 2463–2478.

[58] Nasrallah, S., and Perre, P., 1988. "Detailed study of a model of heat and mass transfer during convective drying of porous media". *Int. Journal of Heat and Mass Transfer,* ***31***(5), pp. 957–967.

[59] Bryden, K., and Hagge, M., 2003. "Modeling the combined impact of moisture and char shrinkage on the pyrolysis of a biomass particle". *Fuel,* ***82***, pp. 1633–1644.

[60] Bryden, K., Ragland, K., and Rutland, C., 2002. "Modeling thermally thick pyrolysis of wood". *Biomass & Bioenergy,* ***22***(1), pp. 41–53.

[61] Zhang, K., and You, C., 2010. "Experimental and numerical investigation of convective drying of single coarse lignite particles". *Energy Fuels,* ***24***, pp. 6428–6436.

[62] Fohr, J., and Moussa, H., 1994. "Heat and mass transfer in a cylindrical grain silo submitted to a periodical wall heat flux". *Int. J. Heat Mass Transfer,* ***37***(12), pp. 1699–1712.

[63] Pen, S., Besant, R., and Strathdee, G., 2000. "Heat and mass transfer in granular potash fertilizer with a surface dissolution reaction". *The Canadian Journal of Chemical Engineering,* ***78***(6), pp. 1076–1086.

[64] Ng, W., and Tan, R., 2006. "Investigation of drying Geldart D and B particles in different fluidization regimes". *The Canadian Journal of Chemical Engineering,* ***84***(6), pp. 656–662.

[65] Alves-Filho, O., Senadeera, W., and Eikevik, T. "Pet food from bovine origin drying by green heat pump technology and fluidization". *Food Innova 2010, Valencia, 25-29 October 2010.*

[66] Magalhaes, A., and Pinho, C., 2008. "Spouted bed drying of cork stoppers". *Chemical Engineering and Processing,* ***47***, pp. 2395–2401.

[67] Heertjes, P., 1962. "Simultaneous heat and mass transfer in a fluidized bed of drying silca gel". *The Canadian Journal of Chemical Engineering,* ***40***(3), pp. 105–109.

[68] Topuz, A., Gur, M., and Gul, M., 2004. "An experimental and numerical study on fluidized bed drying of hazelnuts". *Applied Thermal Engineering,* ***24***, pp. 1535–1547.

[69] Wurzenberger, J., Wallner, S., Raupenstrauch, H., and Khinast, J., 2002. "Thermal conversion of biomass: Comprehensive reactor and particle modeling". *AIChE Journal,* ***48***(10), pp. 2398–2411.

[70] Peters, B., Schröder, E., and Bruch, C., 2003. "Measurements and particle resolved modelling of the thermo- and fluid dynamics of a packed bed". *Journal of Analytical and Applied Pyrolysis,* ***70***, pp. 211–231.

[71] Bruch, C., Peters, B., and Nussbaumer, T., 2003. "Modelling wood combustion under fixed bed conditions". *Fuel,* ***82***, pp. 729–738.

[72] Sahni, E., Chaudhuri, B., and Strong, J., 2011. "DEM based model for mixing and heat transfer in an agitated filter dryer". *AIChE Confex, Annual Meeting.*

[73] Li, J., and Mason, D., 2002. "Application of the discrete element modelling in air drying of particulate solids". *Drying Technology,* ***20***(2), pp. 255–282.

[74] DiMattia, D., Amyotte, P., and Hamdullahpur, F., 1996. "Fluidized bed drying of large particles". *Transactions of the ASABE,* ***39***(5), pp. 1745–1750.

[75] Chandrasekar, V., and Viswanathan, R., 1999. "Physical and thermal properties of coffee". *Journal of Agriculture Engineering Research,* ***73***, pp. 227–234.

[76] Schwartzberg, H., 2002. *Modelling bean heating during batch roasting of coffee beans. In J.Welti-Chanes, G.Barbosa-Canovas and J.M. Aguilera (Eds.), Engineering and food for the 21st century.* Boca Raton: CRC Press LLC, London, New York.

[77] Heyd, B., Broyart, B., Hernandez, J., Valdovinos-Tijerino, B., and Trystram, G., 2007. "Physical model of heat and mass transfer in a spouted bed coffee roaster". *Drying Technology,* ***25***, pp. 1243–1248.

[78] Nagaraju, V., Murthy, C., Ramalakshmi, K., and Srinivaso-Rao, P., 1997. "Studies on roasting of coffee beans in a spouting bed". *Journal of Food Engineering,* ***31***, pp. 263–270.

[79] Hernández, J., Heyd, B., Irles, C., Valdovinos, B., and Trystram, G., 2007. "Analysis of heat and mass transfer during coffee batch roasting". *Journal of Food Engineering,* ***78***, pp. 1141–1148.

[80] Varadharaju, N., Karunaanidhi, C., and Kailappan, R., 2001. "Coffee cherry drying: A two-layer model". *Drying Technology,* ***19***(4), pp. 709–715.

[81] Ciro-Valásquez, H., Abud-Cano, L., and Pérez-Alegría, L., 2010. "Numerical simulation of thin layer coffee drying by control volumes". *Dyna,* ***77***(163), pp. 270–278.

[82] Hernández-Díaz, W., Ruiz-López, I., Salgado-Cervantes, M., Rodrígez-Jimenes, G., and García-Alvarado, M., 2008. "Modelling heat and mass transfer during drying of green coffee beans using polate spheroidal geometry". *Journal of Food Engineering,* ***86***, pp. 1–9.

[83] Yeretzian, C., Jordan, A., and Badoud, R., 2002. "From the green bean to the cup of coffee: investigating coffee roasting by on-line monitoring of volatiles". *European Food Reserach Technology,* ***214***, pp. 92–104.

[84] Bridgwater, A., 1999. "Principles and practice of biomass fast pyrolysis for liquids". *Journal of Analytical and Applied Pyrolysis,* ***51***, pp. 3–22.

[85] Koufopanos, C., Papayannakos, N., Maschio, G., and Lucchesi, A., 1991. "Modelling of the pyrolysis of biomass particles. Studies on kinetics, thermal and heat transfer effects". *Canadian Journal of Chemical Engineering,* ***69***, pp. 907–915.

[86] Di Blasi, C., 1996. "Kinetic and heat transfer control in the slow and flash pyrolysis of solids". *Ind. Eng. Chem. Res.,* ***35***, pp. 37–46.

[87] Di Blasi, C., 2000. "Modelling the fast pyrolysis of cellulosic particles in fluid-bed reactors". *Chemical Engineering Science,* ***55***, pp. 5999–6013.

[88] Authier, O., Ferrer, M., Mauviel, G., Khalfi, A., and Lédé, J., 2009. "Wood fast pyrolysis: Comparison of Lagrangian and Eulerian modeling approaches with experimental measurements". *Ind. Eng. Chem. Res. & Engineering Chemistry Research,* ***48***, pp. 4796–4809.

[89] Sadhukhan, A., Gupta, P., and Saha, R., 2008. "Modelling and experimental studies on pyrolysis of biomass particles". *Journal of Analytical and Applied Pyrolysis,* ***81***(2), pp. 183–192.

[90] Larfeldt, J., Leckner, B., and Melaaen, M., 2000. "Modelling and measurements of the pyrolysis of large wood particles". *Fuel,* ***79***, pp. 1637–1643.

[91] Papadikis, K., Gu, S., and Bridgwater, A., 2008. "CFD modelling of fast pyrolysis of biomass in fluidised bed reactors. Part A Eulerian computation of momentum transport in bubbling fluidised beds". *Chemical Engineering Science,* ***63***(16), pp. 4218–4227.

[92] Papadikis, K., Gu, S., and Bridgwater, A., 2009. "CFD modelling of fast pyrolysis of biomass in fluidised bed reactors. Part B Heat, momentum and mass transport in bubbling fluidised beds". *Chemical Engineering Science,* ***64***(5), pp. 1036–1045.

[93] Papadikis, K., Gu, S., and Bridgwater, A., 2009. "CFD modelling of fast pyrolysis of biomass in fluidised bed reactors: Modelling the impact of biomass shrinkage". *Chemical Engineering Journal,* ***149***, pp. 417–427.

[94] Zhou, Z., Yu, A., and Zulli, P., 2009. "Particle scale study of heat transfer in packed and bubbling fluidised beds". *AIChE Journal,* ***55***(4), pp. 868–884.

[95] Zhou, H., Flamant, G., and Gauthier, D., 2004. "DEM-LES simulation of coal combustion in a bubbling fluidized bed Part II: coal combustion at the particle level". *Chemical Engineering Science,* ***59***, pp. 4205–4215.

[96] Rong, D., and Horio, M., 1999. "DEM simulation of char combustion in a fluidized bed". *2nd Int. Conf. on CFD in the Minerals and Process Industries, Melbourne Australia.*

[97] Rabinovich, O., Borodulya, V., Vinogradov, L., and Korban, V., 2010. "Fast pyrolysis of an ensemble of biomass particles in a fluidized bed". *Journal of Engineering Physics and Thermophysics,* ***83***(4), pp. 694–704.

[98] Peters, B., 2002. "Measurements and application of a discrete particle model (DPM) to simulate combustion of a packed bed of individual fuel particles". *Combustion and Flame,* ***131***, pp. 132–148.

[99] Peters, B., Bruch, C., and Nussbaumer, T., 2003. "Modelling of wood combustion under fixed bed conditions". *Fuel,* ***82***(6), pp. 729–738.

[100] Peters, B., Dziugys, A., and Navakas, R. "A discrete approach to thermal conversion of solid fuel by the discrete particle method (DPM)". *10th International Conference on Modern Building Materials, Structures and Techniques,19-21 May 2010, Vilnius, Lithuania.*

[101] Peters, B., and Raupenstrauch, H., 2010. *Combustion Handbook, Chapter Modelling moving and fix bed combustion.* Wiley.

[102] Geng, Y., and Che, D., 2011. "An extended DEM-CFD model for char combustion in a bubbling fluidized bed combustor of inert sand". *Chemical Engineering Science,* ***66***, pp. 207–219.

[103] Miller, R., and Bellan, J., 1998. "Numerical simulation of vortex pyrolysis reactors for condensable tar production from biomass". *Energy and Fuels,* ***12***, pp. 25–40.

[104] Lathouwers, D., and Bellan, J., 2001. "Yield optimization and scaling of fluidized beds for tar production from biomass". *Energy Fuels,* ***15***, pp. 1247–1262.

[105] Xue, Q., Heindel, T., and Fox, R., 2011. "A CFD model for biomass fast pyrolysis in fluidized-bed reactors". *Chemical Engineering Science,* ***66***, pp. 2440–2452.

[106] Di Blasi, C., 2008. "Modeling chemical and physical processes of wood and biomass pyrolysis". *Progress in Energy and Combustion Science,* ***34***, pp. 47–90.

[107] Wen, C., and Chen, L., 1982. "Fluidized bed freeboard phenomena: Entrainment and elutriation". *AIChE Journal,* ***28***(1), pp. 117–128.

[108] Kersten, S., Wang, X., Prins, W., and van Swaaij, W., 2005. "Biomass pyrolysis in a fluidized bed reactor. Part 1: Literature review and model simulations". *Ind. Eng. Chem. Res,* ***44***, pp. 8773–8785.

[109] Babu, B., and Chaurasia, A., 2004. "Heat transfer and kinetics in the pyrolysis of shrinking biomass particle". *Chemical Engineering Science,* ***39***, pp. 1999–2012.

[110] Khanal, M., Schubert, W., and Tomas, J., 2007. "Discrete element method simulation of bed comminution". *Minerals Engineering,* ***20***, pp. 179–187.

[111] Kun, F., and Herrmann, H., 1996. "A study of fragmentation processes using a discrete element method". *Comput. Methods Appl. Mech. Engrg,* ***138***, pp. 3–18.

[112] Potapov, A., and Campbell, C., 1997. "Computer simulation of shear-induced particle attrition". *Powder Technology,* ***94***, pp. 109–122.

[113] Potapov, A., and Campbell, C., 1994. "Computer simulation of impact-induced particle breakage". *Powder Technology,* ***81***, pp. 207–216.

[114] Whittaker, B., Singh, R., and Sun, G., 1992. "Rock fracture mechanics: Principles, design and application". *Elsevier, Amsterdam.*

[115] Kipp, M., Grady, D., and Chen, E., 1980. "Strain rate dependent fracture initiation". *Int. J. Fracture,* ***16***, pp. 471–478.

[116] Hosseininia, E., and Mirghasemi, A., 2006. "Numerical simulation of breakage of two-dimensional polygon-shaped particles using discrete element method". *Powder Technology,* ***166***, pp. 100–112.

[117] Bagherzahdeh-Khalkhali, A., Mirghasemi, A., and Mohammadi, S., 2008. "Micromechanics of breakage in sharp-edge particles using combined DEM and FEM". *Particuology,* ***6***, pp. 347–361.

[118] Mc Dowell, G., and Harireche, O., 2002. "Discrete element modelling of soil particle fracture". *Géotechnique,* ***52***(2), pp. 131–135.

[119] Robertson, D., and Bolton, M., 2001. "DEM simulation of crushable grains and soils". *Proc. Powder and Grains, Sendai, Japan,* ***56***, pp. 623–626.

[120] Cheng, Y., Nakata, Y., and Bolton, M., 2003. "Discrete element simulation of crushable soil". *Géotechnique,* ***53***(7), pp. 633–641.

[121] Herbst, J., and Potapov, A., 2004. "Making a discrete grain breakage model practical for comminution equipment performance simulation". *Powder Technology,* ***143***, pp. 144–150.

[122] Cleary, P., 2001. "Recent advances in DEM modelling of tumbling mills". *Mineral Engineering,* ***14***(10), pp. 1295–1319.

[123] Mezhericher, M., Levy, A., and Borde, I., 2008. "Modelling of particle breakage during drying". *Chemical Engineering and Processing,* ***47***, pp. 1404–1411.

[124] Syred, N., Kurniawan, K., Griffiths, T., Gralton, T., and Ray, R., 2007. "Development of fragmentation models for solid fuel combustion and gasification as subroutines for inclusion in CFD codes". *Fuel,* ***86***, pp. 2221–2231.

[125] Zhang, H., Cen, K., Yan, J., and Ni, M., 2002. "The fragmentation of coal particles during the coal combustion in a fluidised bed". *Fuel,* ***81***, pp. 1835–1840.

[126] Sudhakar, D., Reddy, K., Kolar, A., and Leckner, B., 2008. "Fragmentation of wood char in a laboratory scale fluidized bed combustor". *Fuel,* ***89***, pp. 1121–1134.

[127] Hastaoglu, M., Kahraman, R., and Syed, M., 2000. "Pellet breakup due to pressure generated during wood pyrolysis". *Ind. Eng. Chem. Res,* ***39***, pp. 3255–3263.

[128] Tinney, E., 1965. "The combustion of wooden dowels in heated air". *Tenth Symposium (International) on Combustion*, pp. 925–930.

[129] van Wachem, B., Yu, X., and Hsu, T., 2010. "A 3D Eulerian-Lagrangian numerical model for sediment transport". *7th Int. Conf. on Multiphase Flow, ICMF 2010.*

[130] van Wachem, B., Remmelgas, J., and Niklasson-Björn, I., 2010. "Simulation of detailed flow behaviour in a wurster-type fluidized bed based upon discrete element and two-fluid modeling". *7th Int. Conf. on Multiphase Flow, ICMF 2010.*

[131] Di Renzo, A., and Di Maio, F., 2004. "Comparison of contact-force models for the simulation of collisions in DEM-based granular flow codes". *Chemical Engineering Science,* ***59***, pp. 525–541.

[132] Snir, M., Otto, S., Huss-Lederman, S., Walker, D., and Dongarra, J., 1995. *MPI: The complete reference.* MIT Press. http://www.netlib.org/utk/papers/mpi-book/mpi-book.html.

[133] van Wachem, B., 2011. "MultiFlow user manual, available together with MultiFlow from the MultiFlow repository (SVN client required)".

[134] Wen, C., and Yu, Y., 1966. "Mechanics of fluidization". *Chem. Eng. Progr. Symp. Series,* ***62***, pp. 100–111.

[135] van Wachem, B., Schouten, J., van den Bleek, C., Krishna, R., and Sinclair, J., 2001. "Comparative analysis of CFD models of dense gas-solid systems". *AIChE J,* ***47***, pp. 1035–1051.

[136] Baron, T., Briens, C., and Bergougnou, M., 1988. "Study on the transport disengagement height". *The Canadian Journal of Chemical Engineering,* ***66***, pp. 749–760.

[137] Rhie, C., and Chow, W., 1983. "Numerical study of the turbulent flow past an airfoil with trailing edge separation". *AIAA Journal,* ***21***, pp. 1525–1532.

[138] Tsuji, Y., Tanaka, T., and Ishida, T., 1992. "Lagrangian numerical simulation of plug flow of cohesionless particles in a horizontal pipe". *Powder Technology,* ***71***, pp. 239–250.

[139] Mindlin, R., and Deresiewicz, H., 1953. "Elastic spheres in contact under varying oblique forces". *J. Appl. Mech. Trans. ASME,* ***20***, pp. 327–344.

[140] Wang, Y., and Mason, M., 1992. "Two-dimensional rigid-body collisions with friction". *Journal of Applied Mechanics-Transactions of the ASME,* ***59***(3), pp. 635–642.

[141] Fu, J., Adams, M., Reynolds, G., and Hounslow, A. S. M., 2004. "Impact deformation and rebound of wet granules". *Powder Technology,* ***140***(3), pp. 248–257.

[142] Mikami, T., Kamiya, H., and Horio, M., 1998. "Numerical simulation of cohesive powder behavior in a fluidized bed". *Chemical Engineering Science,* ***53***(10), pp. 1927–1940.

[143] Rhodes, M., Wang, X., Nguyen, M., P.Stewart, and Liffman, K., 2001. "Use of discrete element method simulation in studying fluidization characteristics: influence of interparticle force". *Chemical Engineering Science,* ***56***(1), pp. 69–76.

[144] Christensen, D., Vervloet, D., Nijenhuis, J., van Wachem, B., van Ommen, J., and Coppens, M., 2008. "Insights in distributed secondary gas injection in a bubbling fluidized bed via discrete particle simulations". *Powder Technology,* ***183***, pp. 454–466.

[145] Allen, M., and Tildesley, D., 1990. *Computer Simulation of Liquids.*

[146] Vervloet, D., 2006. "Lagrangian-Eulerian simulations of secondary injected gas in a bubbling fluidized bed". MSc Thesis, Delft University.

[147] Noreheim, L., 2009. "Discrete Element Modeling of Fluidized Beds with Chemical Looping and Heat Transfer". MS Thesis, Chalmers University of Technology. ISSN: 1652-8557.

[148] Incropera, P., and DeWitt, D., 1996. *Fundamentals of Heat and Mass Transfer, 4th ed.* John Wiley & Sons, New York.

[149] Ranz, W., and Marshall, W., 1952. "Evaporation from drops, part I and II". *Chemical Engineering Progress,* ***48***, pp. 141–146.

[150] Simpson, W., and Ten Wolde, A., 1999. *Wood Handbook, Wood as an Engineering Material, US Department of Agriculture, Madison, Wisconsin, tech. rep. Physical Properties and Moisture Relation of Wood.*

[151] Raupenstrauch, H., 1991. "Ein Beitrag zur Computersimulation reagierender Schüttschichten". PhD Thesis, Graz University of Technology.

[152] Gronli, G., 1996. "A theoretical and experimental study of the thermal degradation of biomass". PhD Thesis, University of Trondheim.

[153] Di Blasi, C. *Simultaneous heat, mass and momentum transfer during biomass drying, Article in: Bridgwater A.V., Boocock D.G.B., Developments in thermochemical biomass conversion, Volume 1, Kluwer Academic Publishers, 1997.*

[154] Alves, S., and Figueiredo, J., 1989. "A model for pyrolysis of wet wood". *Chemical Engineering Science,* ***22***, pp. 2861–2869.

[155] Siau, J., 1984. *Transport Processes in Wood.* Springer Berlin.

[156] Gupta, and Thodos, 1999. *In Perry's Chemical Engineers Handbook.* McGraw-Hill, New York.

[157] Iglesias, H., and Chirife, J., 1982. *Handbook of food isotherms: water sorption parameters for food and food components.* Academic Press: New York.

[158] Burgschweiger, J., Groenewold, H., Hirschmann, C., and Tsotsas, E., 1999. "From hygroscopic single particle to batch fluidized bed drying kinetics". *The Canadian Journal of Chemical Engineering,* ***77***(2), pp. 333–341.

[159] Gmehling, J., and Kolbe, B., 1988. *Thermodynamik.* Georg Thieme Verlag, Stuttgart, New York.

[160] AFNOR, 1976. "NF V03-310 & V03-311, cafe vert et en grains, determination de la teneur eneau". *La Plaine Saint Denis, France.*

[161] Varhegyi, G., Antal, M., Szekeley, T., and Szabo, P., 1989. "Kinetics of thermal decomposition of cellulose, hemicellulose and sugar cane bagasse". *Energy & Fuels,* ***3***, pp. 329–335.

[162] Di Blasi, C., 1995. "Heat, momentum and mass transport through a shrinking biomass particle exposed to thermal radiation". *Chemical engineering sciences,* ***51***(7), pp. 1121–1132.

[163] Shafizadeh, F., and Chin, P., 1977. *Thermal deterioration of wood; In: Wood Technology:Chemical Aspects.* American chemical society.

[164] Thurner, F., and Mann, U., 1981. "Kinetic investigation of wood pyrolysis". *Ind. Eng. Chem. Res,* ***20***, pp. 482–488.

[165] Chan, W., Kelbon, M., and Krieger, B., 1985. "Modelling and experimental verification of physical and chemical processes during pyrolysis of large biomass particles". *Fuel,* ***64***, pp. 1505–1513.

[166] Liden, A., Berruti, F., and Scott, D., 1988. "A kinetic model for the production of liquids from the flash pyrolysis of biomass". *Chemical Engineering Communications,* ***65***, pp. 207–221.

[167] Di Blasi, C., 1993. "Analysis of convection and secondary reaction effects within porous solid fuels undergoing pyrolysis". *Combustion Science and Technology,* ***90***, pp. 315–339.

[168] Lee, C., Chaiken, R., and Singer, J., 1976. "Charring pyrolysis of wood in fires by laser simulation". *16th International Symposium on Combustion, The Combustion Institute, Pittsburgh*, pp. 1459–1470.

[169] Pyle, D., and Zaror, C., 1984. "Heat transfer and kinetics in the low temperature pyrolysis of solids". *Chemical Engineering Science,* ***39***(1), pp. 147–158.

[170] Bridgwater, A., Meier, D., and Radlein, D., 1999. "An overview of fast pyrolysis". *Organic Geochemistry,* ***12***, pp. 1479–1493.

[171] Garcia-Perez, M., Wang, X., Shen, J., Rhodes, M., Tian, F., Lee, W., Wu, H., and Li, C., 2008. "Fast pyrolysis of oil mallee woody biomass: Effect of temperature of the yield and quality of pyrolysis products". *Ind. Eng. Chem. Res.,* ***47***, pp. 1846–1854.

[172] Scott, D., Piskorz, J., Bergougnou, M., Graham, R., and Overend, R., 1988. "The role of temperature in the fast pyrolysis of cellulose and wood". *Ind. Eng. Chem. Res,* ***27***, pp. 8–15.

[173] Horne, P., and Williams, P., 1996. "Influence of temperature on the products from flash pyrolysis of biomass". *Fuel,* ***75***, pp. 1051–1059.

[174] Di Blasi, C., Gonzales Hernandez, E., and Santoro, A., 2000. "Radiative pyrolysis of single moist wood particles". *Ind. Eng. Chem. Res.,* ***39***, pp. 873–882.

[175] Wagenaar, B., Prins, W., and van Swaaij, W., 1994. "Flash pyrolysis kinetics of pine wood". *Fuel Proc Technol,* ***36***, pp. 291–302.

[176] Di Blasi, C., and Branca, C., 2001. "Kinetics of primary product formation from wood pyrolysis". *Ind. Eng. Chem. Res.,* ***40***, pp. 5547–5556.

[177] Font, R., Marcilla, A., Verdu, E., and Devesa, J., 1990. "Kinetics of the pyrolysis of almond shells and almond shells impregnated with $CoCl_2$ in a fluidized bed reactor and in a pyroprobe 100". *Ind. Eng. Chem. Res,* ***29***, pp. 1946–1855.

[178] van der Hoef, M., Ye, M., van Sint Annaland, M., Andrews IV, A., Sundaresan, S., and Kuipers, J., 2006. "Multi-scale modeling of gas-fluidized beds". *Advances in Chemical Engineering,* ***31***, pp. 65–149.

[179] Gunn, D., 1978. "Transfer of heat or mass to particles in fixed and fluidized beds". *International Journal of Heat and Mass Transfer,* ***21***, pp. 467–476.

[180] Miller, R., and Bellan, J., 1997. "A generalized biomass pyrolysis model based on superimposed cellulose, hemicellulose and lignin kinetics". *Combustion, Science and Technology,* ***126***, pp. 97–137.

[181] Gardner, D., Generella, N., Gunnells, D., and Welcott, M., 1991. "Dynamic wettability of wood". *Langmuir, American Chemical Society,* ***7***, pp. 2498–2502.

[182] Bradbury, A., Sakai, Y., and Shafizadeh, F., 1979. "Kinetic model for pyrolysis of cellulose". *J Appl Polym Sci,* ***23***, pp. 3271–80.

[183] Wenzl, H., 1970. *The chemical technology of wood.*

[184] Perry, R., and Green, D., 1984. *Perry's chemical engineers' handbook, 6th edition.* McGraw-Hill.

[185] Flamant, G., Lu, J., and Variot, B., 1993. "Towards a generalized model for vertical walls to gas-solid fluidized beds heat transfer-II. Radiative transfer and temperature effects". *Chemical Engineering Science,* ***48***(13), pp. 2493–2503.

[186] Zhou, H., Flamant, G., and Gauthier, D., 2004. "DEM-LES of coal combustion in a bubbling fluidized bed Part I: gas-particle turbulent flow structure". *Chemical Engineering Science,* ***59***, pp. 4205–4215.

[187] Rabinovich, O., Korban, V., Pal'chenok, G., and Khorol'skaya, O., 2009. "Modeling of fast pyrolysis of a single biomass particle in an inert boiling bed". *Journal of Engineering Physics and Thermophysics,* ***82***(4), pp. 621–631.

[188] Bellais, M., Davidsson, K., Liliedahl, T., Sjöström, K., and Pettersson, J., 2003. "Pyrolysis of large wood particles: A study of shrinkage importance in simulations". *Fuel,* ***82***, pp. 1541–1548.

[189] Hoekstra, E., Hogendoorn, K., Wang, X., Westerhof, R., Kersten, S., van Swaaij, W., and Groeneveld, M., 2009. "Fast pyrolysis of biomass in a fluidized bed reactor: In situ filtering of the vapors". *Ind. Eng. Chem. Res,* ***48***, pp. 4744–4756.

[190] Smolders, K., and Baeyens, J., 1997. "Elutriation of fines from gas fluidized beds: mechanisms of elutriation and effect of freeboard geometry". *Powder Technology,* ***92***, pp. 35–46.

[191] Horio, M., Taki, A., Hsieh, Y., and Muchi, I., 1980. *Fluidization, In: J.R. Grace, J.M. Matsen (Eds.).* Plenum Press.

[192] Smolders, K., and Baeyens, J., 1997. "Continuous monitoring of particle emissions by means of a tribo-electric probe". *Powder Handling Process,* ***9***(2), pp. 123–127.

[193] King, R., 2001. *Modeling and simulation of mineral processing systems.* Butterworth Heinemann.

[194] Griffith, A., 1921. "The phenomena of rupture and flow in solids". *Phylosophical Transactions of the Royal Society of London A,* ***221***, pp. 163–198.

[195] Kun, F., and Herrmann, H., 1999. "Transition from damage to fragmentation in collision of solids". *Phys. Rev. E,* ***59***, pp. 2623–2632.

[196] Åström, J., Kellomäki, M., and Timonen, J., 1997. "Dynamic fragmentation of a two-dimensional brittle material with quenched disorder". *Phys. Rev. E,* ***55***, pp. 4757–4761.

[197] Åström, J., Holian, B., and Timonen, J., 2000. "Universality in fragmentation". *Phys. Rev. Lett.,* ***84***(14), pp. 3061–3064.

[198] Mott, N., 1945. "Fragmentation of shell cases". *Proceedings of the Royal Society of London, Series A, Mathematical and Physical Sciences,* ***189***.

[199] Tavares, L., and de Carvalho, R., 2009. "Modelling breakage rates of coarse particles in ball mills". *Mineral Engineering,* ***22***, pp. 650–659.

[200] Vogel, L., and Peukert, W., 2004. "Determination of material properties relevant to grinding by practicable labscale milling tests". *Int. J. Miner. Process,* ***745***, pp. S329–S338.

[201] Morrison, R., Shi, F., and Whyte, R., 2007. "Modelling of incremental rock breakage by impact; for use in DEM models". *Mineral Engineering,* ***20***, pp. 303–309.

[202] Vogel, L., and Peukert, W., 2005. "From single impact behaviour to modelling of impact mills". *Chemical Engineering Science,* ***60***, pp. 5164–5176.

[203] Bearman, R., Briggs, C., and Kojovic, T., 1997. "The application of rock mechanics parameters of the prediction of comminution behaviour". *Mineral Engineering,* ***10***(3), pp. 225–264.

[204] Napier-Munn, T., Morrel, S., Morrison, R., and Kojovic, T., 1996. *Mineral Comminution Circuits - Their Operation and Optimisation.* JKMRC, Brisbane, Australia.

[205] Rumpf, H., and Bull, F., 1975. *Particle Technology (Powder Technology Series).*

[206] Harris, C., 1966. "On the role of energy in comminution: A review of physical and mathematical principles". *Trans. IMM (London),* ***75***, pp. C37–C56.

[207] Bergstrom, B., 1966. "Empirical modification of the Gaudin-Meloy equation". *AIME Trans,* ***235***, p. 45.

[208] Kolmogoroff, A.", 1941.". *Doklady Akad. Nauk S.S.S.R,* ***31***(99).

[209] Halmos, P., 1944. "Random alms". *Ann. Math. Stat,* ***15***, p. 182.

[210] Epstein, B., 1947. "The mathematical description of certain breakage mechanisms leading to the logarithmico-normal distribution". *J.Franklin Inst,* ***244***, pp. 471–477.

[211] Gilvarry, J., 1961. "Fracture of brittle solids. I. Distribution function for fragment size in single fracture (theoretical)". *Journal of Applied Physics,* ***32***(3).

[212] Shi, F., and Kojovic, T., 2007. "Validation of a model for impact breakage incorporating particle size effect". *International Journal of Mineral Processing,* ***82***, pp. 156–163.

[213] Whiten, W., and Narayanan, S., 1988. "Determination of comminution characteristics from single particle breakage tests and its application to ball mill scale-up". *Transactions of the Institution of Mineral Metallurgy,* ***97***, pp. 115–124.

[214] Morrison, R., and Grady, P., 2004. "Using DEM to model ore breakage within a pilot scale SAG mill". *Minerals Engineering,* ***17***, pp. 1117–1124.

[215] Jaeger, J., 1967. "Failure of rocks under tensile conditions". *Int. J. Rock Mech. Miner. Sci,* ***4***, pp. 219–237.

[216] Prasher, C., 1987. *Crushing and grinding process handbook*. John Wiley & Sons Inc.

[217] Chirone, R., Cammarota, A., D'Amore, M., and Massimilla, L., 1982. "Elutriation of attrited carbon fines in a fluidized combustion of coal". *Proceedings of the Nineteenth International Symposium of Combustion*, p. 1213.

[218] Baumgardt, S., Buss, B., May, P., and Schubert, H., 1975. "On the comparision of results in single grain crushing under different kinds of load". *Proc. 11th Int. Miner. Process. Congr., Calgiari*, pp. 3–32.

[219] Bergstrom, C., 1963. "Energy and size distribution aspects of single particle crushing In: Fairhurst C., Rock Mechanics, Proceedings of the 5th Symposium on Rock Mechanics, Pergamon Press, New York, pp.155-172, May 1962".

[220] Weiss, N., 1985. *SME Mineral Processing Handbook*. SME-AIME, New York.

[221] Wu, S., Chau, K., and Yu, T., 2004. "Crushing and fragmentation of brittle spheres under double impact test". *Powder Technology,* ***143***, pp. 41–55.

[222] Schäfer, F., 2006. "An engineering fragmentation model for the impact of spherical projectiles on thin metallic plates". *International Journal of Impact Engineering,* ***33***, pp. 745–762.

[223] Tsuji, T., Yabumoto, K., and Tanaka, T., 2008. "Spontaneous structures in three-dimensional bubbling gas-fluidized bed by parallel DEM-CFD coupling simulation". *Powder Technology,* ***184***, pp. 132–140.

[224] Cleary, P., 2009. "Ball motion, axial segregation and power consumption in a full scale two chamber cement wall". *Minerals Engineering,* ***22***, pp. 809–820.

[225] Cui, H., and Grace, J., 2008. "Spouting of biomass particles: A review". *Bioresource Technology,* ***99***, pp. 4008–4020.

[226] Patankar, S., 1980. *Numerical heat transfer and fluid flow.* McGraw-Hill Book Company.